OUT-OF-BAND RADIATION AND CFO IMMUNITY OF POTENTIAL 5G MULTICARRIER MODULATION SCHEMES

A THESIS SUBMITTED TO
THE GRADUATE SCHOOL OF NATURAL AND APPLIED SCIENCES
OF
MIDDLE EAST TECHNICAL UNIVERSITY

BY

ALİ BULUT ÜÇÜNCÜ

IN PARTIAL FULFILLMENT OF THE REQUIREMENTS
FOR
THE DEGREE OF MASTER OF SCIENCE
IN
ELECTRICAL AND ELECTRONICS ENGINEERING

AUGUST 2015

Approval of the thesis:

OUT-OF-BAND RADIATION AND CFO IMMUNITY OF POTENTIAL 5G MULTICARRIER MODULATION SCHEMES

submitted by **ALİ BULUT ÜÇÜNCÜ** in partial fulfillment of the requirements for the degree of **Master of Science in Electrical and Electronics Engineering Department, Middle East Technical University** by,

Prof. Dr. Gülbin Dural Ünver
Dean, Graduate School of **Natural and Applied Sciences** _____

Prof. Dr. Gönül Turhan Sayan
Head of Department, **Electrical and Electronics Engineering** _____

Prof. Dr. Ali Özgür Yılmaz
Supervisor, **Electrical and Electronics Engineering Dept., METU** _____

Examining Committee Members:

Prof. Dr. Yalçın Tanık
Electrical and Electronics Engineering Dept., METU _____

Prof. Dr. Ali Özgür Yılmaz
Electrical and Electronics Engineering Dept., METU _____

Prof. Dr. Tolga Mete Duman
Electrical and Electronics Engineering Dept., Bilkent University _____

Assoc. Prof. Dr. Çağatay Candan
Electrical and Electronics Engineering Dept., METU _____

Asst. Prof. Dr. Sevinç Figen Öktem
Electrical and Electronics Engineering Dept., METU _____

Date: 19.08.2015

I hereby declare that all information in this document has been obtained and presented in accordance with academic rules and ethical conduct. I also declare that, as required by these rules and conduct, I have fully cited and referenced all material and results that are not original to this work.

Name, Last Name: ALİ BULUT ÜÇÜNCÜ

Signature :

ABSTRACT

OUT-OF-BAND RADIATION AND CFO IMMUNITY OF POTENTIAL 5G MULTICARRIER MODULATION SCHEMES

Üçüncü, Ali Bulut
M.S., Department of Electrical and Electronics Engineering
Supervisor : Prof. Dr. Ali Özgür Yılmaz

August 2015, 98 pages

In this study, generalized frequency division multiplexing (GFDM) and windowed cyclic prefix circular offset quadrature amplitude modulation (WCP-COQAM), which are candidate physical layer modulation schemes for the 5G systems, are compared to orthogonal frequency division multiplexing (OFDM) in terms of out-of-band (OOB) radiation levels and carrier frequency offset (CFO) immunity. GFDM and WCP-COQAM are shown to be superior to OFDM with respect to OOB emissions in some studies in literature. However, we consider that these comparisons are made under unfair conditions since OOB reduction techniques are not also applied to OFDM and the spectral efficiencies of the three modulations are not equal. Establishing fair comparison grounds accordingly, the simulation results yielded no significant OOB emission performance difference between the three modulation types. Further simulations considering some parameters related to the transmitted signals such as error-vector magnitude or average power under the effects of amplifier nonlinearity or digital-to-analog converter also revealed no significant difference between the three modulation types under LTE spectral mask requirements.

The three modulation types are also compared in terms of their carrier frequency offset (CFO) immunities. To achieve better CFO immunity, advanced pulse shaping methods defined for offset quadrature amplitude modulation OFDM (OQAM-OFDM) are also applied to WCP-COQAM. This is possible since the two modulations are also proved to be equivalent in terms of orthogonality, which is one of the main analytic contributions of this thesis. However, the error rate performance simulations under CFO for various channel conditions did not improve CFO immunity for WCP-COQAM or GFDM compared to OFDM.

Keywords: GFDM, WCP-COQAM, OOB emissions, CFO robustness, FBMC, Spectral mask

ÖZ

OLASI 5G ÇOKLU-TAŞIYICI KİPLEMELERİNİN BANT DIŞI EMİSYONLARI VE CFO DAYANIKLILIKLARI

Üçüncü, Ali Bulut
Yüksek Lisans, Elektrik ve Elektronik Mühendisliği Bölümü
Tez Yöneticisi : Prof. Dr. Ali Özgür Yılmaz

Ağustos 2015, 98 sayfa

Bu çalışmada genelleştirilmiş frekans bölümlemeli çoğullama (GFDM) ve pencerelemeli döngüsel ön ekli dairesel offset dördül genlik modülasyonu (WCP-COQAM) olarak adlandırılan 5G haberleşme sistemleri için aday fiziksel katman modülasyon teknikleri, dik frekans bölümlemeli çoğullama (OFDM) tekniği ile bant dışı (OOB) emisyonları ve taşıyıcı frekans hatası (CFO) dayanıklılığı açılarından karşılaştırılmıştır. GFDM ve WCP-COQAM'nin literatürdeki bazı çalışmalarda OFDM'e göre OOB emisyonları açısından daha iyi başarım gösterdiği iddia edilmektedir. Buna karşın, literatürdeki OOB emisyon karşılaştırmalarının eşit spektral verimlilik altında yapılmaması ve OOB emisyon azaltıcı tekniklerin OFDM için de uygulanmaması sebeplerinden ötürü bu karşılaştırmaların adil yapılmadığı değerlendirilmektedir. Çalışmamızda bu açılardan daha adil koşullar altında yapılan benzetimlerde 3 modülasyon tipi için OOB emisyonları açısından önemli farklılık gözlenmemiştir. Daha ileri seviyedeki benzetimlerde LTE standartlarında belirtilen spektral maske gerekliliklerine uygun koşullarda anfi doğrusalsızlığı ve dijitalden analoğa dönüştürücü etkileri al-

tında 3 ayrı modülasyon tipi için iletilen sinyalin hata vektör genliği (error vector magnitude) ve ortalama iletim gücü parametreleri açısından da benzer sonuçlar görülmüştür.

Söz konusu modülasyon tipleri taşıyıcı frekans hatasına karşı gürbüzlükleri açısından da karşılaştırılmıştır. Daha iyi CFO gürbüzlüğü sağlayabilmek amacıyla literatürde offset dördül genlik modülasyonu OFDM (OQAM-OFDM) için uygulanan gelişmiş darbe biçimi tasarım yöntemleri WCP-COQAM için de uygulanmıştır. Bu durum çalışmamızın analitik anlamda önemli katkılarından olan OQAM-OFDM için diklik (orthogonality) şartlarını sağlayan darbe şekillerinin WCP-COQAM için de sağladığının matematiksel olarak kanıtlanması sayesinde mümkün olmuştur. Buna karşın, çeşitli kanal koşullarında hata oranı başarımının gözlendiği kapsamlı benzetimlerde CFO gürbüzlüğü açısından da GFDM veya WCP-COQAM, OFDM'e göre daha yüksek başarım göstermemiştir.

Anahtar Kelimeler: GFDM, WCP-COQAM, OOB emisyonları, CFO gürbüzlüğü, FBMC, Spektral maske

To my family and my dearest friends

ACKNOWLEDGMENTS

To begin with, I would like to express my deepest gratitude to my supervisor, Prof. Ali Özgür Yılmaz for his invaluable guidance, patience and support throughout my M.S. studies. His mentorship provided me to have an insight on a wide range of topics in telecommunications area. Working with him in research projects was also a privilege. His understanding during the hard times I underwent during my M.S. period was also important for me to not to loose my self-esteem.

I would also like to thank Dr. Gökhan Muzaffer Güvensen for his endless support, motivation and friendship during the M.S. period. I had very enjoyable times with him from the first day that I met him in D-226. Apart from his enjoyable and kind friendship, his knowledge and experience provided me to enhance my vision related to subjects I dealt with during this thesis.

Another important contribution to my thesis work has come from Erman Köken. The methodology he used to analyze the peak-to-average power values of different modulation types was also used in this thesis. Moreover, I have learnt some important details from the MATLAB codes he provided.

I am also thankful to ASELSAN Inc. for their financial support during the research project they provided. The project has provided me a chance to study on a practical subject and enhanced my knowledge and experience to a significant level. In fact, the subject of this thesis emerged from the studies that me and my team-mates dealt with during the project. It was a pleasure for me to work with Tuğcan Aktaş, Alptekin Yılmaz and Yunus Can Gültekin, in this project thanks to their friendship and the fruitful discussions that we had during our studies. I would also like to express my best feelings to Alper Yazar, Ömer Özdemir, Seçil Özdemir, Ömer Melih Gül, Samet Gelincik, Pınar Şen, Mürsel Karadaş and Selim Özgen for the enjoyable times that we had. I am also very thankful to my friends whose names are not mentioned here for their support and the pleasant times that we had. Very special thanks go to Arzu

İpek Yılmaz for the invaluable trust that she provided me to make me secure during the time that we had up to now and for the future.

I also want to acknowledge the prestigious financial support that Turkcell and the scientific and technological research council of Turkey (TÜBİTAK) provided me during my M.S. period. I will try to contribute to my country as most as possible in order to deserve their support.

Lastly by not the least, I would like to express my indebtedness to my family, Neslihan and Murat Üçüncü. Without their support, love and trust many of the achievements that I have done would not be possible.

TABLE OF CONTENTS

LIST OF FIGURES

FIGURES

LIST OF ABBREVIATIONS

ADSL	Asymmetric Digital Subscriber Lines
AM	Amplitude Modulation
AST	Adaptive Symbol Transition
AWGN	Additive White Gaussian Noise
BW	Bandwidth
CC	Cancellation Carrier
CFO	Carrier Frequency Offset
CMT	Cosine Modulated Multitone
COST-207	European Cooperation in Science and Technology-207
CP	Cyclic Prefix
CR	Cognitive Radio
DAB	Digital Audio Broadcasting
DAC	Digital-to-Analog Converter
DFT	Discrete Fourier Transform
DSB	Double-Sideband
DTFT	Discrete Time Fourier Transform
DZT	Discrete Zak Transform
EVM	Error-vector magnitude
FBMC	Filter-Bank Multicarrier
FCC	Federal Communications Commission
FDM	Frequency Division Multiplexing
FFT	Fast Fourier Transform
FIR	Finite Impulse Response
FM	Frequency Modulation
GFDM	Generalized Frequency Division Multiplexing
GWCP-COQAM	Guard Symbol Inserted WCP-COQAM
GW-GFDM	Guard Symbol Inserted and Windowed GFDM
GW-OFDM	Guard Symbol Inserted and Windowed OFDM
HDSL	High-Bit-Rate Digital Subscriber Lines
HDTV	High-Definition Television
HGUP	Heisenberg-Gabor Uncertainity Principle
ICI	Inter-Carrier Interference

IEEE	Institute of Electrical and Electronics Engineers
IF	Intermediate Frequency
IFFT	Inverse Fast-Fourier Transform
IoT	Internet-of-Things
IOTA	Isotropic Orthogonal Transform Algorithm
ISI	Inter-Symbol Interference
ITU	International Telecommunications Union
LTE	Long-Term Evolution
MF	Matched Filter
MF-DSIC	Double Sided Inter-carrier Interference Cancellation
MMSE	Minimum Mean Squared Error
OFDM	Orthogonal Frequency Division Multiplexing
OOB	Out-of-Band
OQAM	Offset Quadrature Amplitude Modulation
OQAM-OFDM	Offset Quadrature Amplitude Modulation-Orthogonal Frequency Division Multiplexing
PA	Power Amplifier
PAPR	Peak-to-Average Power Ratio
PM	Phase Modulation
PSD	Power Spectral Density
QAM	Quadrature Amplitude Modulation
QPSK	Quadrature Phase Shift Keying
RC	Raised-Cosine Spectrum
RF	Radio-Frequency
RRC	Root-Raised-Cosine Spectrum
SER	Symbol Error Rate
SIR	Signal-to-Interference Ratio
SMT	Staggered Multitone
SNR	Signal-to-Noise Ratio
TFL	Time-Frequency Localization
VDSL	Very-High-Speed Digital Subscriber Lines
VR	Virtual Reality
VSB	Vestigial-Sideband
WCP-COQAM	Windowed Cyclic Prefix Circular Offset Quadrature Amplitude Modulation
W-GFDM	Windowed GFDM
WIMAX	Worldwide Interoperability for Microwave Access
W-OFDM	Windowed OFDM
ZF	Zero-Forcing

CHAPTER 1

INTRODUCTION

Inter-symbol interference (ISI) caused by the transmission channel is a typical problem that has been widely studied in the communications literature. It is mainly caused by the multipath nature of the transmission channel, that is, the transmitted signal reaches the receiver through multiple paths. If the time delay between the multiple paths is not significantly smaller than the symbol duration, cancelling the effects of ISI becomes necessary. To combat ISI, there are mainly two approaches. One of them is to use equalizers that mitigate the effects of the ISI channel. However, if the amount of multipath distortion is significant, equalization can be very complex. In that case, multicarrier modulation techniques appear as an alternative solution to deal with ISI. In a multicarrier communication scenario, the binary data bits to be transmitted are divided into substreams and each substream is sent over subchannels, each of which constitutes some portion of the total transmission bandwidth. An illustration of the division of the transmission channel into subchannels is in Figure 1.1 [1].

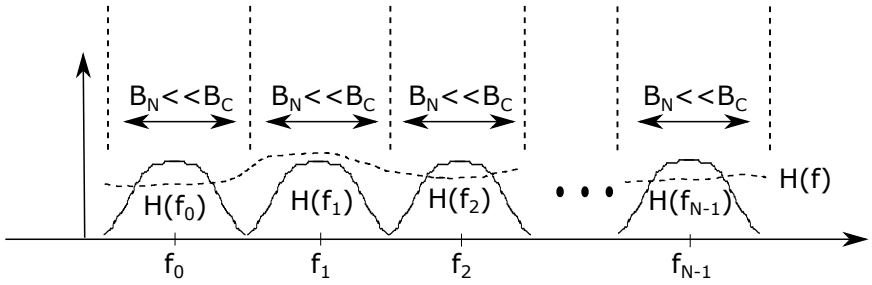

Figure 1.1: A typical multicarrier transmission from the frequency domain point of view

As can be observed from Figure 1.1, over the band of each subchannel represented as B_N, the frequency response of the channel $H(f)$ is approximately flat. This means that there will be no significant ISI over the subchannels, that is, the subchannels experience flat fading. For this to hold, the bandwidth of the subbands B_N should be significantly smaller than the coherence bandwidth of the transmission channel [1]. Without dividing the main binary stream into substreams, and transmitting them over separate subbands, if the transmission was carried out by a single carrier with a bandwidth larger than the coherence bandwidth of the channel, the transmission channel would be observed as a frequency selective channel causing significant levels of ISI. This would require complex equalization. Instead, the ISI effects can be avoided substantially by dividing the available bandwidth into subchannels and transmitting the data symbols using these separate subbands over an effectively flat transmission channel.

Among the multicarrier communication schemes, orthogonal frequency division multiplexing (OFDM) is one of the most popular. Unlike the scheme shown in Figure 1.1, in which the subchannels are nonoverlapping, the subchannels in OFDM are overlapping. Two multicarrier modulation schemes with overlapping and nonoverlapping subbands are depicted in Figure 1.2.

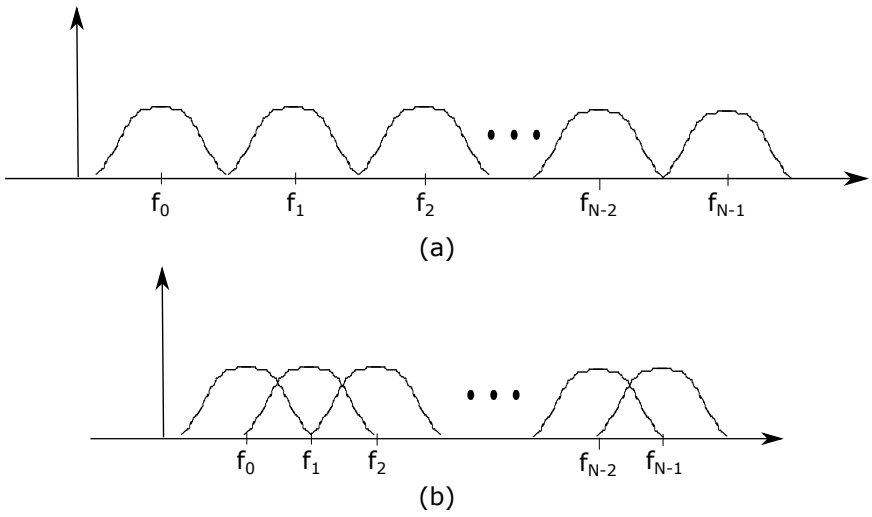

Figure 1.2: Multicarrier schemes with nonoverlapping (a) or overlapping (b) subchannels

For the schemes with nonoverlapping subchannels, it is straightforward to state that the subbands create no interference to each other if they are separated with conventional filtering at the receiver side. The downside of using non-overlapping subchannels is the reduced spectral efficiency. On the other hand, when the subchannels are overlapping, it appears that different subchannels can interfere with each other. However, it can easily be proved that if the subchannels are separated with a distance of multiples of $1/T_s$, where T_s is the symbol interval, there will be no interference between the subchannels in OFDM. Therefore, an increase in the spectral efficiency can be attained while avoiding interference.

In addition to its advantages against multipath distortion, there are also other factors that promote the use of OFDM in many communication systems. These are summarized below [2].

- The transmitter and receiver filters can be implemented easily by using basic fast Fourier transform (FFT) and inverse FFT blocks.
- Multiantenna structures can be implemented easily by using OFDM both at the transmitter and receiver side.
- It is possible to achieve capacity gains over each subcarrier by observing the signal-to-noise ratio levels at a particular subcarrier and applying rate adaptation accordingly.
- OFDM is robust to narrowband interference due to the fact that only a fraction of the total subcarriers are affected from such interference.
- Single frequency networks, which are suitable for broadcasting applications, can be used with OFDM.

On the other hand, OFDM has also some disadvantages, which are

- High sensitivity to frequency offset and phase noise [3], [4], [5].
- Large peak-to-average-power ratio (PAPR), which causes the average transmitted power to reduce. This decreases the information capacity of the transmission channel [6].

- Large out-of-band radiation due to the poor decaying property of the rectangular pulse shape used in OFDM [5], [7].

In spite of its aforementioned fallbacks, the advantages of OFDM have enabled its use in a wide range of applications even in the early stages of digital communication. For instance, KINEPLEX [8], ANDEFT [9], and KATHRYN [10] are examples of high-frequency military systems that used OFDM technique in 1960s. In 1980s, OFDM technique was used for high-speed modems, high-density recording and digital mobile communications. Moreover, mobile radio FM channels, high-bit-rate digital subscriber lines (HDSL), asymmetric digital subscriber lines (ADSL), very-high-speed digital subscriber lines (VDSL), digital audio broadcasting (DAB) and high-definition television (HDTV) terrestrial broadcasting were some of the application areas of OFDM in 1990s [2].

The most recent examples of applications of OFDM are the wireless local area network standards including IEEE 802.11a, 802.11g, and 802.11j [11]. OFDM has also been included in the 4G standards such as Mobile WIMAX [12] and LTE [13]. These 4G standards have data rates reaching up to several hundreds of Mbits/s in order to cope with the high data rate demand created mainly with the advent of the smartphones equipped with large storage and processing power and high definition screen and cameras.

The scenarios that are considered for the future 5G systems have already exceeded the capabilities of the current 4G systems [14]. These scenarios are related to Tactile internet [15], which is defined by ITU in August 2014 as an internet network that is able to serve applications that have virtual, visual and auditory human-to-machine interaction with low latency requirements down to 1 millisecond. Such an interaction can be over numerous sensors and all of the information from these sensors should be received, processed and a response should be given without too much time-lag to satisfy a high quality interaction between human and technical systems. Moving our heads while wearing Virtual Reality (VR) goggles to receive immediate visual response can be an example for such applications.

Furthermore, machine-to-machine communications is also a recent discussion that draws attention. Industrial robots and electronic stability control systems used in

the vehicles can be given as examples. Furthermore, such systems can also interact with a centralized server in the communication system. This creates giant sized and heterogeneous networks that have elements ranging from sensors to server centers with high processing or storage capacity. Such an infrastructure is also referred under the name of Internet of Things (IoT) [16].

Furthermore, in order to increase data rates in 5G systems through an increase in spectral efficiency, cognitive radio (CR) based approaches can also be used. Cognitive radio is the general name given to the techniques that utilize the unused portions of the frequency spectrum opportunistically. In order for the CR based techniques to be more effective, the users should not radiate much power out of the transmission band allocated to them. Only in such a case, the neighboring bands of a specific user are not polluted much and other users can use these neighboring bands opportunistically. Therefore, low out-of-band (OOB) radiation levels is also a requirement in 5G systems.

Being the main physical layer modulation format in the latest 4G communication standard, OFDM is an important candidate for the physical layer solution in the 5G systems. However, since the rectangular pulse that is used in OFDM has large side lobes, which in turn increases its OOB radiation, strict frequency synchronization requirements, alternative modulation formats such as filter-bank multicarrier (FBMC), time-frequency packed signalling, and single-carrier modulations are being considered as candidates for the modulation formats that will be used in 5G. Among these modulation schemes, one of the most popular is the Generalized Frequency Division Multiplexing (GFDM) offered by Fettweis et al. [7]

One main advantage of GFDM compared to OFDM is claimed to be its reduced OOB radiation [7]. The reason for such an advantage to appear is having a pulse shape that has better decaying property in frequency domain compared to that of the rectangular pulse of OFDM. In GFDM, the pulse shaping filter that will be used at the transmitter side can flexibly be chosen. Furthermore, in [7], another superiority of GFDM over OFDM is stated to be about the lower spectral efficiency loss caused by the cyclic prefix (CP). In GFDM, there is still a CP as in OFDM. However, a single CP in a GFDM frame is enough to be appended to a number of GFDM symbols, whereas a

CP should be used for each OFDM symbol. In that respect, GFDM seems to have spectral efficiency advantage in terms of the overhead caused by the CP compared to OFDM. The reason for that advantage of GFDM will be more clear when the frame and symbol structures of OFDM and GFDM are examined in detail in Chapter 3.

In this thesis, the claimed advantages of GFDM over OFDM are investigated. Firstly, GFDM and OFDM are compared in terms of OOB radiations under fair conditions. Unlike [7], in which OOB reduction techniques such as guard symbol insertion and windowing are applied only to GFDM, they will be applied both to OFDM and GFDM. Furthermore, OOB emissions are also compared when OFDM and GFDM have equal spectral efficiency. Equal spectral efficiency conditions are established by increasing the number of subcarriers in OFDM, keeping the same transmission bandwidth. In such a case, the spectral efficiency loss caused by the CP will be equal for OFDM and GFDM. The reason for this fact can be understood more clearly, when the frame structures of OFDM and GFDM detailed in Chapter 3 are examined. However, OFDM has increased vulnerability to carrier frequency offset (CFO) when more subcarriers are packed into the same transmission bandwidth. Hence, error rate performances of OFDM and GFDM will also be compared under CFO, when their spectral efficiencies are the same.

A variant of GFDM called windowed cyclic prefix circular offset QAM (WCP-COQAM) is proposed by Lin and Siohan [17]. The main difference between GFDM and WCP-COQAM is that OQAM type of modulation is utilized in WCP-COQAM, compared to the QAM type modulation in GFDM. The details about WCP-COQAM are covered in Chapter 3. WCP-COQAM is also included in the above-mentioned comparisons between OFDM and GFDM. Moreover, in Chapter 4, the equivalence of the orthogonality conditions of OQAM-OFDM and WCP-COQAM is proved and optimal pulse shaping methods defined for OQAM-OFDM in literature is also applied to WCP-COQAM. The proof of the equivalence of OQAM-OFDM and WCP-COQAM is the main analytic contribution of this thesis.

The organization of this thesis is made as follows. In Chapter 2, the details about OFDM and FBMC modulation types will be presented. In Chapter 3, GFDM and WCP-COQAM modulations will be discussed in detail, and their CFO vulnerabilities

will be compared when OFDM, GFDM and WCP-COQAM have equal or unequal spectral efficiencies. Chapter 4 describes advanced pulse shaping methods for FBMC. These pulse shaping methods will be applied to WCP-COQAM and the performances of the designed pulses are investigated under CFO in comparison to OFDM. Finally, the OOB emissions of OFDM, GFDM and WCP-COQAM are compared in Chapter 4. Some of the OOB emission comparisons in Chapter 4 also take the spectral mask requirements in LTE, amplifier non-linearity and digital to analog converter (DAC) effects into account.

CHAPTER 2

OFDM AND FBMC

2.1 Orthogonal Frequency Division Multiplexing (OFDM)

OFDM is a multicarrier modulation technique that consists of orthogonal subcarriers. The frame structure of OFDM with subsequent OFDM symbols is given in Figure 2.1.

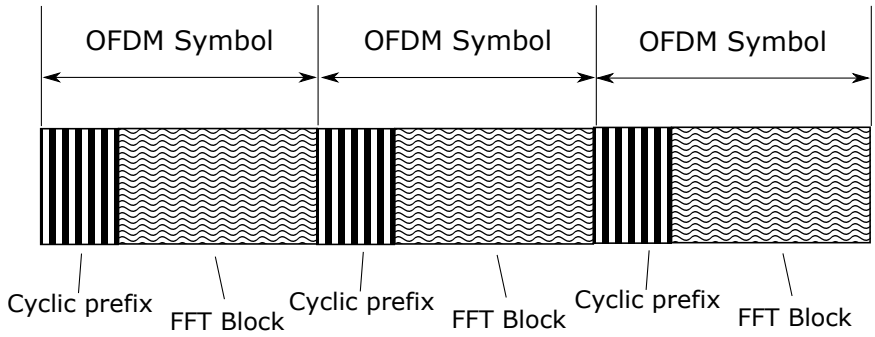

Figure 2.1: OFDM frame consisting of 3 OFDM symbols

As can be observed in Figure 2.1, OFDM symbols are separated through an interval called "cyclic prefix". Addition of cyclic prefix is necessary to ensure that there is no interference between the subsequent OFDM symbols. The reason for such an interference between the OFDM symbols originates from the time dispersion of the transmission channel, or any timing error at the receiver. The timing dispersion caused by the transmission channel is presented in Figure 2.2.

Assuming that there is no timing error at the receiver, the cyclic-prefix should be larger than the delay spread of the transmission channel [1]. In that case, the leakage

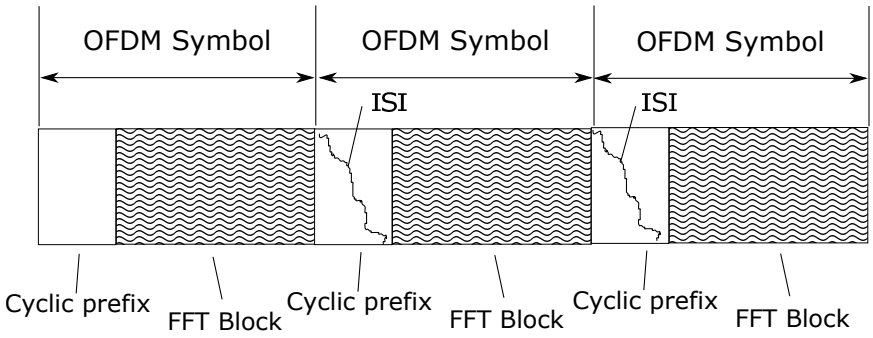

Figure 2.2: Dispersion caused by the transmission channel on the OFDM symbols

of the OFDM symbols to the next OFDM symbol will fall into the cyclic prefix interval between the two symbols. Since the cyclic prefixes are discarded at the OFDM receiver, there will be no interference between the OFDM symbols.

The OFDM transmitter and receiver structure are demonstrated in Figure 2.3. [1].

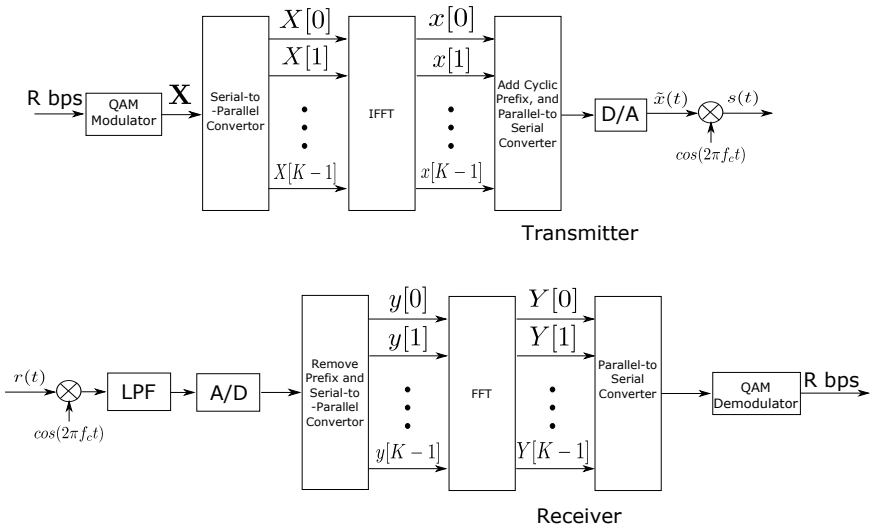

Figure 2.3: OFDM transmitter and receiver

As can be seen from Figure 2.3, the binary sequence to be transmitted is first fed into a modulator, which is of quadrature-amplitude modulation (QAM) type without loss of generality, that yields the symbol vector $\mathbf{X}$ of length K. The serial-to-parallel converter outputs the elements of the vector $\mathbf{X}$ whose inverse fast-Fourier transform (IFFT) is taken by the IFFT block to yield the following discrete signal $x[n]$:

$$x[n] = \sum_{k=0}^{K-1} X[k] e^{j2\pi nk/K}, 0 \leqslant n \leqslant K-1. \tag{2.1}$$

After the addition of cyclic prefix, interpolation by D/A converter and upconversion to carrier frequency f_0, $s(t)$ is transmitted to the channel. After $s(t)$ passes through the channel, the received signal $r(t)$ is downconverted and low-pass filtered. The A/D converter yields the discrete samples $y[n]$. Cyclic prefix part is removed from $y[n]$ and series to parallel converter outputs the samples whose FFT is taken by the FFT block. Finally, the FFT outputs are serialized and demodulated to obtain the estimates of the transmitted binary data bits.

An important point is that the cyclic prefix length should be at least equal to the delay spread of the transmission channel [1], and should have a special structure in order that the equalization of the channel can be made very easily.

Consider a discrete sequence, $x[n] = x[0], x[1], \cdots, x[K-1]$. Furthermore, assume that the transmission channel impulse response is characterized by, $h[n] = h[0], h[1], \cdots, h[L-1]$. Here $L = T_d/T_s$, where T_s is the sampling rate and T_d is the channel delay spread.

Define the cyclic prefix for x[n] as $x[K-L], \cdots, x[K-1]$, that is, it consists of the last L samples of the sequence $x[n]$. Since cyclic-prefix is appended at the beginning of $x[n]$, the transmitted signal $\tilde{x}[n]$ will be obtained as $\tilde{x}[n] = x[K-L], x[K-L-1], \cdots, x[K-1], x[0], x[1], \cdots, x[K-1]$. Assume also that $\tilde{x}[n]$ is fed into the channel, $h[n]$. In this case, the discrete output signal $y[n]$ will be obtained as

$$\begin{aligned} y[n] &= h[n] * \tilde{x}[n] \\ &= \sum_{l=0}^{L} h[l]\tilde{x}[n-l] \\ &= \sum_{k=0}^{L} h[l]x[n-l]_K \\ &= h[n] \circledast x[n] \end{aligned} \tag{2.2}$$

where the last equality follows due to the fact that $\tilde{x}[n-l] = x[n-l]_K$, for $0 \leqslant n \leqslant K-1$. Therefore, appending $x[n]$ with the specified cyclic prefix

structure, the linear convolution of $x[n]$ with $h[n]$ becomes equivalent to the circular convolution between $x[n]$ and $h[n]$. Hence, if the DFT of $y[n]$ is taken,

$$DFT\left\{y[n]\right\} = Y[k] = X[k]H[k], \;\; 0 \leqslant k \leqslant K-1 \tag{2.3}$$

where X[k] and H[k] are the K-point DFTs of x[n] and h[n], respectively. Therefore, according to (2.3), the equalization of the channel can be carried out with a very simple operation as DFT. Since FFT operation is already performed at the receiver of OFDM, the equalization can simply be accomplished through dividing $Y[k]$, which is obtained after the FFT block in Figure 2.3, by $H[k]$.

2.2 Filter Bank Multicarrier (FBMC)

FBMC is the general name for the multicarrier modulation methods that uses arbitrary pulse shaping filters to form the subcarriers over which the frequency selectivity of the channel is small enough to require a complex equalization block at the receiver. The transmitter and the receiver structure for FBMC is presented in Figure 2.4. [5].

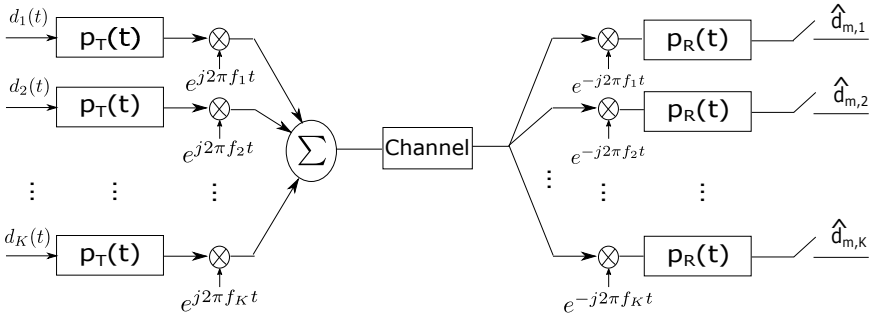

Figure 2.4: FBMC transmitter and receiver

As can be observed in Figure 2.4, the symbols to be transmitted $d_k(t)$, which are impulse functions that are weighted with the data symbols to be transmitted, are fed to the filter bank in the transmitter. These filter banks generate the pulse shape over which the data will be transmitted. Furthermore, multiplication by the complex exponentials carries the baseband data to the subcarrier locations in the frequency spectrum. Then, the transmitted signal is passed through the transmitted channel to reach

the receiver block. The receiver consists of filters that are matched to the pulse shape and the subcarrier of the data symbol to be estimated. At the filter outputs, the samples are taken at every symbol duration to yield the estimates of the transmitted data symbols.

Figure 2.4 gives a general picture of the transmitter and receiver structure of FBMC type modulation schemes. More specifically, FBMC techniques can be divided into two distinct types. In the first FBMC type, QAM symbols having complex values are transmitted. These complex valued symbols will be denoted as $d_{m,k}$. The subscripts m and k mean that the symbol is to be transmitted at the k^{th} subcarrier and m^{th} symbol time interval. The relation between $d_{m,k}$ and $d_k(t)$ in Figure 2.4 can be written as follows.

$$d_k(t) = \sum_m d_{k,m}\delta(t - mT). \tag{2.4}$$

In fact, the block diagram given in Figure 2.4 can also represent an OFDM transmitter and receiver. In that case, the impulse responses of the receive and the transmit filters $p_t(t)$ and $p_r(t)$ are rectangular pulses. Moreover, considering Figure 2.4, the signal model for OFDM or FBMC can be written as,

$$x(t) = \sum_k \sum_m d_{k,m} p(t - mT) e^{j2\pi t f_k} \tag{2.5}$$

where $p(t)$ is the pulse shaping filter, T is the symbol timing, $d_{k,m}$ is the data to be transmitted at the k^{th} subcarrier and the m^{th} symbol in time. Moreover, f_k is the location of the subcarrier in frequency domain. Furthermore, $p(t)$ can be any pulse shape. For example if it is a root raised cosine spectrum filter (RRC) with roll of factor α, in order that the subcarrier bands do not overlap, the frequency spacing between the subcarriers should be at least $F = (1 + \alpha)/T$, which is demonstrated in Figure 2.5. [5].

With a frequency spacing of $F = (1+\alpha)/T$, where T is the symbol spacing, the time-frequency phase-space lattice representation of an FBMC system can be depicted as in Figure 2.6. [5].

From the lattice representation it is possible to see the spacing between the subcarriers and the symbol time interval from the lattice points. An important parameter related

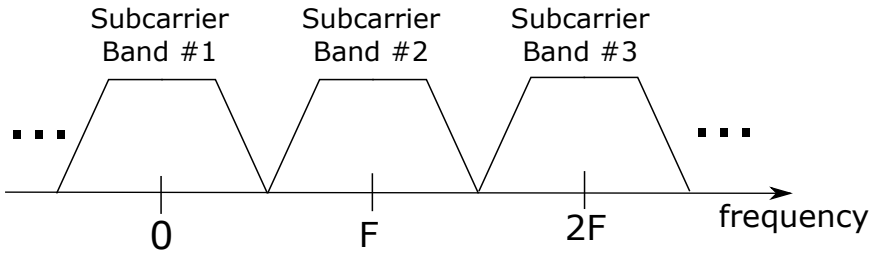

Figure 2.5: The locations of the non-overlapping subcarriers filtered with an RRC filter with roll-off factor α in the frequency axis

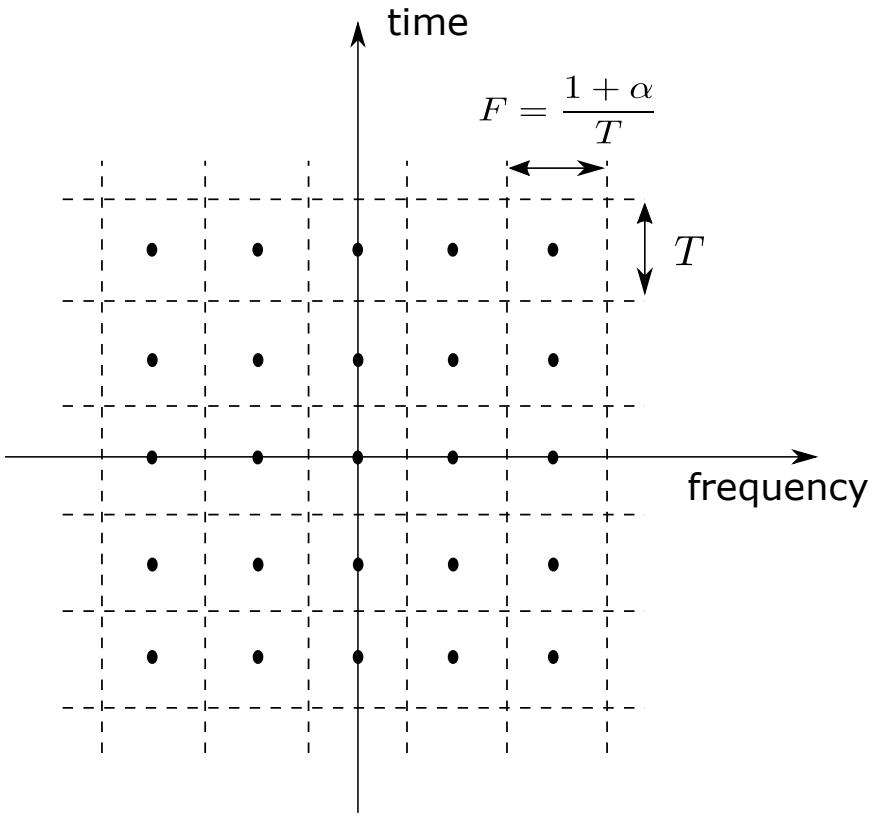

Figure 2.6: Time-frequency phase-space lattice representation of an FBMC system with an RRC filter with roll-off factor α

to the lattice representations is the symbol density in the lattice, which is defined as the number of symbol per unit area TF. For the lattice in Figure 2.6, the symbol density η can be calculated as

$$\eta = \frac{1}{TF} = \frac{1}{1+\alpha}. \tag{2.6}$$

The higher the symbol density in the lattice representation of the multicarrier communication method, the better the spectral efficiency of the communication system will be. As can be noted in (2.6), as the roll-off factor of the pulse-shaping filter in the transmitter increases, the symbol lattice density reduces.

That type of modulation where the subcarrier bands do not overlap as in Figure 2.5 corresponds to the classical frequency division multiplexing (FDM) communications scheme. However, there exist FBMC schemes for which the subcarrier bands overlap, which in turn increases the lattice density and the spectral efficiency. OFDM can be an example for such schemes in which the subcarrier bands overlap.

Other type of FBMC schemes are the ones for which the transmitted symbols $d_{m,k}$ have real values. In this case, OQAM type modulation is applied instead of QAM, which yields the following transmitted signal $x(t)$.

$$x(t) = \sum_{k}\sum_{m} d_{k,m} p(t - mT/2) e^{j2\pi t f_k} e^{j\phi_{k,m}} \tag{2.7}$$

where $p(t)$ is the impulse response of the pulse shaping filter, f_k is the location of the subcarriers in the frequency domain and $d_{k,m}$ is the data transmitted at the k^{th} subcarrier and the m^{th} symbol interval. Note that the symbol spacing along the time axis has become T/2 in (2.7) whereas the symbol spacing in time for the FBMC expression (2.5) is T. Furthermore, an important point in (2.7) is related to the $e^{j\phi_{m,n}}$ term. It can be selected arbitrarily without causing any ISI or ICI [4]. For example, it was chosen as $e^{j(k+m)\pi/2}$ in [5]. For that specific value of $e^{j\phi_{m,n}}$, when $k+m$ has even values, this term can be considered as having no effect in that the real-valued nature of $d_{k,m}$ do not change. However, when $k+m$ has an odd value, it introduces a phase shift of $\pm\pi/2$. This concept is presented in Figure 2.7 with a time-frequency phase-space lattice [5].

As can be observed in Figure 2.7, the points with orange color represent the symbols with a phase shift of $\pm\pi/2$ and the blue points correspond to no effective phase

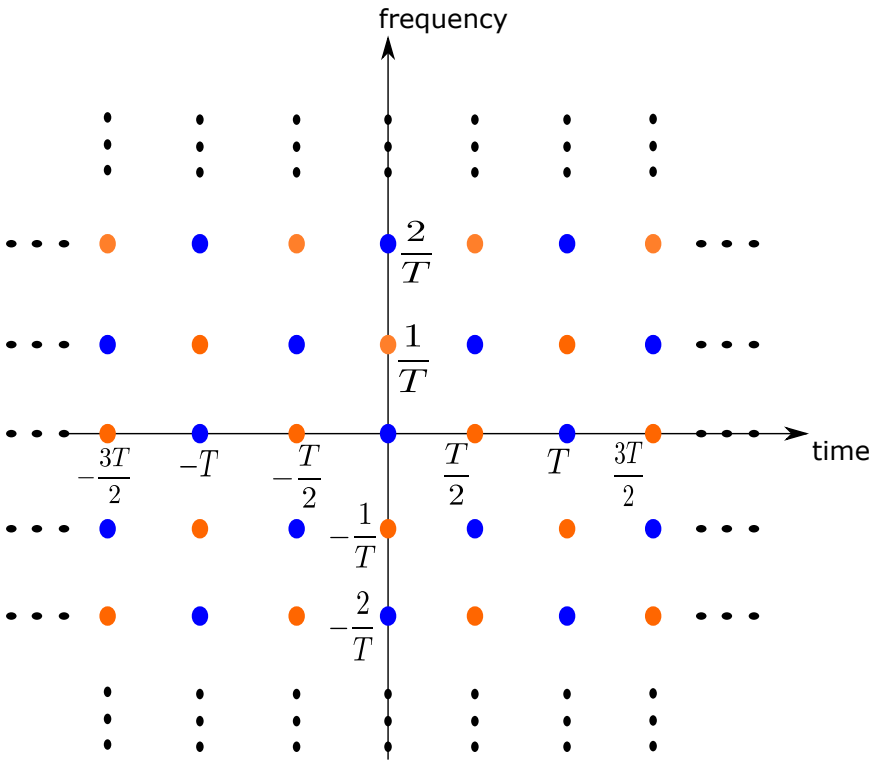

Figure 2.7: Time-frequency phase-space lattice representation for FBMC with real valued symbols

shift, that is, the real valued nature of the symbols does not change for blue points. Furthermore, the receiver structure has also differences from the FBMC modulation with complex QAM type symbols. The receiver for FBMC with real valued symbols is composed of matched filters as in FBMC with complex valued symbols. On the other hand, the real or imaginary values of the matched filter outputs are taken for the FBMC schemes with real valued symbols. A possible transmitter and receiver structure, whose transmitted signal can be characterized by (2.7), is demonstrated in Figure 2.8. [5].

This type of FBMC whose system structure is given in Figure 2.8 is referred to as offset-QAM-OFDM (OQAM-OFDM) or staggered multitone (SMT). The structure is mainly proposed by Saltzberg [18]. In fact, the reason why OQAM term is used is obvious. As can be observed in Figure 2.8, the real and the imaginary parts of the QAM signals are transmitted with a timing offset of $T/2$.

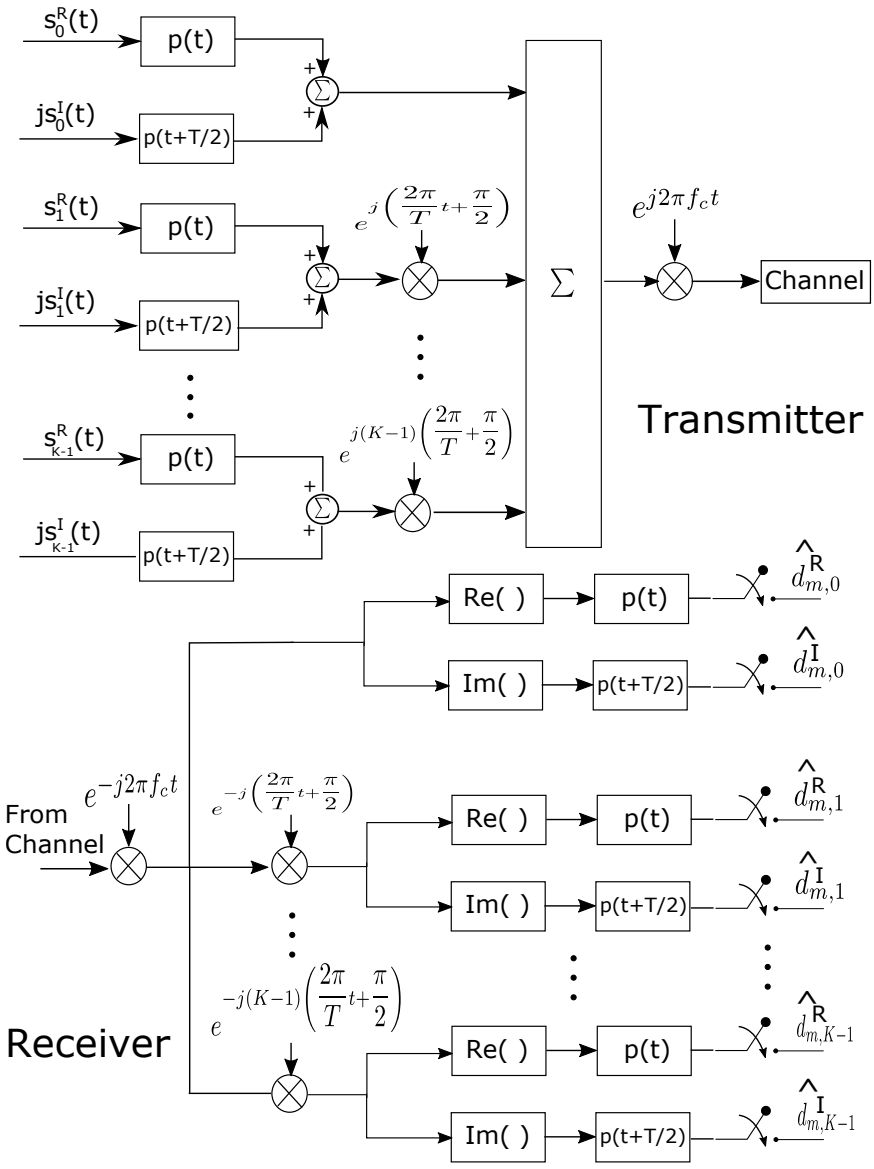

Figure 2.8: The transmitter and receiver structure of OQAM-OFDM or SMT

There is also another variation of SMT named as cosine modulated multitone (CMT). This is first proposed by Chang [19]. Then, the more recent name CMT is suggested in [20]. There is a little difference between CMT and SMT. In SMT, the subcarriers are modulated with DSB modulated filter banks. However, in CMT the filter-banks are composed of vestigial-sideband (VSB) type filters. Accordingly, the time-frequency phase-space lattice representation of CMT has some differences compared to SMT. For a more detailed examination of CMT, the reader is suggested to refer to [5].

However, the most important modulation types in this thesis that are discussed in this chapter are OFDM and OQAM-OFDM. OFDM will be a reference modulation type and other modulation types that are candidates to be used in 5G systems such as generalized frequency division multiplexing (GFDM) and windowed cyclic prefix circular offset QAM (WCP-COQAM) will be compared to OFDM. Furthermore, the reason why OQAM-OFDM is important is covered in the subsequent chapters in terms of the relation between OQAM-OFDM and WCP-COQAM. The details about the modulation type WCP-COQAM will also be examined in Chapter 3.

CHAPTER 3

GENERALIZED FREQUENCY DIVISION MULTIPLEXING

3.1 GFDM: A New Modulation Technique for the Next Generation Communications

Generalized frequency division multiplexing (GFDM) is a multicarrier modulation technique proposed by Fettweis et al. [7]. It is a special case of filter bank multicarrier (FBMC) modulation scheme in that there is a pulse shaping filter for each subcarrier in the transmitter. On the other hand, it has similarity to OFDM in that OFDM's block structure with cyclic prefix is also present in GFDM. This makes the linear and circular convolution between the transmitted sequence and the channel to be equivalent, which makes single tap equalization of the multipath ISI channel. The frame structure for OFDM and GFDM are presented in Figure 3.1.

As can be observed from Figure 3.1, while an OFDM frame has a cyclic prefix for the transmission of every symbol of K subcarriers, a GFDM frame has a single cyclic prefix (CP) for M GFDM symbols, each of which contains K subcarriers. This becomes possible since a single cyclic prefix is sufficient to ensure that the linear convolution with the channel is equivalent to circular convolution, which enables single tap equalization to be performed over the whole GFDM frame consisting of $M \cdot K$ samples. Therefore, the transmission of $M \cdot K$ constellation symbols using only a single cyclic prefix is possible for GFDM, whereas in OFDM, M cyclic prefix intervals are needed for the transmission of $M \cdot K$ constellation symbols. In that case, the efficiency losses resulting from cyclic prefix overhead for OFDM and GFDM, which can be denoted as η_{OFDM} and η_{GFDM} , respectively, can be written as

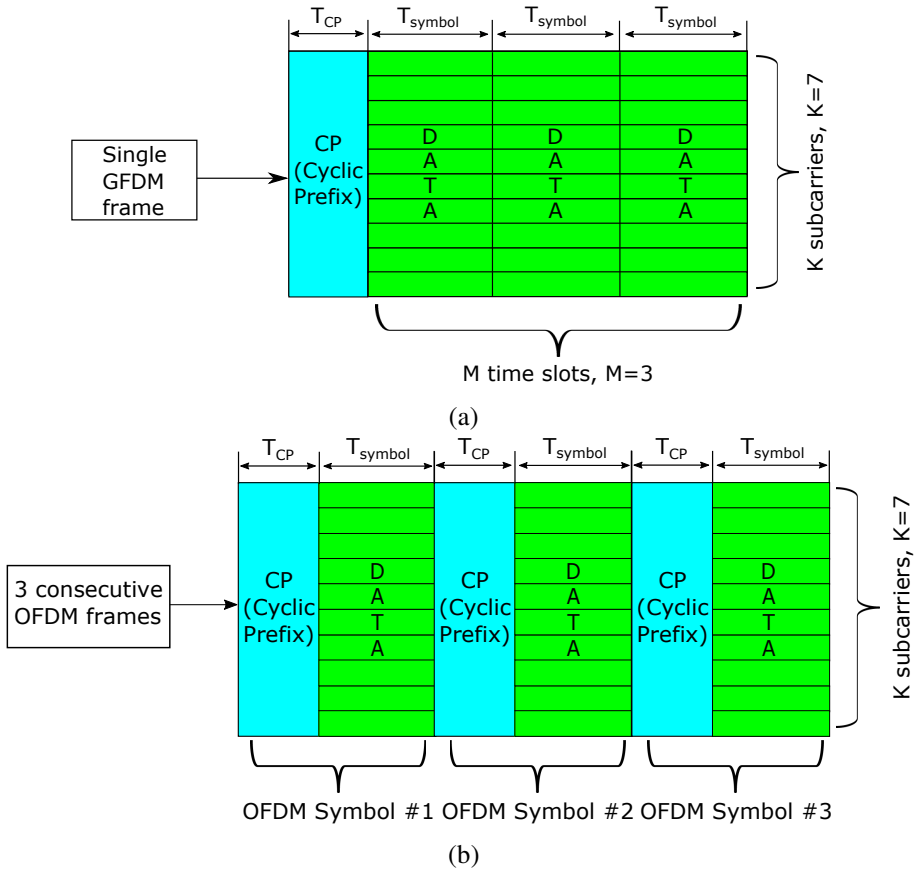

Figure 3.1: (a) A GFDM frame composed of 3 consecutive GFDM symbols. (b) An OFDM frame consisting of 3 consecutive OFDM symbols

$$\eta_{OFDM} = \frac{T_{symbol}}{T_{CP} + T_{symbol}} \tag{3.1}$$

$$\eta_{GFDM} = \frac{M \times T_{symbol}}{M \times T_{symbol} + T_{CP}} \tag{3.2}$$

where T_{symbol} is equal to OFDM symbol duration and it is equal to $1/M$ of the total duration of the GFDM frame excluding the cyclic-prefix interval duration, if the transmission bandwidth is equal for OFDM and GFDM, which makes T_{symbol} to be the same for OFDM and GFDM. In that case, according to (3.1) and (3.2), the spectral efficiency of GFDM will be higher than that of OFDM for $M > 1$. As M gets higher and higher, η_{GFDM} goes to 1, which corresponds to the case that there is no efficiency loss due to CP overhead. However, the trade-off for high M is the latency caused by the requirement that whole GFDM frame (consisting of M GFDM symbols) should be received to demodulate the data content. Furthermore, the assumption that channel should not change very much within the GFDM frame in order to be able to perform

block equalization at the receiver may not apply if the number of GFDM symbols within a GFDM frame is increased. However, a similar situation may also be a concern even for $M = 1$ for GFDM or OFDM [21]. Therefore, the time-variation of a channel which is characterized by its coherence time [1] should be considered along with the latency requirements of the application while the number of GFDM symbols in a GFDM frame is designed.

Although GFDM seems to be superior to OFDM considering the above mentioned efficiency losses due to CP overhead, most of the simulations that is included in this thesis will be done under equal spectral efficiency conditions, that is, instead of transmitting K subcarriers in OFDM, $M \cdot K$ subcarriers will be transmitted using the same bandwidth as GFDM. This corresponds to the case that $M \cdot K$ subcarriers are transmitted in an OFDM symbol duration of $M \cdot T_{symbol}$ which ensures the same spectral efficiency loss for OFDM and GFDM.

Although a GFDM frame consisting of 3 GFDM symbols, which is depicted in Figure 3.1a, is referred to as a "GFDM frame", in the literature, most of the references refer to this block as a "GFDM symbol", which is composed of sub-symbols. However, for convenience, unlike the literature, we refer to a "GFDM symbol" as "GFDM frame", and "GFDM sub-symbols" as "GFDM symbols".

3.2 GFDM Transreceiver

GFDM Transreceiver block diagram can be found in Figure 3.2 [7].

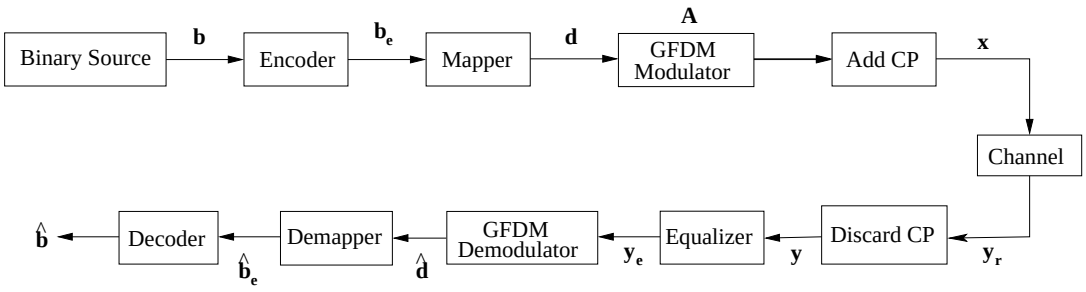

Figure 3.2: GFDM transreceiver block diagram

In Figure 3.2, the binary data, $\mathbf{b}$, is encoded (with any possible error control coding scheme) to get $\mathbf{b_e}$. Then the mapper maps its binary inputs to the constellation points to yield $\mathbf{d}$. After that, GFDM modulator, which can be represented as a multiplication by a matrix $\mathbf{A}$, modulates the constellation symbols according to the rules of GFDM modulation. Before transmission to channel, cyclic prefix is added, as in OFDM. At the receiver side, after CP removal and equalization, the received discrete signal is de-modulated with a GFDM demodulator, which outputs the soft constellation symbols. After de-mapping and decoding, estimates of the transmitted bits are obtained.

3.3 GFDM Signal Model

The transmitted signal with GFDM is given as follows.

$$x[n] = \sum_{m=0}^{M-1} \sum_{k=0}^{K-1} d_{k,m} p[(n - mK)_N] g_k[n] \tag{3.3}$$

where M is equal to the number of GFDM symbols in a GFDM frame and K refers to the number of subcarriers. $d_{k,m} \in A_X$, where A_X is the input alphabet of the source to be transmitted, is the data symbol transmitted at the k^{th} subcarrier and m^{th} GFDM symbol in GFDM frame. $p[n]$ refers to the pulse shaping filter impulse response of length N. In 3.3, $p[(n-mK)_N]$ represents the circular shift $p[n]$ by mK with modulo N, where N equals to $N = M \cdot K$. $g_k[n]$ is the complex exponential multiplier term that shifts the base-band spectrum to k^{th} subcarrier location, which is given in 3.4.

$$g_k[n] = e^{-j2\pi k \frac{n}{N}}. \tag{3.4}$$

3.4 GFDM Transmitter

GFDM transmitter [22], which corresponds to GFDM modulator block in Figure 3.2, can be seen in Figure 3.3.

In Figure 3.3, $d_{m,k}$ refers to the data symbol transmitted at the k^{th} subcarrier and m^{th} GFDM symbol. There are a total of $M \cdot K$ data symbols on the left side of the transmitter. In addition, as stated before, $p[(n - K)_N]$ refers to the circular shift of the pulse shape with modulo N. Here, $N = M \cdot K$. This circular shifting structure

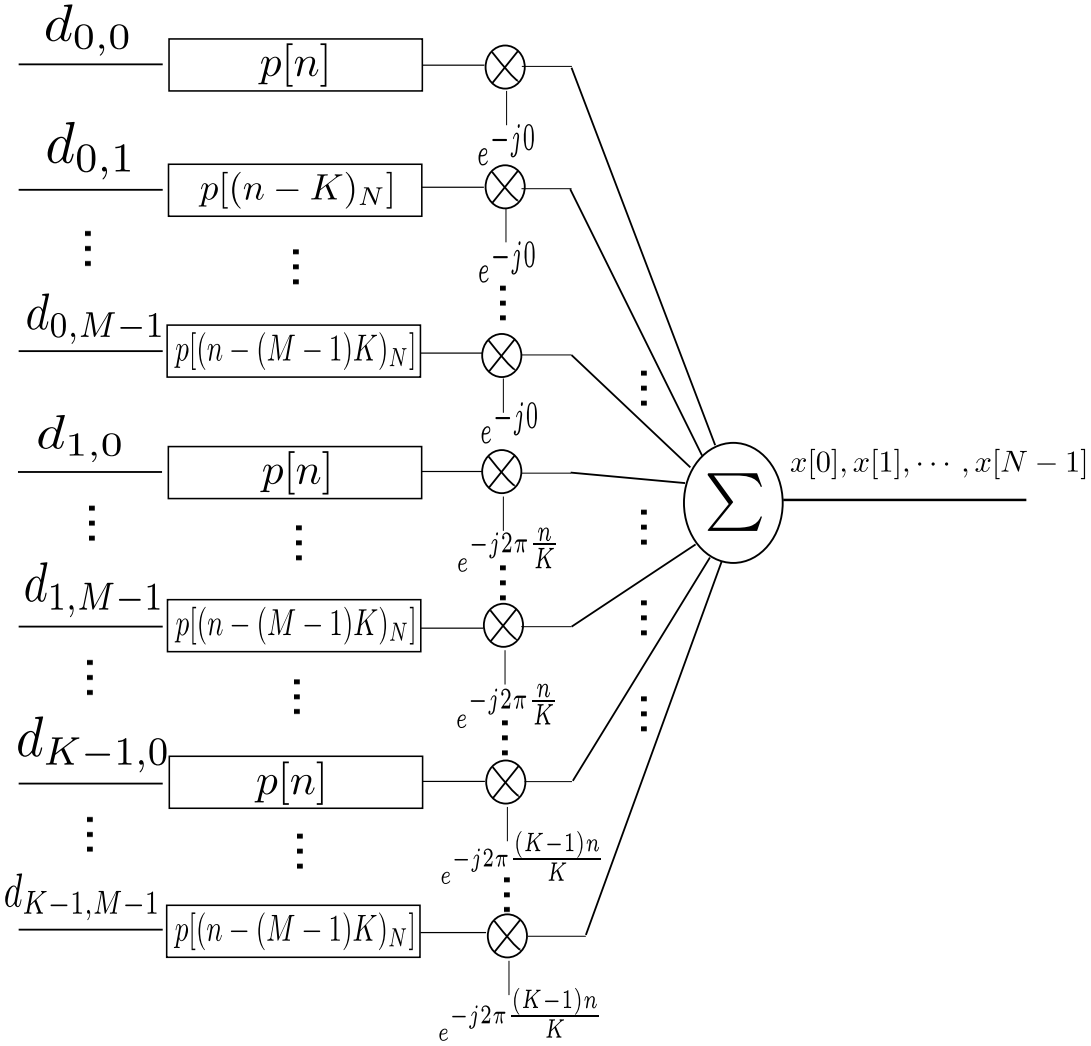

Figure 3.3: GFDM transmitter

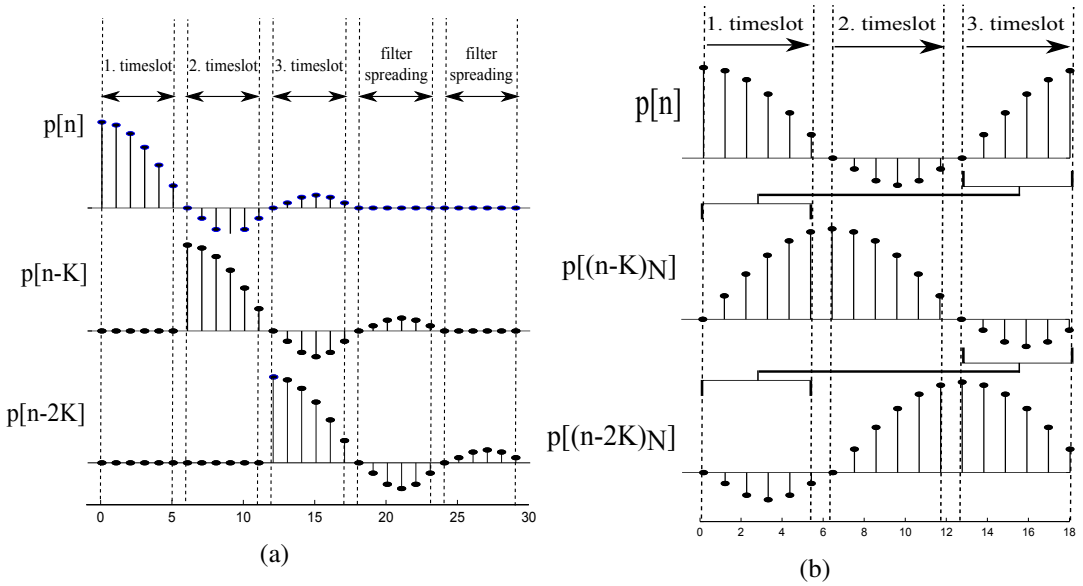

Figure 3.4: Linear (a) and circular (b) convolution based signalling

is important in that if it were a delay rather than a circular shift, which corresponds to conventional linear filtering, the cyclic prefix length should also account for the delay caused by transmit filtering. To better illustrate this, Figures 3.4a and 3.4b show the difference between conventional linear filtering and filtering using circular convolution for $M = 3$ [23].

In Figure 3.4b the addition of the last K samples to the beginning of the delayed versions of transmit filters generates a circular shifted version of $p[n]$. This technique is called tail-biting in some studies [24], [25]. While it ensures that cyclic prefix length is independent of the transmit filter length, it also enables frequency domain implementation for transmit filtering, which can reduce computational complexity for high transmit filter lengths [26] (especially for high $M \cdot K$ values). Furthermore, note from Figure 3.4b that there is even symmetry in $p[n]$. This is important in that only if $p[n]$ is even symmetric and CP is longer than the channel delay spread, any linear convolution with the channel response becomes equivalent to circular convolution, which results in a circulant channel convolution matrix. This makes single tap equalization possible on the receiver side as in OFDM [1].

3.5 GFDM Modulator Model

The output of the GFDM transmitter, x[n], in Figure 3.3, can be written as in (3.3). Defining $p_m[n] \triangleq p[(n - mK)_N]$, (3.3) can be reexpressed as

$$x[n] = \sum_{m=0}^{M-1} \sum_{k=0}^{K-1} d_{k,m} p_m[n] g_k[n]. \tag{3.5}$$

It is also possible to express (3.5) as a multiplication of a matrix $\mathbf{A}$ with a transmitted data vector $\mathbf{d}$ as follows.

$$\mathbf{x} = \mathbf{A}\mathbf{d} \tag{3.6}$$

where

$$\mathbf{x} = \begin{bmatrix} x[0] \\ x[1] \\ \vdots \\ x[MK-1] \end{bmatrix}, \mathbf{A} = \begin{bmatrix} p_0[n]g_0[n] \\ p_0[n]g_1[n] \\ \vdots \\ p_0[n]g_{K-1}[n] \\ p_1[n]g_0[n] \\ p_0[n]g_1[n] \\ \vdots \\ p_{M-1}[n]g_{K-1}[n] \end{bmatrix}^T, \mathbf{d} = \begin{bmatrix} d_{0,0} \\ d_{1,0} \\ \vdots \\ d_{K-1,0} \\ d_{0,1} \\ d_{1,1} \\ \vdots \\ d_{K-1,M-1} \end{bmatrix}. \tag{3.7}$$

Such a simple expression of the transmitted vector $\mathbf{x}$ in terms of the vector containing unmodulated symbols to be transmitted, $\mathbf{d}$, will be useful in expressing the operations of different types of GFDM receivers, which is explained in the following Section 3.6.

3.6 GFDM Receiver

The basic block diagram of a GFDM receiver is given in Figure 3.5 [23].

The samples from the sampler in the RF front end block is denoted as $y_{cp}[n]$. The CP portion of it is removed to get $y[n]$. Subsequently, the equalizer block equalizes the effect of the channel with the estimated channel values provided by the channel estimation block. This equalization is performed as a single tap equalization, since

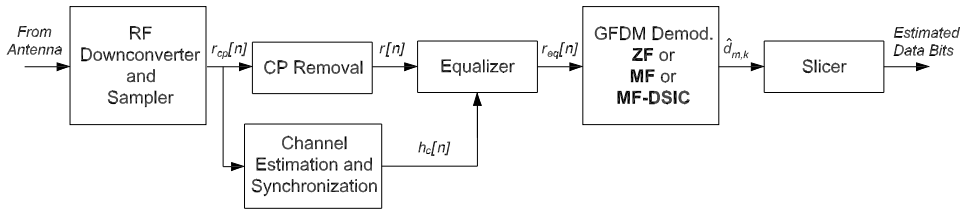

Figure 3.5: GFDM receiver block diagram

the structure of GFDM allows such a block equalization as mentioned in the previous sections. The equalized signal $y_{eq}[n]$ is fed to the GFDM demodulator, which yields the soft data bits. The slicer makes the hard decisions.

The single tap equalization procedure is simply run as

$$y_{eq}[n] = \mathbf{IFFT}\left[\frac{\mathbf{FFT}[y[n]]}{\mathbf{FFT}[h_c[n]]}\right] \tag{3.8}$$

thanks to the block structure of the GFDM symbol with a cyclic prefix that results in a circulant convolution matrix. After equalization, the equalized samples are fed to the GFDM demodulator. The demodulator can be of three types, namely Matched Filter (MF), Zero-forcing (ZF) or Matched Filter followed by a Double Sided ICI Cancellation (MF-DSIC) [23], which will be detailed in the following sections. It should also be stated that, in the following parts, the term "receiver" is used instead of "demodulator".

3.6.1 Matched Filter (MF) Receiver

The matched filter (MF) GFDM receiver can be implemented as a correlator receiver, as shown in Figure 3.6 [23].

As can be seen, each correlator is matched to a different time slot (to a different GFDM symbol time interval) and a different subcarrier. After multiplication of the received signal $y_{eq}[n]$ with appropriately circularly shifted versions of the pulse shape $p[n]$ and complex exponentials, summation is done over an interval of MK and the result is sampled. This is the classical integrate-dump operation used in a correlation

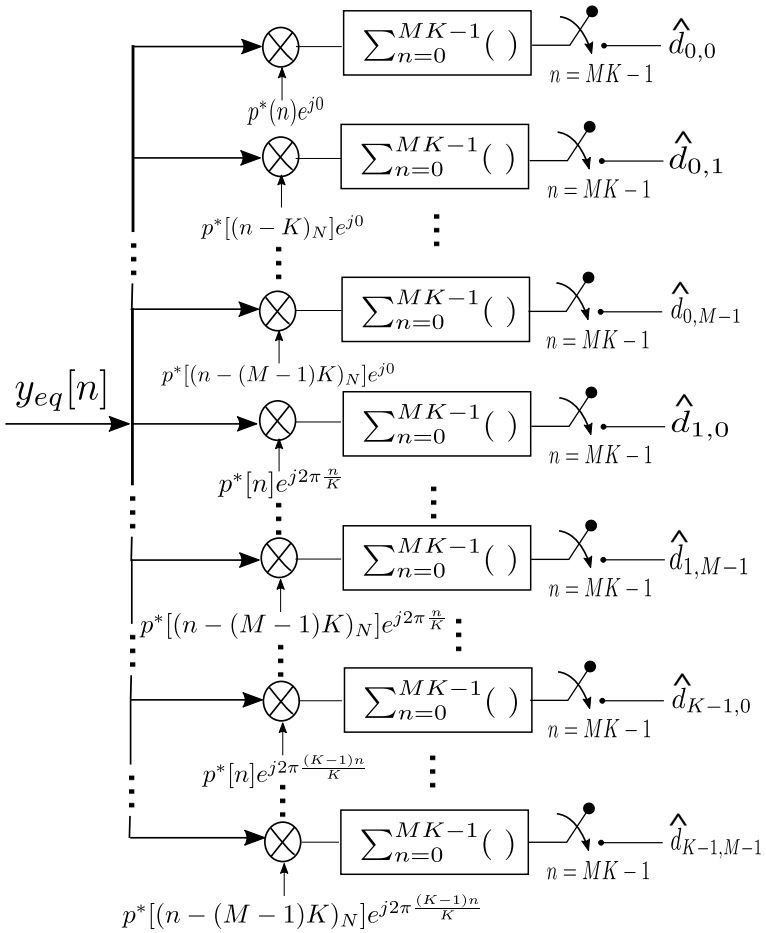

Figure 3.6: GFDM MF receiver

receiver. Such an operation in fact corresponds to multiplication of the equalized version of the received signal, $y_{eq}[n]$ with $\mathbf{A^H}$. In this case the vector of estimated soft bits, $\hat{\mathbf{d}}_{\mathbf{MF}}$ can be expressed as

$$\hat{\mathbf{d}}_{\mathbf{MF}} = \mathbf{A^H y_{eq}} \tag{3.9}$$

where $\mathbf{y_{eq}} = [\ y_{eq}[0]\ y_{eq}[1]\ \ldots\ y_{eq}[MK-1]\ ]^T$. Such a receiver does not guarantee that there is zero inter-symbol interference (ISI) or inter-carrier interference (ICI) which will cause interference between the elements of the transmitted vector $\mathbf{d}$. This depends on the selection of the pulse shape $p[n]$. For instance, if it is a root-raised cosine spectrum pulse, there will be zero ISI. However, ICI will still not be guaranteed to be equal to zero. Therefore, if MF receiver will be used, the selection of the pulse shape should be made carefully, considering the possible non-orthogonalities in time (which will cause ISI) or frequency (which will be responsible for ICI). More details on the selection of orthogonal pulses that will not cause ISI or ICI if an MF receiver is used will be discussed in Chapter 4.

3.6.2 Zero-forcing Receiver

Zero forcing (ZF) receiver is simply the multiplication of $\mathbf{y_{eq}}$ by the inverse of the matrix $\mathbf{A}$. In this case,

$$\hat{d}_{MF} = \mathbf{A^{-1} y_{eq}}. \tag{3.10}$$

Unlike MF receiver, ZF receiver is able to completely remove ISI and ICI. However, the downside of ZF receiver can be a possible noise enhancement, which will degrade SNR at the receiver.

3.6.3 Matched Filter Receiver Followed by Double Sided Interference Cancellation

MF-DSIC is a type of receiver that cancels the interference between the adjacent subcarriers proposed by [23]. It is most useful when most of the interference in the received signal is owing to ICI and this ICI is mostly present between the neighbouring subcarriers. For example, this is the case when an RRC pulse is used for transmission.

With MF type receiver on the demodulator side, the interference between the GFDM symbols will only be due to ICI, thanks to the fact that raised cosine spectrum (RC) pulse (which is obtained with matched-filtering of an RRC pulse) is a Nyquist-1 type pulse [27]. The ICI will also be mostly originating from the neighbouring subcarriers, intensity of which is determined by the roll-off factor of the RRC pulse chosen. The MF-DSIC receiver block diagram is given in Figure 3.7 [23].

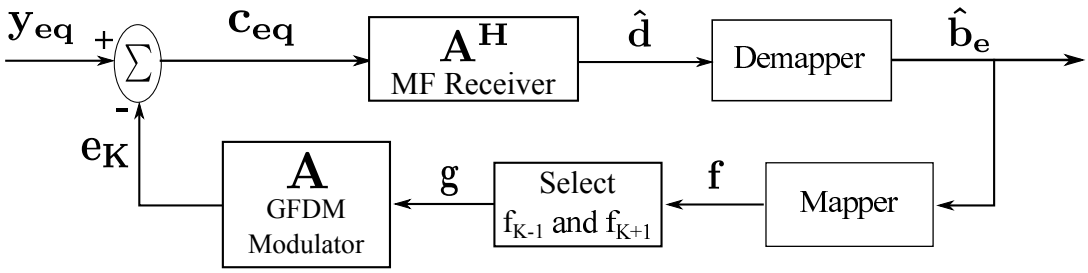

Figure 3.7: GFDM MF-DSIC receiver block Diagram

As can be seen in Figure 3.7, firstly the input signal, $\mathbf{y_{eq}}$ is matched filtered. After matched filtering, hard decisions are made from $\hat{\mathbf{d}}$, which will yield $\hat{\mathbf{b}}_\mathbf{e}$, which is again mapped to their corresponding constellation points to yield $\mathbf{f}$. From $\mathbf{f}$, only the symbols in the $(k-1)^{th}$ and $(k+1)^{th}$ subcarriers are selected, and the rest of the symbols are mapped to zero to form the vector $\mathbf{g}$ which is fed to GFDM modulator again. The output of the GFDM modulator, $\mathbf{e_k}$ is subtracted from the input vector $\mathbf{y_{eq}}$ and this procedure is followed for all k values to finish one iteration of interference cancellation. The number of iterations can be increased to get more accurate results. Trade-off is the increased complexity owing to the higher number of iterations.

3.7 Windowed Cyclic-Prefix Circular Offset QAM

WCP-COQAM is a modification of GFDM by modulating the constellation symbols with an OQAM type of modulation which is offered by Lin and Siohan [17]. The transmitted signal with WCP-COQAM can be written as

$$x_{WCP-COQAM}[n] = \sum_{k=0}^{K-1} \left\{ \sum_{m=0}^{M-1} d_{k,m}^{\Re} \tilde{g}_k[n] p[(n - mK)_N] + \sum_{m=0}^{M-1} j d_{k,m}^{\Im} \tilde{g}_k[n] p[(n + K/2 - mK)_N] \right\}. \tag{3.11}$$

As can be seen in (3.11), the application of OQAM modulation shows itself in that the real part of $d_{k,m}$, which is denoted as $d_{k,m}^{\Re}$ in (3.11), is transmitted with a delay of $K/2$ with respect to the transmission of the imaginary part of $d_{k,m}$, which is referred to as $d_{k,m}^{\Im}$ in (3.11). In (3.11), $\tilde{g}_k[n] = g_k[n]e^{-j\pi\frac{k}{K}\alpha}$ where $\alpha = \frac{K}{2} - 1$.

By using OQAM type of modulation, it is possible to preserve orthogonality both in frequency domain (between the subcarriers) and in time-domain (between the sub-symbols in a GFDM frame) by using pulse shapes other than the rectangular pulse shape [28] while maintaining the same spectral efficiency [29]. If OQAM is not used, the only possible pulse shape that satisfies such an orthogonality is the rectangular type pulse shape [28]. The reason for using pulse shapes other than the rectangular pulse shape is to use pulses that have better spectral properties such as being prone to carrier frequency offset (CFO) [3], [4], [5] or having lower out-of-band (OOB) radiation [5], [7]. Here, having better spectral properties corresponds to having better localization in frequency domain, that is, the frequency response of the pulse-shaping filter decays faster in frequency domain, which obviously will result in less OOB radiation and immunity to CFO. In fact, this orthogonality enables the use of matched filter receiver instead of a zero-forcing receiver, which may cause noise enhancement, or MMSE receiver, which may also be responsible of some amount of noise enhancement although less than ZF receiver.

3.8 Simulation Results

In this section, error rate performances of OFDM, GFDM (with three different receiver structures mentioned in Section 3.6) and WCP-COQAM (with an MF receiver) under CFO will be inspected. These performances will be observed under different

channels. The first channel type that is included in the simulations is an AWGN channel. Another channel type that is used in the simulations is a static ISI channel, specified by the COST-207 hilly terrain model [27]. The last channel type is the Rayleigh faded version of the COST-207 channel, that is, the power of each channel tap will be exponentially distributed with an average power corresponding to the tap powers specified in the power-delay profile of the COST-207 hilly terrain model. The pulse shapes that will be used are raised-cosine (RC), root-raised cosine (RRC) and Dirichlet pulses. Here, the Dirichlet pulse is a pulse that is also referred to as the discrete sinc or aliased sinc, whose DTFT produces a rectangular pulse. Since it is used in time-domain in GFDM, it will be a rectangular pulse in frequency domain. In that respect, GFDM will be an "inverse OFDM" since rectangular pulse is used in OFDM in time domain, rather than in frequency domain. In that case, Dirichlet pulse is expected to present no ISI or ICI under ideal conditions, that is, the channel is perfectly equalized and there is no ISI or ICI owing to timing and frequency synchronization errors between the transmitters and receivers or due to any doppler effect. Simulation parameters are given in Table 3.1.

The reason for choosing 128 subcarriers here is that in the simulations related to out-of-band emissions and spectral mask compliance which are presented in Chapter 5, the number of subcarriers are selected amongst possible choices that are specified in LTE standard [13]. 128 is one of the possible choices. Furthermore, since the comparison of OFDM and GFDM or WCP-COQAM at equal spectral efficiency conditions is desired, the number of subcarriers for OFDM is $M \cdot K = 1152$. Moreover, note also that the number of GFDM symbols in a GFDM frame (M) is chosen to be an odd number. This is important in that ZF receiver in GFDM does not perform well when the number GFDM symbols in a GFDM frame (M) is an even number [30]. Amongst the possible odd numbers, the reason for selecting $M = 9$ is in order to have the same M value as in [7] for the out-of-band radiation comparison simulations.

As stated before, the simulations are performed under equal spectral efficiency conditions. Therefore, the expectation is that GFDM and WCP-COQAM should give a better performance under CFO, since pulse shaping is applied in GFDM or in WCP-COQAM, which results in the use of pulses that have better localization in frequency domain than that of the rectangular pulse used in OFDM.

Table 3.1: Simulation Parameters

Pulse shape	RC, RRC or Dirichlet
Roll-off factor	0.1 or 0.3
No. of subcarriers (K)	128 for GFDM, $128 \cdot 9$ in OFDM
No. of GFDM symbols (M)	9
CP length	72
No. of iterations for MF-DSIC receiver	3
Constellation order	4 (QPSK)
Channel	AWGN or COST 207 (Static ISI or Rayleigh Fading)
Sampling rate	1 MHz
Carrier frequency offset (CFO)	0, 50 Hz or 100 Hz
No. of Monte-Carlo trials	Trials continue until at least 100 frame errors are collected

3.8.1 Simulation Results in AWGN

In AWGN, SER curves of OFDM, GFDM and WCP-COQAM under CFO are given in Figures 3.8-3.10 when RRC, RC pulses with roll-off factor 0.1 or Dirichlet pulses are used for GFDM and WCP-COQAM.

From Figures 3.8-3.10, one may note that the theoretic SER vs. SNR performance for OFDM in AWGN is given as a curve named as "OFDM Theory". This curve is plotted according to the approximate symbol error probability expression of OFDM with M'-QAM (M' is the constellation order) in AWGN given by [31], which is

$$p_e \approx \frac{4(\sqrt{M'}-1)}{\sqrt{M'}} Q\left(\sqrt{\frac{3E_s}{(M'-1)N_0}}\right) \tag{3.12}$$

The simulation results in Figures 3.8-3.10 show that OFDM performs the same as GFDM or WCP-COQAM for Dirichlet pulse under no CFO. This is an expected

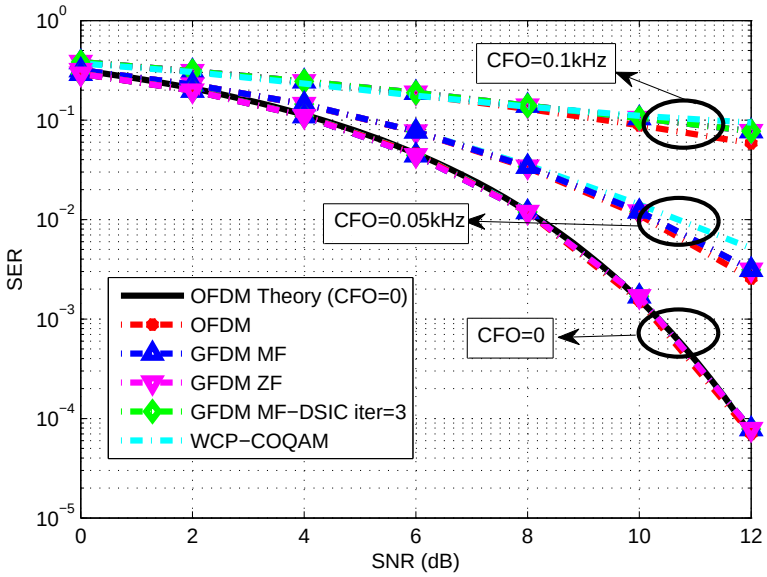

Figure 3.8: SER vs. SNR for OFDM, GFDM or WCP-COQAM with Dirichlet pulse under different CFO values in AWGN

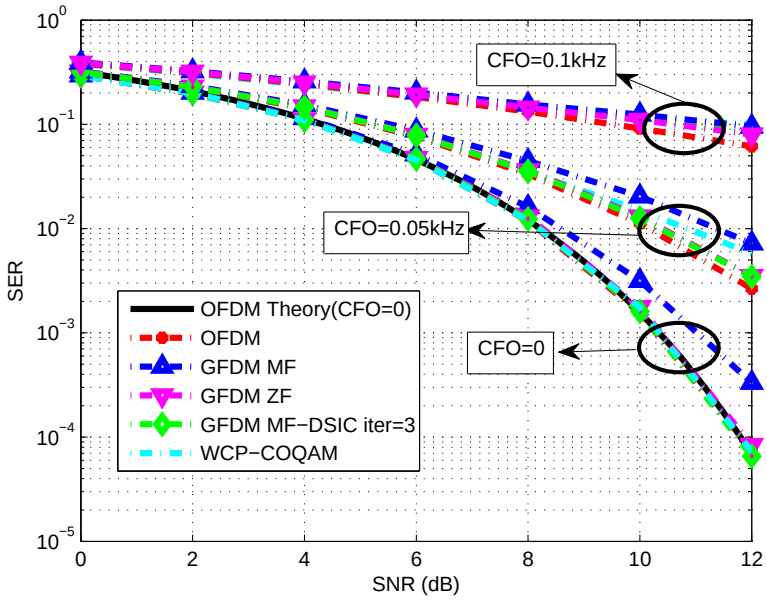

Figure 3.9: SER vs. SNR for OFDM, GFDM or WCP-COQAM with RRC pulse with roll-off factor 0.1 under different CFO values in AWGN

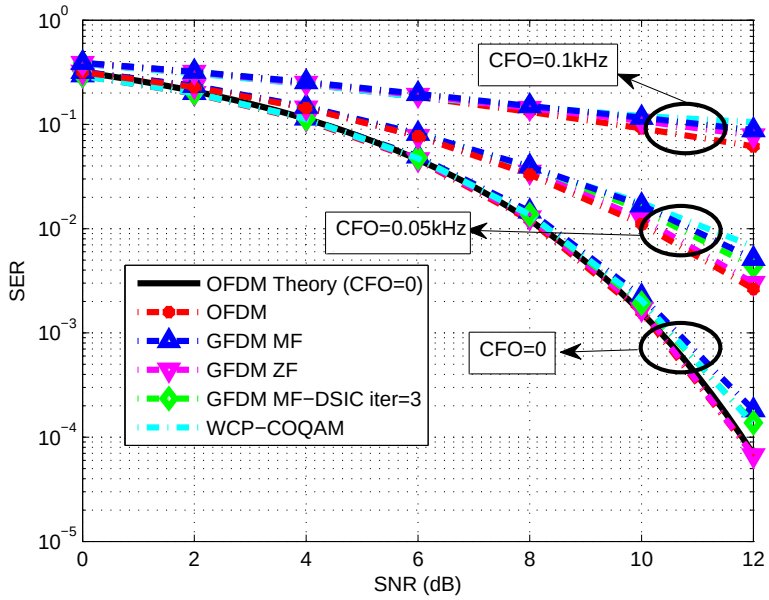

Figure 3.10: SER vs. SNR for OFDM, GFDM or WCP-COQAM with RC pulse with roll-off factor 0.1 under different CFO values in AWGN

result resulting from the zero ISI or ICI nature of the Dirichlet pulse. However, for non-zero CFO, when RC and RRC pulses are used in GFDM or WCP-COQAM, OFDM performs the best. The performance losses for the RC pulse are due to the created ISI and ICI for the case of MF receiver. Similarly for the RRC pulse, the created ICI is responsible for the performance losses compared to OFDM when MF receiver is used.

The most significant observation from the Figures 3.8-3.10 is that when CFO is nonzero, OFDM performs better than GFDM or WCP-COQAM in all cases regardless of the chosen pulse shape. Therefore, GFDM or WCP-COQAM with RC, RRC pulses with roll-off 0.1 or with Dirichlet pulse do not show any better CFO immunity performance compared to OFDM in AWGN. Therefore, SER vs.. SNR simulations are also performed for RC and RRC pulses with roll-off 0.3. The results are presented in Figures 3.11-3.12.

As can be observed from Figures 3.11-3.12, using RC or RRC pulses with roll-off factor 0.3 in GFDM or WCP-COQAM did not yield in any better CFO immunity performance compared to OFDM. Another observation is that GFDM MF receiver

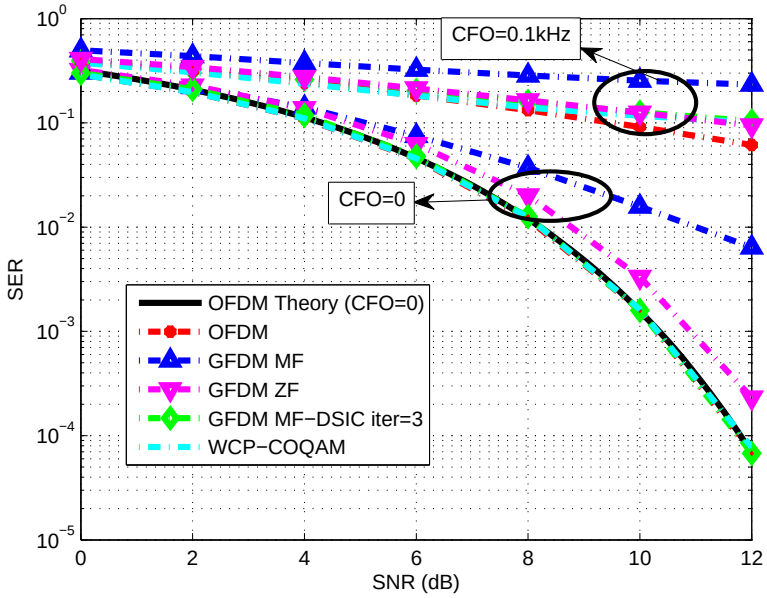

Figure 3.11: SER vs. SNR for OFDM, GFDM or WCP-COQAM with RRC pulse with roll-off factor 0.3 under different CFO values in AWGN

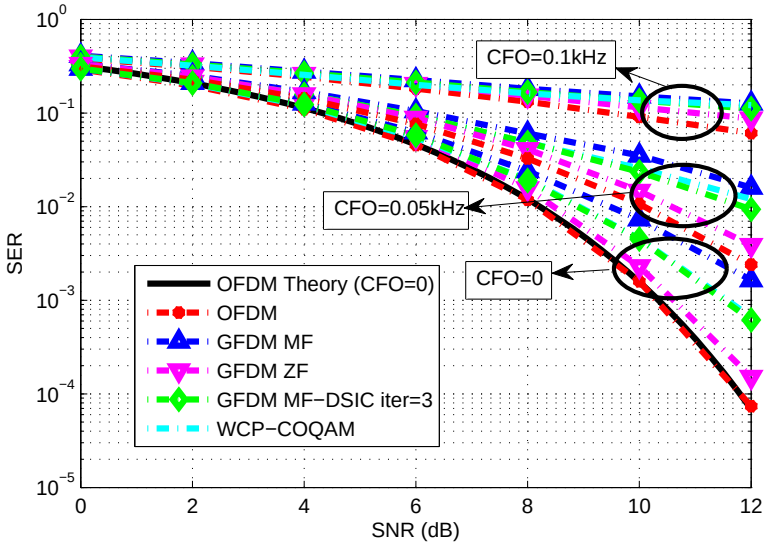

Figure 3.12: SER vs. SNR for OFDM, GFDM or WCP-COQAM with RC pulse with roll-off factor 0.3 under different CFO values in AWGN

yields poorer performance compared to the case for which roll-off factors are 0.1 since increased roll-off factor causes higher ICI with MF receiver.

3.8.2 Simulation Results with Static ISI COST 207 Channel

Similar simulations are also made with the channel created according to the power-delay profile dictated by the COST-207 Hilly Terrain Model. However, to limit the number of the simulations that is presented, RC or RRC pulses with only 0.1 roll-off factor is used in this section. The reason is that RC or RRC pulses with 0.1 roll-off factor revealed better results than that of RC or RRC pulses with 0.3 roll-off factor. The simulation results are given in Figures 3.13-3.15.

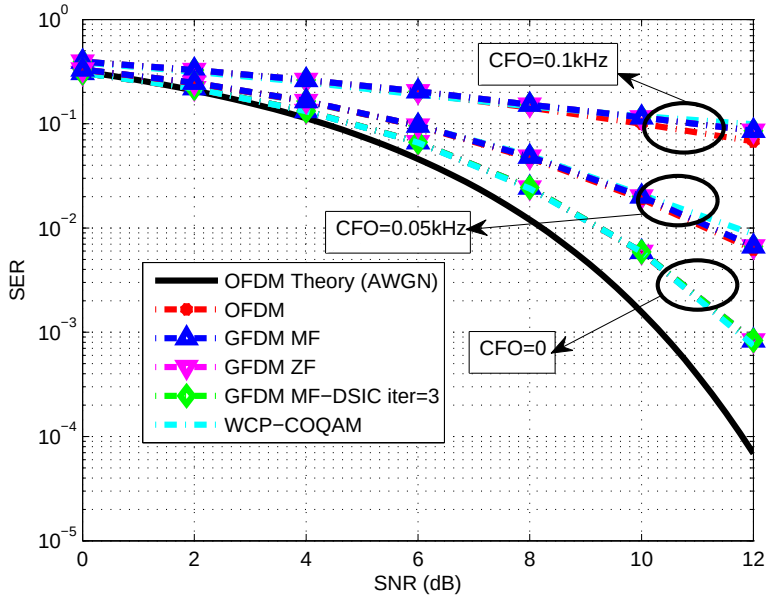

Figure 3.13: SER vs. SNR for OFDM, GFDM or WCP-COQAM with Dirichlet pulse under different CFO values in static ISI COST-207 channel

As can be observed from the above figures, there is a performance loss for COST-207 channel compared to the SER vs. SNR results observed in AWGN channel. This is an expected result, since single-tap equalization that is performed to equalize the multipath distortion as a result of the ISI channel is a zero-forcing type equalization

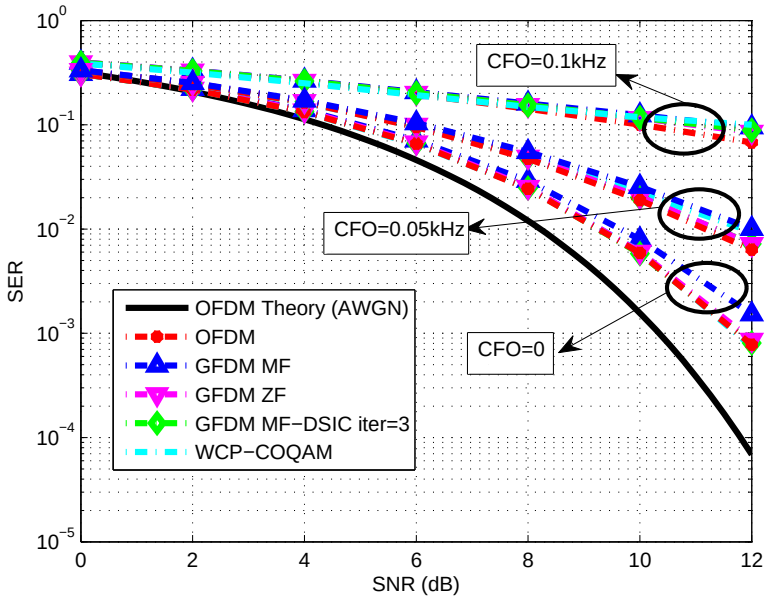

Figure 3.14: SER vs. SNR for OFDM, GFDM or WCP-COQAM with RRC pulse with roll-off factor 0.1 under different CFO values in static ISI COST-207 channel

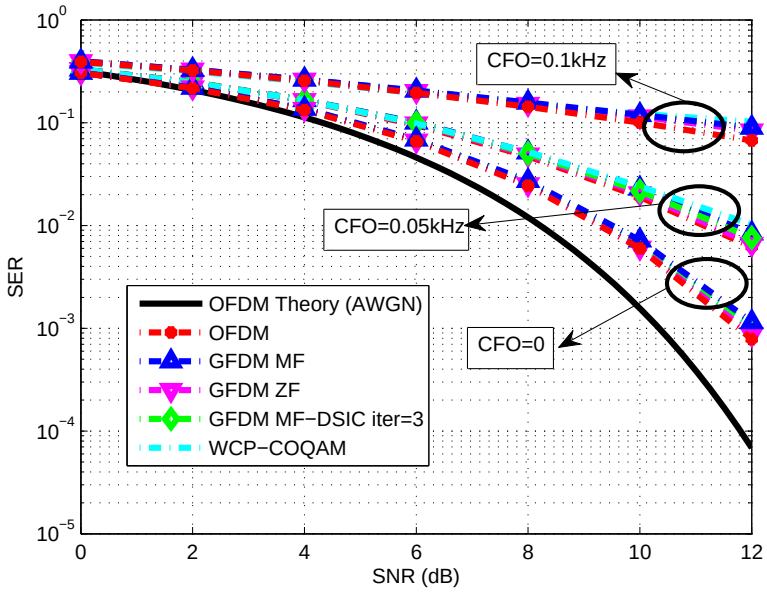

Figure 3.15: SER vs. SNR for OFDM, GFDM or WCP-COQAM with RC pulse with roll-off factor 0.1 under different CFO values in static ISI COST-207 channel

which is responsible for some amount of noise enhancement. The ISI created due to COST-207 channel is considered to be cancelled with single-tap equalization since the maximum delay spread of COST-207 which is about $20\mu s$ is shorter than the cyclic prefix length that is taken in the simulations, which is $72\mu s$. The main observation from the simulations is that there is no case that GFDM or WCP-COQAM performs better than OFDM under CFO also in COST-207 static ISI channel.

3.8.3 Simulation Results with Rayleigh Fading Cost-207 Channel

The simulations with the same parameters as in the ones made with the static ISI COST-207 channel are performed when Rayleigh fading is present in the COST-207 channel. Simulation results for RRC, RC pulses with roll-off factor 0.1 and Dirichlet pulses are presented in Figures 3.16-3.18.

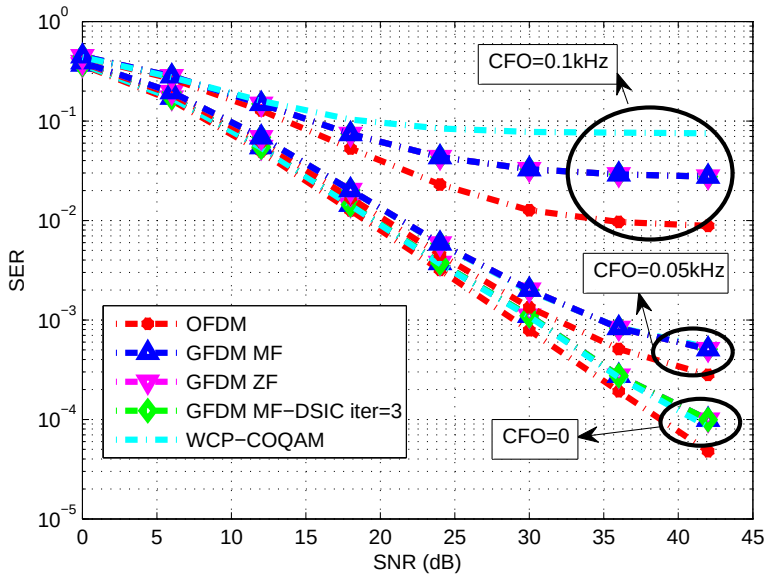

Figure 3.16: SER vs. SNR for OFDM, GFDM or WCP-COQAM with Dirichlet pulse under different CFO values in COST-207 Rayleigh fading channel

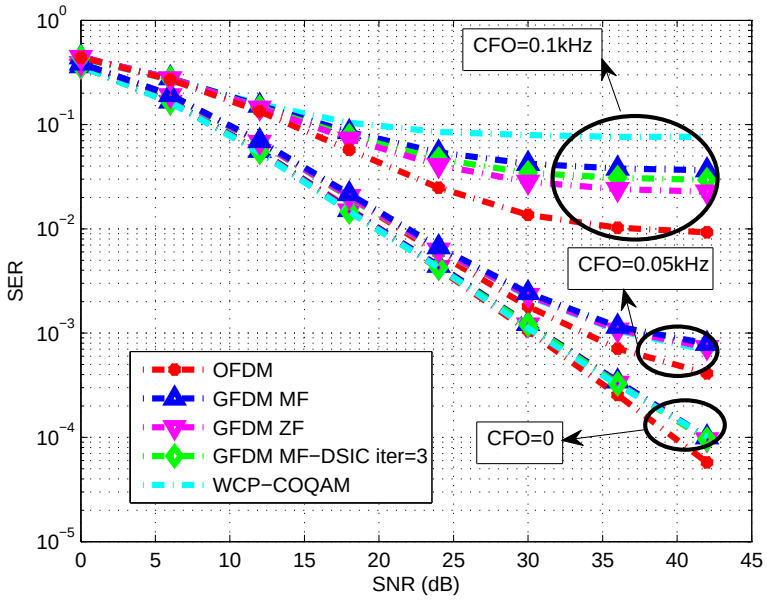

Figure 3.17: SER vs. SNR for OFDM, GFDM or WCP-COQAM with RRC pulse with roll-off factor 0.1 under different CFO values in COST-207 Rayleigh fading channel

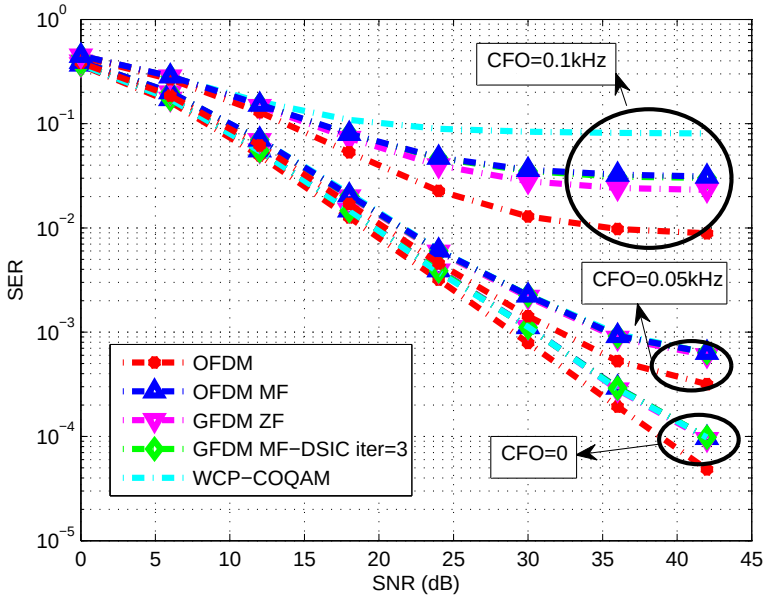

Figure 3.18: SER vs. SNR for OFDM, GFDM or WCP-COQAM with RC pulse with roll-off factor 0.1 under different CFO values in COST-207 Rayleigh fading channel

As can be observed from the above figures, an error floor is observed for high SNR levels owing to the interference created due to CFO. Such an error floor was not observed in AWGN or in the static ISI COST-207 channel, since SNR values that are considered was not as high as the SNR values used in the Rayleigh fading simulations. The reason for the use of high SNRs in Rayleigh fading channel is to observe SER values down to 10^{-4}. Such high SNR values are needed because of the severe performance loss owing to Rayleigh fading. An important observation may be that the diversity order observed when CFO=0 is about 1. This is expected since no diversity is gained via any method such as coding, frequency hopping or maximal ratio combining, etc.

The most important observation is that OFDM has better performance in any configuration that is examined under CFO. Therefore, it has been observed that the SER vs. SNR performance of OFDM under CFO cannot be surpassed by GFDM or WCP-COQAM with the pulse shapes that is used (RC,RRC pulses with roll-off 0.1 or 0.3 or Dirichlet pulse) or in the considered channels (AWGN, Static ISI or Rayleigh fading COST-207 channels). Therefore, by resorting to more advanced pulse shaping methods, which will be detailed in Chapter 4, the effort in the following chapter is to have better SER vs. SNR performance under CFO for GFDM and WCP-COQAM than OFDM.

CHAPTER 4

PULSE SHAPING IN FBMC

4.1 Ambiguity Function and Orthogonality Conditions

In this section, we will concentrate more on the orthogonality between time symbols and subcarriers in a transmitted signal with FBMC. A general representation of an FBMC signal with K subcarriers can be given as follows.

$$x(t) = \sum_{k=0}^{K} x_k(t) \tag{4.1}$$

where

$$x_k(t) = \sum_{m} d_{k,m} p(t - mT) g_k(t) \tag{4.2}$$

and

$$g_k(t) = e^{-j2\pi t f_k}. \tag{4.3}$$

In (4.2), $p(t)$ corresponds to the pulse shaping filter's impulse response and $d_{k,m}$ corresponds to the data symbol transmitted at the k^{th} subcarrier and the m^{th} time interval. The complex exponential $g_k(t)$ serves to shift the subcarriers to their corresponding frequency positions and $f_k's$ are the center frequencies of the subcarriers. T is the symbol duration. Let also $p_k(t)$ be defined as

$$p_k(t) = p(t) g_k(t). \tag{4.4}$$

At the receiver side, if it is desired that no ICI or ISI exists between the time symbols and subcarriers, the condition in (4.5) should hold.

$$\langle p_l(t-nT), p_k(t-mT)\rangle = \delta_{lk}\delta_{nm} \tag{4.5}$$

where

$$\langle p_l(t-nT), p_k(t-mT)\rangle = \int_{-\infty}^{\infty} p_l(t-nT)p_k^*(t-mT)dt. \tag{4.6}$$

In (4.5), δ_{lk} is the Kronecker delta function which can be expressed as

$$\delta_{lk} = \begin{cases} 1, & \text{if } l = k \\ 0, & \text{otherwise.} \end{cases} \tag{4.7}$$

Considering (4.5), (4.6) and (4.7) it can be stated that if (4.5) is satisfied the pulse shape that is used will create zero ISI and ICI at the receiver. This holds when the receiver is of a matched filter type since the inner product operation given in (4.6) will resemble an MF filtering operation. In fact, throughout this chapter, all orthogonality conditions are defined for the MF receiver type. Here, the orthogonality constraint in (4.5) will be related to a commonly used function called the ambiguity function.

4.1.1 Ambiguity Function

The ambiguity function of a pulse shaping function $p(t)$ can be defined as [32]

$$\Psi_p(\tau, v) = \int_{-\infty}^{\infty} p(t)p^*(t-\tau)e^{-j2\pi vt}dt \tag{4.8}$$

where τ corresponds to the time-delay between the correlated functions and v is the frequency shift. Recalling (4.6), and replacing $f_k = kF$ in (4.3) and (4.4), the inner product in (4.6) can be expressed as

$$\langle p_l(t-nt), p_k(t-mT)\rangle = \int_{-\infty}^{\infty} p(t-nT)e^{-j2\pi lFt}p^*(t-mT)e^{j2\pi kFt}dt. \tag{4.9}$$

Comparing (4.8) and (4.9), it can be seen that

$$\langle p_l(t-nt), p_k(t-mT)\rangle = \Psi_p\left((m-n)T, (l-k)F\right). \tag{4.10}$$

Since the ambiguity function and the inner product expressed in (4.9) are related as in (4.10), the orthogonality constraint given in (4.5) is equivalent to

$$\Psi_p\left((m-n)T,(l-k)F\right) = \begin{cases} 1, & \text{if } m=n, l=k \\ 0, & \text{otherwise} \end{cases} \tag{4.11}$$

which can also be expressed as

$$\Psi_p(mT,kF) = \begin{cases} 1, & \text{if } m=k=0 \\ 0, & \text{otherwise.} \end{cases} \tag{4.12}$$

Note that when k=0,

$$\Psi_p(\tau,0) = \int_{-\infty}^{\infty} p(t)p^*(t-\tau)dt, \tag{4.13}$$

which corresponds to the case for which the symbols are transmitted on the same subcarrier. In this case, the symbols can only be differentiated with their transmission time delays. This time delay is represented as τ in (4.13). When the correlator outputs are sampled at a sampling period of T in an MF receiver, $\tau = nT$. This means that the orthogonality constraint given in (4.13) corresponds to the Nyquist criterion for zero ISI. Therefore, one of the possible pulse shape designs is the square-root-raised cosine (RRC) pulse. It satisfies the Nyquist constraint for zero ISI [33]. However, it has some disadvantages. First, denoting the spacing between the subcarriers as F, if $F = \frac{1}{T}$, where T is the sampling duration, any RRC pulse with roll-off factor greater than zero will violate the orthogonality constraint in (4.12) due to the created ICI between the subcarriers. Furthermore, any increase in the roll-off factor will result in a higher ICI, which is not desired. To preserve orthogonality, a possible approach can be increasing the subcarrier spacing proportional to the roll-off factor as in the following equation.

$$F = \frac{1+\alpha}{T}. \tag{4.14}$$

In this case, lattice symbol density, which is defined as the number of symbols per unit area, η, can be calculated as

$$\eta = \frac{1}{TF} = \frac{1}{1+\alpha} \leqslant 1. \tag{4.15}$$

Considering (4.15), increasing roll-off factor decreases the lattice symbol density, which reduces the overall spectral efficiency. Instead of using RRC pulses with high roll-off factors, using RRC pulses with low roll-off factors also have some disadvantages [5]. These are

- A small roll-off factor results in a slowly decaying time-domain pulse. This causes high complexity for the receive and transmit filters, which will have long impulse responses.
- If there is any timing offset at the sampler at the receiver side, this will cause high ISI. Therefore, the communication system will have high sensitivity to timing offset at the receiver.
- Since the pulse have long duration, in terms of ISI, it will be more sensitive to time variation in the channel. This results from the fact that if the channel changes much from symbol to symbol, the pulses corresponding to different symbols will be multiplied by a different channel factor, which in turn creates ISI.

Therefore, taking into account the abovementioned disadvantages of having either small or large roll-off factor for the RRC pulses, the pulse design is carried out with some more advanced methods.

4.1.2 Advanced Pulse Shape Design Methods

The disadvantages of RRC pulses that are discussed in the previous section leads a pulse shape designer to opt for more advanced pulse shaping methods. It is important to note that the purpose is to find pulses that has immunity to ISI, which is caused by the multipath effect in the transmission channel that causes time dispersion or by any timing offset at the sampler at the receiver. Moreover, the designed pulses should also have immunity to ICI, which is created by the Doppler effects in the channel [34], which corresponds the frequency dispersion of the channel or by the lack of frequency synchronization between the transmitter and receiver (due to any

CFO at the receiver). To combat ISI and ICI, it is crucial to use pulse shapes that has good time and frequency localization (TFL) [35]. In order to explain TFL, it will be useful to define some quantities related to the designed pulse shaping function. Firstly, the time dispersion of a pulse, $p(t)$, can be defined as

$$\gamma_t = \sqrt{\int_{-\infty}^{\infty} t^2 |p(t)|^2 dt}. \tag{4.16}$$

Furthermore, the frequency dispersion of a pulse can be given as

$$\gamma_f = \sqrt{\int_{-\infty}^{\infty} f^2 |P(f)|^2 df} \tag{4.17}$$

where $P(f) = \mathcal{F}\{p(t)\}$. In order to have pulses that have minimum TFL, we should minimize $\gamma_t \gamma_f$. However, the Heisenberg-Gabor Uncertainity Principle (HGUP) gives a lower bound for the TFL of the pulse [36]

$$\gamma_t \gamma_f \geqslant \frac{1}{4\pi}. \tag{4.18}$$

The above bound is a tight bound. In fact, it becomes an equality if and only if $p(t)$ is a Gaussian pulse [37]. The expression for a Gaussian pulse is

$$p_{Gaussian}(t) = \frac{\sqrt{\pi}}{\alpha} e^{-\frac{\pi^2 t}{\alpha^2}} \tag{4.19}$$

where α is related to the spread of the Gaussian pulse in time domain. Although the minimum value for the TFL is reached when $p(t)$ is a Gaussian pulse, the orthogonality conditions in (4.12) is not satisfied with a Gaussian pulse. In order to design pulse shapes satisfying both minimum TFL, or the Heisenberg-Gabor uncertainity lower bound and the orthogonality conditions, there are many different methods in the literature [38], [39], [40]. Amongst these, isotropic orthogonal transform algortihm (IOTA) is one of the most popular methods. In this algorithm, an initial pulse is selected to be a Gaussian pulse, and it is converted such that it has nulls in the ambiguity function $\psi(\tau, v)$ at every $\tau = L\tau_O$ and $v = L'v_O$, where L and L' are integers. This conversion can be expressed as

$$p_N(t) = \mathcal{F}^{-1} O_{\tau_O} \mathcal{F} O_{v_O} p_{Gaussian}(t). \tag{4.20}$$

Here O_{τ_O} and O_{v_O} are orthogonalization operators. If $y(t) = O_b x(t)$, orthogonalization operator O_b yields $y(t)$ as follows.

$$y(t) = \frac{x(t)}{\sqrt{\frac{1}{b}\sum_{n=-\infty}^{\infty} |x(t - n/b)|^2}}. \tag{4.21}$$

Starting with a Gaussian pulse, which satisfies the minimum value of TFL that can be achieved according to the HGUP, and applying such an orthogonalization operation, which is defined in (4.20) and (4.21), a pulse both satisfying minimum TFL and the orthogonality conditions in (4.12) can be obtained. The resulting pulse is expected to suffer less from ISI and ICI, compared to other pulses that do not have minimum TFL.

4.2 Orthogonality Conditions in OQAM-OFDM

In this section, the orthogonality conditions will be given in a more detailed fashion for OQAM-OFDM. Following that, these conditions will be generalized for WCP-COQAM modulation, which was stated to be an extension of GFDM.

OQAM-OFDM is a type of modulation that has some differences from OFDM. OFDM has a block structure that is composed of a cyclic prefix (CP) and an OFDM symbol. This block with CP has a special structure that enables single tap equalization on the receiver side with a simple DFT operation, as explained in detail in Chapter 2. It is also referred to as CP-OFDM in the literature. However, OFDM has a rectangular pulse shape, which has poor decaying property in frequency domain, which reportedly creates high distortion due to CFO at the receiver or frequency dispersion caused by the transmission channel [3], [4], [5] and high OOB radiation [5], [7]. Hence, pulse shaping is applied in order to improve such fallbacks of OFDM. OQAM/OFDM is one example for such modulation types with a pulse shaping flexibility. It also does not have any block structure with a CP.

The similarity between CP-OFDM and OQAM/OFDM is that there is no interference between the subcarriers (no ICI) and between the OFDM symbols (ISI), that is, the subcarriers and OFDM symbols are orthogonal when there is no frequency or time dispersion due to transmission channel or no timing and frequency synchoronization

errors between the receiver and the transmitter. The orthogonality is also satisfied in OFDM/OQAM with a pulse shape different than the rectangular pulse thanks to the OQAM type modulation. If OQAM modulation is not used, it is not possible to use a pulse with good time-frequency localization with a lattice density of 1 according to the Balian-Low theorem.

The discrete OQAM-OFDM modulated signal can be obtained from (4.1). Letting $t = nT$ in (4.1), where T is the sampling period and $x_k[n] = x_k(nT)$, and considering the phase difference between the complex and real parts of the transmitted data symbols in OQAM modulation, one can obtain the OQAM-OFDM modulated signal, namely $x_{OOM}[n]$ as

$$x_{OOM}[n] = \sum_{k=0}^{K-1} x_k[n] = \sum_{k=0}^{K-1} \left\{ \sum_{m=-\infty}^{\infty} d_{k,m}^{\Re} p[n - mK] g_k[n] + \sum_{m=-\infty}^{\infty} j d_{k,m}^{\Im} p[n + K/2 - mK] g_k[n] \right\}. \tag{4.22}$$

Here $g_k[n]$ is equal to $g_k(nT)$ in (4.3), only with a difference due to a phase term, $\beta = e^{-j\pi\frac{\alpha}{K}}$. In this case,

$$g_k[n] = \beta g_k(nT) = \beta e^{-j2\pi nTf_k} = e^{-j2\pi\frac{k}{K}(n-\alpha/2)}. \tag{4.23}$$

The significance of the phase term β will become clear in the following parts. The block diagram for the construction of the transmitted signal, $x_{OOM}[n]$, and the OQAM-OFDM MF receiver is presented in Figure 4.1 (a) and 4.1 (b), respectively. [3].

In Figure 4.1, if there is no ISI or ICI, $d_{k,m} = \tilde{d}_{k,m}$. In this case, the value of the recovered symbol at the k^{th} subcarrier and m^{th} symbol interval, should only depend on the transmitted constellation symbol at the k^{th} subcarrier and m^{th} symbol interval. The effect of the symbol transmitted at the $(k + v)^{th}$ subcarrier and m^{th} symbol interval on the received symbol at the k^{th} subcarrier and m^{th} symbol interval (This effect should be zero in order to have zero ICI) is also depicted as a block diagram as in Figure 4.2 [3]. For zero ISI and ICI, the conditions given in (4.24)-(4.27) should be satisfied [3].

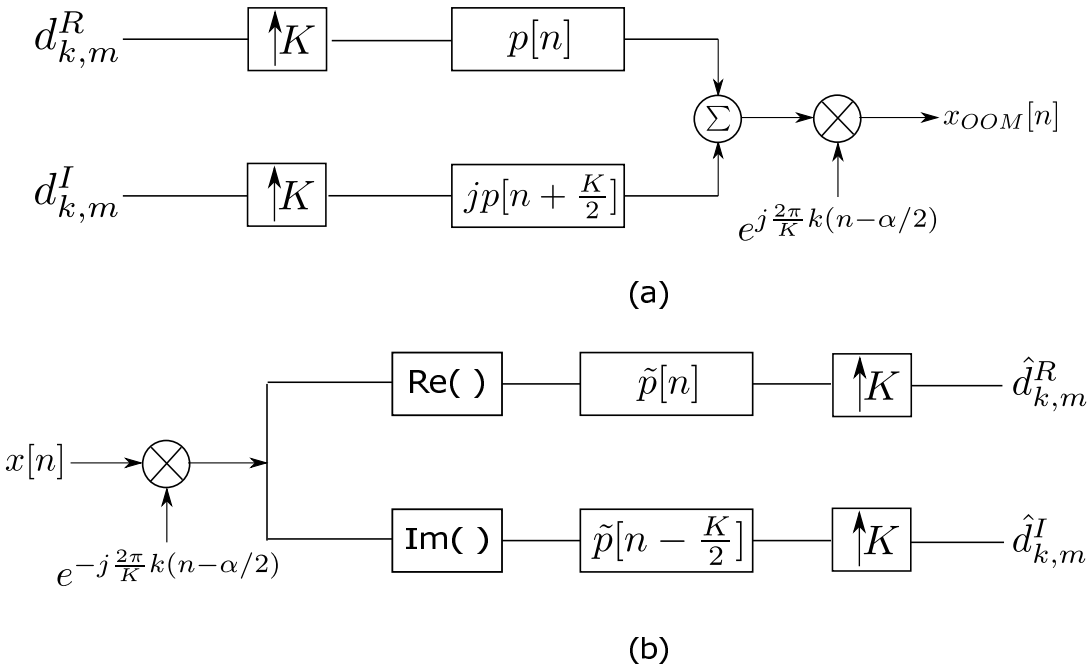

Figure 4.1: Block diagram for OQAM-OFDM transreceiver

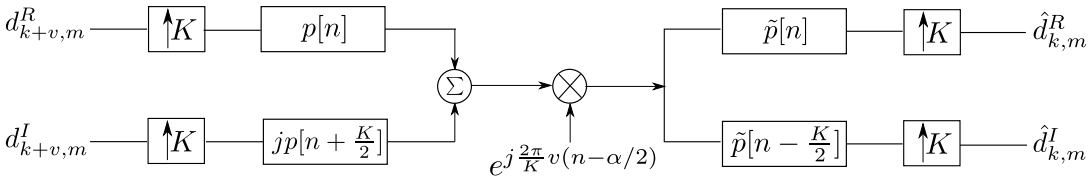

Figure 4.2: The interference path from $k+v^{th}$ subcarrier on the estimate of k^{th} subcarrier at the same time slot

$$\Re\left\{p[n-mK]e^{j2\pi\frac{v}{K}(n-\alpha/2)}\right\} * \tilde{p}[n]\big|_{n=0} = \delta[m]\delta[v], \tag{4.24}$$

$$\Im\left\{jp[n+K/2-mK]e^{j2\pi\frac{v}{K}(n-\alpha/2)}\right\} * \tilde{p}[n-K/2]\big|_{n=0} = \delta[m]\delta[v], \tag{4.25}$$

$$\Re\left\{jp[n+K/2-mK]e^{j2\pi\frac{v}{K}(n-\alpha/2)}\right\} * \tilde{p}[n]\big|_{n=0} = 0, \tag{4.26}$$

$$\Im\left\{p[n-mK]e^{j2\pi\frac{v}{K}(n-\alpha/2)}\right\} * \tilde{p}[n-K/2]\big|_{n=0} = 0. \tag{4.27}$$

The above equations (4.24)-(4.27) imply zero ICI when $v \neq 0$. In terms of ISI, (4.24) and (4.25) is satisfied only when there is no ISI for $d^{\Re}_{k,m}$ or $d^{\Im}_{k,m}$. In addition, (4.26) and (4.27) ensures that no interference exists between the real and imaginary parts of $d_{k,m}$.

In [3], it has also been proved that (4.26) and (4.27) are equivalent and they are satisfied if $p[n]$ is an even symmetric function such that

$$p[n] = p[(2b+1)\frac{K}{2} + \alpha - n] \tag{4.28}$$

where $b \in \mathbb{Z}$ and $\alpha \in [0, K-1]$. Here α and b can be adjusted according to the designed FIR filter length. If the filter length is denoted as L_p, the α parameter should be selected as $\alpha = L_p + \frac{K}{2} - 1 \bmod K$. When the filter length is an integer multiple of the number of subcarriers, K, that is $L_p = G \cdot K$, where $G \in \mathbb{Z}$, $\alpha = \frac{K}{2} - 1$. Therefore, when constructing the transmitted signal $x_{OOM}[n]$, the selection of the value of α is important to have orthogonality with the designed pulse.

Now that (4.26)-(4.27) are satisfied when the designed pulse satisfies (4.28), the remaining conditions for orthogonality, (4.24)-(4.25) should also hold. In [3], the equivalence of (4.24)-(4.25) is also shown and they have been proven to be satisfied if the following equality holds.

$$\frac{1}{2}\langle p, p_{-v,m}\rangle + \frac{1}{2}\langle p, p_{v,m}\rangle = \delta[m]\delta[v] \tag{4.29}$$

where

$$p_{v,m} = p[n-mK]e^{j2\pi\frac{R}{2}v(n-\alpha/2)}. \tag{4.30}$$

Here, $\delta[m]$ is the Kronecker delta function and $\langle c, d\rangle = \sum_{n=-\infty}^{\infty} c[n]d^*[n]$ corresponds to the inner product of the sequences $c[n]$ and $d[n]$. In [3], the condition in (4.29) is written using discrete-time Zak transform (DZT).

4.2.1 Orthogonality Expressions using DZT

DZT of a sequence $c[n]$ is defined as [41], [42],

$$\mathcal{Z}_p(n,\theta) = \sum_{m=-\infty}^{\infty} p\left[n + m\frac{K}{2}\right] e^{-j2\pi m\theta} \tag{4.31}$$

with an inverse transform given as

$$p[n] = \int_0^1 \mathcal{Z}_p(n,\theta)d\theta. \tag{4.32}$$

In [3], it has been proved that starting with an even symmetric pulse $p[n]$ satisfying (4.28), the discrete Zak transform of an orthogonal pulse $p_0[n]$ satisfying (4.28) and (4.29), thus all of the orthogonality conditions, which are (4.24)-(4.27), can be found as

$$\mathcal{Z}_{p_0}(n,\theta) = \frac{2\mathcal{Z}_p(n,\theta)}{\sqrt{K|\mathcal{Z}_p(n,\theta)|^2 + K|\mathcal{Z}_p(n,\theta-\frac{1}{2})|^2}}. \tag{4.33}$$

If $\mathcal{Z}_{p_0}$ is found, $p_0[n]$ can be obtained by taking inverse DZT. Therefore, the design procedure is simply taking the DZT of an initial pulse $p[n]$ satisfying the symmetry condition in (4.28) and finding $\mathcal{Z}_{p_0}(n,\theta)$ using (4.33) and taking the inverse DZT to obtain the orthogonal pulse $p_0[n]$. However, an even simpler implementation of this design procedure is to use FFT or IFFT to take DZTs or inverse DZTs, respectively.

4.2.2 Implementation of the Algorithm Using FFT

The DZT expression given in (4.31) can also be evaluated at discrete frequencies as [41]

$$\mathcal{Z}_p[n,v] = \sum_{m=0}^{G-1} p\left[n + m\frac{K}{2}\right] e^{-j2\pi(v/G)m} \tag{4.34}$$

where $n = 0, 1, \ldots, \dfrac{K}{2} - 1, v = 0, 1, \ldots, G-1$. Here the length of the initial filter $p[n]$ should satisfy $L_p = \dfrac{K}{2}\, G$, that is L_p should be an integer multiple of $K/2$. Therefore,$G = \dfrac{2L_p}{K}$. It can also be seen that $\mathcal{Z}_p[n,v]$ can be evaluated by taking the FFTs of the columns of the following $G \times \dfrac{K}{2}$ matrix $\mathbf{P}$

$$\mathbf{P} = \begin{bmatrix} p[0] & p[1] & \dots & p[K/2-1] \\ p[K/2] & p[K/2+1] & \dots & p[K-1] \\ p[K] & p[K+1] & \dots & p[3K/2-1] \\ \vdots & \vdots & & \vdots \\ p[L_p - K/2] & p[L_p - K/2+1] & \dots & p[L_p-1] \end{bmatrix}. \tag{4.35}$$

Using this observation, the design procedure to obtain an orthogonal pulse is as follows.

- Choose an even symmetric initial filter, $p[n]$, satisfying (4.28).
- Zero-padding can be done on $p[n]$ while (4.28) is still satisfied. After zero-padding, the length of the initial filter must be an integer multiple of the half of the number of subcarriers that will be used. That is $L_p = \dfrac{K}{2}\, G$.
- Compute DZT of the orthogonal filter $p_0[n]$ according to (4.36). $Z_p(n,v)$ can be found by taking the FFTs of the columns of the matrix $\mathbf{P}$ in (4.35).

$$\mathcal{Z}_{p_0}(n,v) = \frac{2\mathcal{Z}_p(n,v)}{\sqrt{K|\mathcal{Z}_p(n,v)|^2 + K|\mathcal{Z}_p(n,v-\frac{G}{2})|^2}} \tag{4.36}$$

- Compute the inverse DZT of $\mathcal{Z}_{p_0}[n,v]$. This corresponds to taking the inverse FFTs of the columns of the matrix $\mathcal{Z}_{p_0}[n,v]$.

Starting with an initial pulse, $p[n]$, orthogonal pulses that satisfy (4.24)-(4.27) can be created following the above-mentioned steps.

4.3 Equivalence of Orthogonalization of Pulses Using Discrete Zak Transform and Isotropic Orthogonal Transform Algorithm

Now that the two algorithms that yield orthogonal pulses, namely the Isotropic Orthogonal Transform Algorithm (IOTA) and orthogonalization using discrete time Zak Transform, are explained in detail, the relation between the two algortihms worth discussing. In fact, the equivalence of the two algorithms are proved in [43], when a Gaussian pulse is used as an initial pulse in the algorithm that employs discrete Zak

transform. Therefore, in order to form an orthogonal pulse in time and in frequency, which have minimum TFL, the application of the orthogonalization algorithm that resorts to discrete Zak transform on a Gaussian pulse will be equivalent to application of IOTA on a Gaussian pulse. Owing to the simplicity of the orthogonalization algorithm based on discrete Zak transform with simple fft and ifft operations, we have employed this algorithm instead of IOTA to obtain orthogonal pulses to be used with WCP-COQAM. However, for the discrete case, there is no proof that the abovementioned algorithm will yield the same orthogonal pulse as IOTA will give. Therefore, starting with an initial Gaussian function, after the application of discrete Zak Transform, the resulting pulse that are used in the simulations in this chapter is checked whether it satisfies the criteria given in [3] to have minimum time frequency localization. Furthermore, the pulses obtained after the discrete Zak Transform based algorithm will be referred to as DZAK pulse.

4.4 Orthogonality Conditions for WCP-COQAM

In this section, the orthogonality conditions for WCP-COQAM for MF receiver will be analyzed. To begin with, consider the transmitted signal with WCP-COQAM,

$$x_{WCP-COQAM}[n] = \sum_{k=0}^{K-1} \left\{ \sum_{m=0}^{M-1} d_{k,m}^{\Re} g_k[n] p[(n-mK)_N] + \sum_{m=0}^{M-1} j d_{k,m}^{\Im} g_k[n] p[(n+K/2-mK)_N] \right\}. \tag{4.37}$$

Considering the MF receiver which corresponds to taking the real part of the multiplication of the received and equalized vector y_{eq} by A^H, the zero ISI and ICI conditions for WCP-COQAM can be written as follows.

$$\sum_{n=0}^{N-1} \Re\left\{ p[(n-mK)_N] e^{j2\pi \frac{v}{K}(n-\alpha/2)} p^*[n] \right\} = \delta[(m)_M]\delta[v], \tag{4.38}$$

$$\sum_{n=0}^{N-1} \Re\left\{ p[(n+K/2-mK)_N] e^{j2\pi \frac{v}{K}(n-\alpha/2)} p^*[(n+K/2)_N] \right\} = \delta[(m)_M]\delta[v], \tag{4.39}$$

$$\sum_{n=0}^{N-1} \Re\left\{jp[(n+K/2-mK)_N]e^{j2\pi\frac{v}{K}(n-\alpha/2)}p^*[n]\right\} = 0, \tag{4.40}$$

$$\sum_{n=0}^{N-1} \Re\left\{p[(n-mK)_N]e^{j2\pi\frac{v}{K}(n-\alpha/2)}jp^*[(n+K/2)_N]\right\} = 0. \tag{4.41}$$

In (4.38)-(4.41), $N = M \cdot K$, where K is the number of subcarriers and M is the number of WCP-COQAM symbols in a WCP-COQAM frame. Note also that by definition $\delta[(m)_M]$ is equal to 1 when m is equal to integer multiples of M and it is equal to zero otherwise. If (4.38)-(4.41) are satisfied when $v \neq 0$, there will be no ICI between the $(k+v)^{th}$ subcarrier and the k^{th} subcarrier. Therefore, the above equations implies zero ICI when $v \neq 0$. On the other hand, when $v = 0$, (4.38)-(4.39) ensures no ISI for $d_{k,m}^{\Re}$ or $d_{k,m}^{\Im}$, that is there is no ISI between real or imaginary parts of the symbols that are transmitted at the same subcarrier, but at different WCP-COQAM symbols. Moreover, when $v = 0$, (4.40)-(4.41) guarantee that there is no interference between the real and imaginary parts of $d_{k,l}$ transmitted either at the same WCP-COQAM symbol or at different WCP-COQAM symbols.

4.4.1 Relation Between the Orthogonality Conditions of OQAM/OFDM and WCP-COQAM

In this section, it will be shown that the orthogonality conditions which are found for OQAM-OFDM in (4.24)-(4.27) imply the conditions for orthogonality in WCP-COQAM, given in (4.38)-(4.41). Therefore, if there is such an implication, the orthogonal pulses that are designed for OQAM-OFDM by using the discrete Zak transform based algorithm, can also be used for WCP-COQAM as orthogonal pulses.

Theorem: If a pulse shape $p[n]$ satisfies the orthogonality conditions defined for OQAM-OFDM, which are (4.24)-(4.27), it will also satisfy the orthogonality conditions for WCP-COQAM, given in (4.38)-(4.41).

Proof: Define $s_{\beta,\gamma}[m,v]$ such that

$$s_{\beta,\gamma}[m,v] = \sum_{n=0}^{N-1} p[(n-mK+\beta)_N]g_v[n]p^*[(n+\gamma)_N] \tag{4.42}$$

where $g_v[n] = e^{j2\pi\frac{v}{K}(n-\alpha/2)}$. Assume that $m \in \{1, 2, \cdots, M\}$. Moreover, also assume that β is either equal to zero or $K/2$. Towards the end of the proof, the reason for such assumptions will be clear. With these assumptions, $-MK \leqslant \beta - mK \leqslant 0$. In this case, the term $p[(n - mK + \beta)_N]$ in (4.42) can also be expressed as follows.

$$p[(n - mK + \beta)_N] = \begin{cases} p[n + (M - m)K + \beta], & \text{when } 0 \leqslant n \leqslant mK - \beta - 1 \\ p[n - mK + \beta], & \text{when } mK - \beta \leqslant n \leqslant MK - 1 \end{cases} \tag{4.43}$$

where M is the number of WCP-COQAM symbols in a WCP-COQAM frame and K is the number of subcarriers. Note also that $N = MK$. Moreover, also assume that γ is equal to zero or $K/2$. This will bring about $p[(n + \gamma)_N]$ being expressed as follows.

$$p[(n + \gamma)_N] = \begin{cases} p[n + \gamma], & \text{when } 0 \leqslant n \leqslant MK - \gamma - 1 \\ p[n - MK + \gamma], & \text{when } MK - \gamma \leqslant n \leqslant MK - 1. \end{cases} \tag{4.44}$$

Using (4.43) and (4.44), and also assuming $MK - \gamma - 1 \geqslant mK - \beta - 1$, (4.42) can be rewritten as

$$\begin{aligned} s_{\beta,\gamma}[m, v] = &\sum_{n=0}^{mK-\beta-1} p[n + (M - m)K + \beta] g_v[n] p^*[n + \gamma] \\ &+ \sum_{n=mK-\beta}^{MK-\gamma-1} p[n - mK + \beta] g_v[n] p^*[n + \gamma] \\ &+ \sum_{n=MK-\gamma}^{MK-1} p[n - mK + \beta] g_v[n] p^*[n - MK + \gamma]. \end{aligned} \tag{4.45}$$

Changing the summation limits for the third summation term in (4.45), one can get

$$\begin{aligned} s_{\beta,\gamma}[m, v] = &\sum_{n=0}^{mK-\beta-1} p[n + (M - m)K + \beta] g_v[n] p^*[n + \gamma] \\ &+ \sum_{n=mK-\beta}^{MK-\gamma-1} p[n - mK + \beta] g_v[n] p^*[n + \gamma] \\ &+ \sum_{n=-\gamma}^{-1} p[n + (M - m)K + \beta] g_v[n] p^*[n + \gamma]. \end{aligned} \tag{4.46}$$

since $g_v[n] = g_v[n + MK]$. Note that in (4.46), the first and the third summation terms can be combined to obtain

$$s_{\beta,\gamma}[m,v] = \sum_{n=-\gamma}^{mK-\beta-1} p[n+(M-m)K+\beta]g_v[n]p^*[n+\gamma] + \sum_{n=mK-\beta}^{MK-\gamma-1} p[n-mK+\beta]g_v[n]p^*[n+\gamma]. \tag{4.47}$$

Moreover, the two summation terms in (4.47) can also be written as follows.

$$\begin{aligned}\sum_{n=-\gamma}^{mK-\beta-1} p[n+(M-m)K+\beta]g_v[n]p^*[n+\gamma] &= p[n+(M-m)K+\beta]g_v[n] \ast \tilde{p}[n-\gamma]\Big|_{n=0} \\ \sum_{n=mK-\beta}^{MK-\gamma-1} p[n-mK+\beta]g_v[n]p^*[n+\gamma] &= p[n-mK+\beta]g_v[n] \ast \tilde{p}[n-\gamma]\Big|_{n=0}\end{aligned} \tag{4.48}$$

where $\ast$ is the convolution operator and $\tilde{p}[n] = p^*[-n]$. Using (4.47) and (4.48), (4.42) can also be written as

$$s_{\beta,\gamma}[m,v] = p[n+(M-m)K+\beta]g_v[n] \ast \tilde{p}[n-\gamma]\Big|_{n=0} + p[n-mK+\beta]g_v[n] \ast \tilde{p}[n-\gamma]\Big|_{n=0}. \tag{4.49}$$

Moreover, considering (4.42) orthogonality conditions for WCP-COQAM, which are (4.38)-(4.41), can be written in terms of $s_{\beta,\gamma}[m,v]$ as follows.

$$\Re\left\{s_{\beta=0,\gamma=0}[m,v]\right\} = \delta[(m)_M]\delta[v], \tag{4.50}$$

$$\Im\left\{j s_{\beta=K/2,\gamma=K/2}[m,v]\right\} = \delta[(m)_M]\delta[v], \tag{4.51}$$

$$\Re\left\{j s_{\beta=K/2,\gamma=0}[m,v]\right\} = 0, \tag{4.52}$$

$$\Im\left\{s_{\beta=0,\gamma=K/2}[m,v]\right\} = 0. \tag{4.53}$$

Replacing $s_{\beta,\gamma}$ in (4.50)-(4.53) using (4.49), and since $g_v[n] = e^{j2\pi\frac{v}{K}(n-\alpha/2)}$, one can get

$$\Re\{p[n+(M-m)K]e^{j2\pi\frac{v}{K}(n-\alpha/2)} \ast \tilde{p}[n]\Big|_{n=0}\} + \Re\{p[n-mK]e^{j2\pi\frac{v}{K}(n-\alpha/2)} \ast \tilde{p}[n]\Big|_{n=0}\} = \delta[(m)_M]\delta[v], \tag{4.54}$$

$$\Im\{jp[n+(M-m)K+K/2]e^{j2\pi\frac{v}{K}(n-\alpha/2)} \circledast \tilde{p}[n-K/2]\Big|_{n=0}\} + \Im\{jp[n-mK+K/2]e^{j2\pi\frac{v}{K}(n-\alpha/2)} \circledast \tilde{p}[n-K/2]\Big|_{n=0}\} = \delta[(m)_M]\delta[v], \tag{4.55}$$

$$\Re\{jp[n+(M-m)K+K/2]e^{j2\pi\frac{v}{K}(n-\alpha/2)} \circledast \tilde{p}[n]\Big|_{n=0}\} + \Re\{jp[n-mK+K/2]e^{j2\pi\frac{v}{K}(n-\alpha/2)} \circledast \tilde{p}[n]\Big|_{n=0}\} = 0, \tag{4.56}$$

$$\Im\{p[n+(M-m)K]e^{j2\pi\frac{v}{K}(n-\alpha/2)} \circledast \tilde{p}[n-K/2]\Big|_{n=0}\} + \Im\{p[n-mK]e^{j2\pi\frac{v}{K}(n-\alpha/2)} \circledast \tilde{p}[n-K/2]\Big|_{n=0}\} = 0. \tag{4.57}$$

Consider the case $m \in \{1, 2, \cdots, M-1, M\}$. For these values of m, the assumed conditions $MK - \gamma - 1 \geqslant mK - \beta - 1$ and $-MK \leqslant \beta - mK \leqslant 0$ in the proof hold when $\beta = \gamma = 0$ or $\beta = \gamma = K/2$ or $(\beta, \gamma) = (K/2, 0)$, which corresponds to the cases in (4.50), (4.51) and (4.52). Therefore, it is valid that (4.50), (4.51), (4.52) are equivalent to (4.54), (4.55), (4.56), respectively. For these values of m, (4.24) implies (4.54) when $p[n]$ is real valued. Similarly, for the same m values, when $p[n]$ is real valued, (4.55) and (4.56) are also satisfied by (4.25) and (4.26), respectively. Note also that, if the orthogonality conditions in (4.50)-(4.52) hold for $m = 1, 2, \cdots, M-1, M$, they will also hold for any possible value of m, since $s_{\beta,\gamma}[m, v] = s_{\beta,\gamma}[m + PM, v]$ for any integer P value.

The remaining case in the proof is the satisfaction of (4.53). In (4.53), note that $\beta = 0, \gamma = K/2$. For these values, choose another set for the possible values of m as $\{0, 1, 2, \cdots, M-1\}$. For these values of m, β, γ, the assumed conditions in the proof $MK - \gamma - 1 \geqslant mK - \beta - 1$ and $-MK \leqslant \beta - mK \leqslant 0$ holds. Therefore, (4.53) is equivalent to (4.57). Since (4.57) is also satisfied by (4.27) when $p[n]$ is real, the proof is ended.

4.5 Simulation Results

In this section, simulation results will be given when discrete Zak transform based algorithm is applied to an initial Gaussian pulse and the resulting orthogonal pulse is

used for WCP-COQAM. In this section, the orthogonalized Gaussian pulse is simply referred to as the Gaussian pulse. Simulation parameters are the same as that in Section 3.8, which are given in Table 3.1, except that the pulse shape that is used is an orthogonalized Gaussian pulse for WCP-COQAM, instead of the commonly used pulse shapes such as RC or RRC pulses. For the Gaussian pulse, the parameter α, given in (4.19), which determines the dispersion of the Gaussian pulse in time domain, is selected as either 0.1 or 0.3. Error rate performances of OFDM and WCP-COQAM will be compared under CFO. The channel types that are used are AWGN, static ISI Cost-207, and Rayleigh fading COST-207, as in Section 3.8.

4.5.1 Simulation Results in AWGN

In AWGN, SER curves of OFDM and WCP-COQAM with Gaussian pulse under CFO are given in Figure 4.3 and Figure 4.4, for the α parameter of the Gaussian pulse being equal to 0.1 and 0.3, respectively.

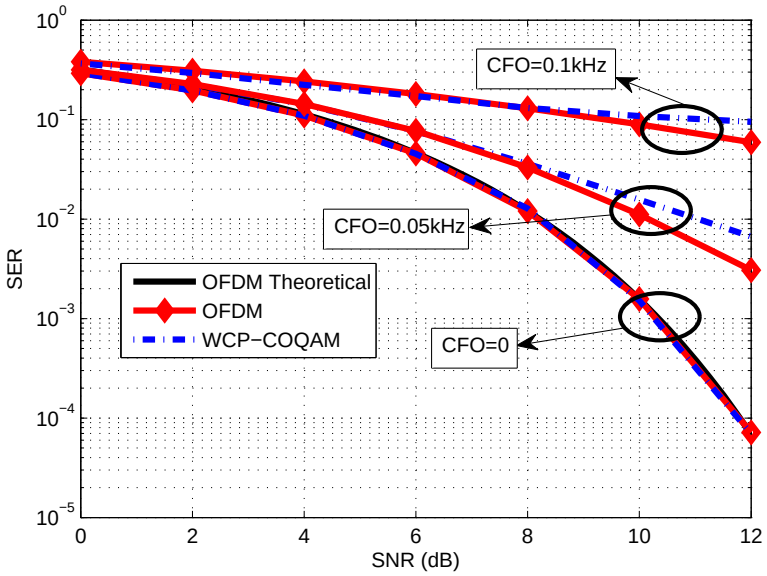

Figure 4.3: SER v.s SNR for OFDM and WCP-COQAM with the Gaussian pulse (with $\alpha = 0.1$) under different CFO values in AWGN

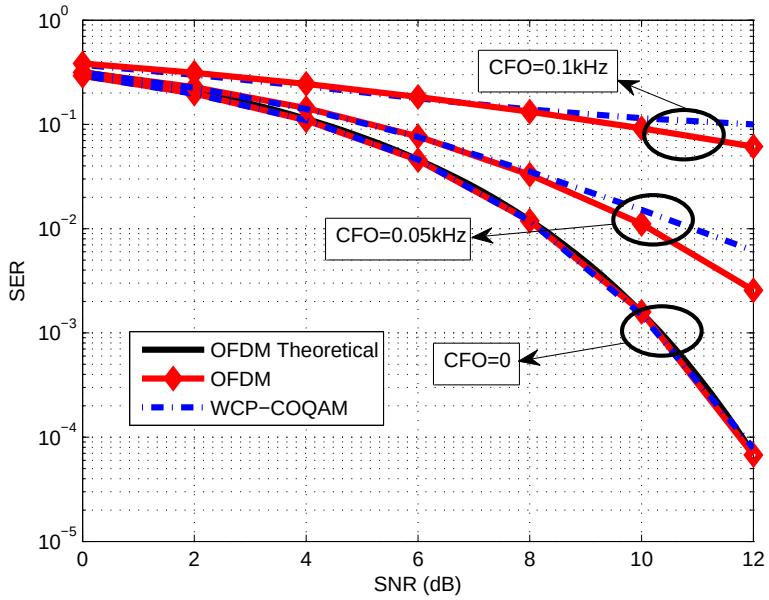

Figure 4.4: SER vs. SNR for OFDM and WCP-COQAM with the Gaussian pulse (with $\alpha = 0.3$) under different CFO values in AWGN

As can be seen in Figures 4.3 and 4.4, the theoretical OFDM curve is plotted according to (3.12). Note from the figures that, WCP-COQAM performs the same as OFDM when there is no CFO. This is owing to the fact that the Gaussian pulse is orthogonalized in time and frequency to yield zero ISI and ICI as OFDM when there is no CFO. However, for non-zero CFO, WCP-COQAM do not perform any better than OFDM for any CFO value and for any of the simulated α values, which are 0.1 and 0.3 for the Gaussian pulse, in AWGN. Therefore, in search for a case for which WCP-COQAM performs better than OFDM, the simulations continue under COST-207 Static ISI channel.

4.5.2 Simulation Results under Static ISI COST-207 Channel

Similar simulations performed under AWGN are also conducted under static ISI Hilly Terrain COST-207 channel. The simulation parameters are the same as that used for AWGN channel. Note that the effect of non-ideal channel estimation is not reflected to the simulation results, that is, the channel is perfectly known at the receiver and equalization is performed as a single tap-equalization at the receiver side, which is

the very simple equalization method for both OFDM and WCP-COQAM. The SER curves for OFDM and WCP-COQAM under static ISI COST-207 channel for different CFO values are given in Figures 4.5 and 4.6. Figure 4.5 is for the Gaussian pulse with $\alpha = 0.1$ and Figure 4.6 uses the Gaussian pulse with $\alpha = 0.3$.

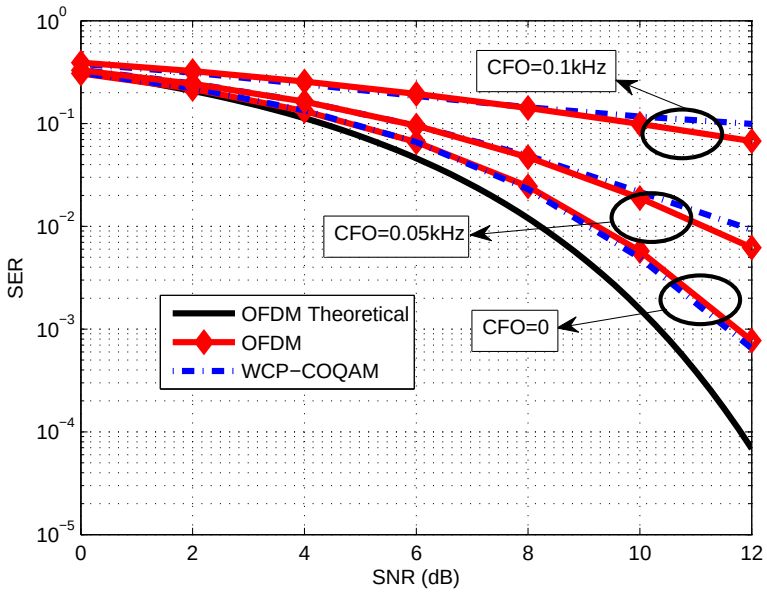

Figure 4.5: SER vs. SNR for OFDM and WCP-COQAM with the Gaussian pulse (with $\alpha = 0.1$) under different CFO values in Static ISI COST-207 Channel

As can be observed from Figures 4.5 and 4.6, despite OFDM and WCP-COQAM shows similar performance when there is no CFO, for non-zero CFO, OFDM performs better than WCP-COQAM, which points out a better CFO immunity for OFDM also for Static ISI COST-207 channel.

4.5.3 Simulation Results under Rayleigh Fading COST-207 Channel

In this section, the error rate performances of OFDM and WCP-COQAM will be compared when Rayleigh fading is present in the Hilly Terrain COST-207 channel. Figures 4.7 and 4.8 show the SER curves for OFDM and WCP-COQAM with Gaussian pulse with $\alpha = 0.1$ and $\alpha = 0.3$, respectively.

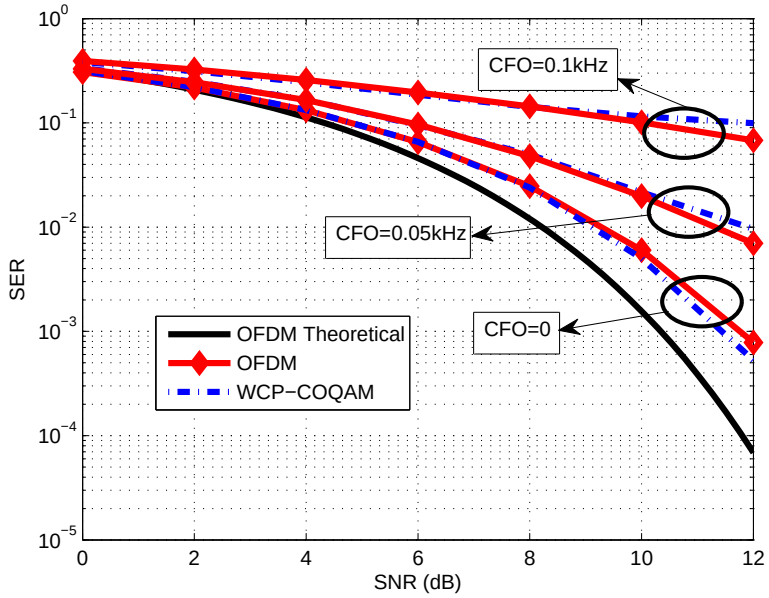

Figure 4.6: SER vs. SNR for OFDM and WCP-COQAM with the Gaussian pulse (with $\alpha = 0.3$) under different CFO values in Static ISI COST-207 Channel

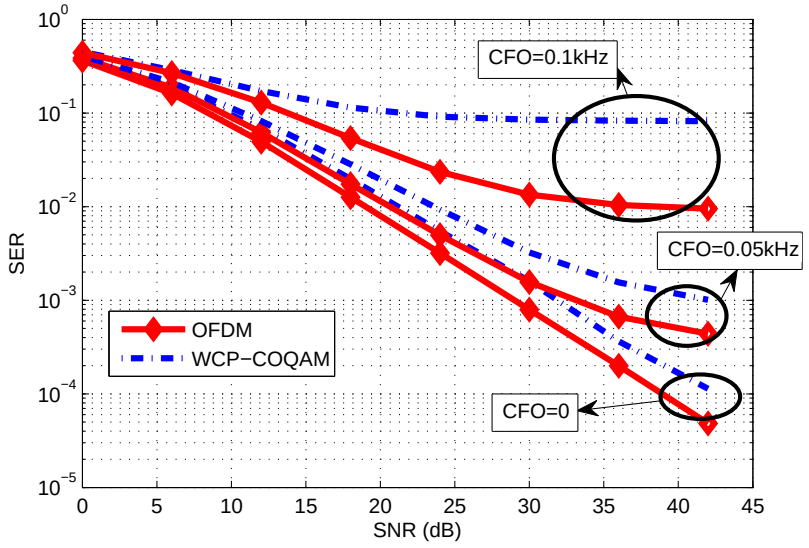

Figure 4.7: SER vs. SNR for OFDM and WCP-COQAM with the Gaussian pulse (with $\alpha = 0.1$) under different CFO values in Rayleigh fading COST-207 channel

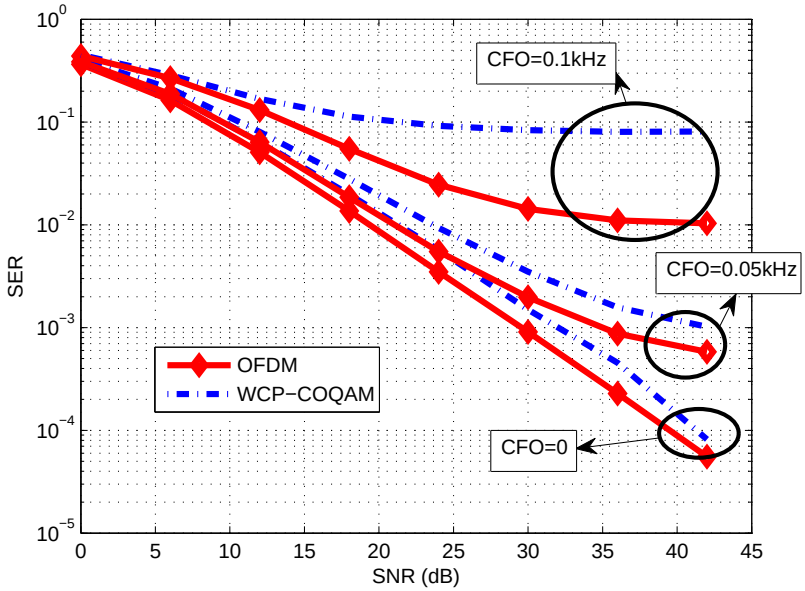

Figure 4.8: SER vs. SNR for OFDM and WCP-COQAM with the Gaussian pulse (with $\alpha = 0.3$) under different CFO values in Rayleigh fading COST-207 channel

As can be seen from Figures 4.7 and 4.8, for non-zero CFO, an error floor is observed at high SNR levels. This is owing to the interference created by CFO. Such an error floor was not observed in the simulations performed under AWGN or COST-207 static ISI channel since such high SNR values are not simulated for these channels. The reason for experimenting on SNR values as high as 40dB under Rayleigh fading COST-207 channel is to be able to observe SER values down to 10^{-4}, since Rayleigh fading causes a significant error rate performance loss.

A similar observation under Rayleigh fading COST-207 channel is that OFDM performs better than WCP-COQAM with the Gaussian pulse with $\alpha = 0.1$ or $\alpha = 0.3$ for any CFO value. In fact, for the highest CFO value in the simulations, the performance loss for WCP-COQAM is very severe compared to OFDM. Therefore, considering all of the simulations that are presented, using discrete Zak transform based methods to obtain minimum time frequency localization pulses in WCP-COQAM exploiting its pulse-shaping flexibility to obtain a better CFO immunity than OFDM seems to be ineffective for the observed cases in this chapter.

CHAPTER 5

OUT-OF-BAND RADIATION COMPARISONS

5.1 Various Aspects of Out-of-Band (OOB) Emission Levels

Cognitive radio (CR) based applications [44], [45] have been gaining importance and they are considered to be used in future communication standards in 5G and after. CR is composed of three main components: spectrum sensing, dynamic spectrum access, adaptive transmission. Spectrum sensing refers to the communication phase in which the users listen to the channel in order to find any unused frequency gaps that they may utilize. Dynamic spectrum management phase takes place after spectrum sensing. In this phase, selection amongst the detected spectrum gaps is planned. Adaptive transmission in the context of CR refers to the adaptation of the communication parameters (such as communication bandwidth, transmission power etc.) according to the changing state of the spectrum that is considered.

CR is important since static allocation of the time and frequency resources corresponds to very low levels of utilization. The recent study by Federal Communications Commission (FCC) has stated that the utilization of the allocated spectrum is only 30% in US. Moreover, spectrum occupancy varies from milliseconds to hours [46]. Therefore, proper use of the frequency and time resources with CR based techniques increases the spectral efficiencies drastically. This will be important for the satisfaction of the expected requirements of the 5G systems to provide 1000 times more bit rate [47].

Although CR based techniques are considered for the next generation mobile systems, they have already appeared in the currently available standards. IEEE 802.22 [48] is

the first global wireless communication standard that incorporates CR based applications. Moreover, IEEE 802.16 e/h/m gives possible cognitive radio applications which are compatible with the existing 4G systems [49].

To be able to employ CR based techniques, the users should not radiate much power out of the frequency bandwidth allocated to them. That is, their out-of-band (OOB) radiation should be small enough, in order not to interfere much with the possible users whose neighboring frequency bands can be used opportunistically. The out-of-band radiation of a transmitter, if denoted by OOB, can be calculated as,

$$OOB = P_{total} - \int_{f_c - W/2}^{f_c + W/2} X(f) df \tag{5.1}$$

where P_{total} is the total transmitted power of the user, f_c is the carrier frequency, W is the transmission bandwidth and $X(f)$ is power spectral density of the transmitted signal.

Reduced OOB emission has many advantages. First, if OOB radiation of a specific user is low, it will concentrate most of its transmitted power in its transmission BW, which will result in high SNR at the receiver side, which increases the capacity of the transmission channel. However, if there is a power leakage to outside the transmission BW, owing to the fact that intermediate frequency (IF) filter will only pass the transmission BW, there will be an SNR loss at the receiver, which will result in a capacity loss. Furthermore, for high valued OOB emissions, there will also be an increased distortion at the receiver side apart from the effect of lower SNR values, since IF filter will suppress the signal components out of the transmission BW.

The more pronounced advantage of low OOB radiation is that the interference between the neighboring users in the frequency spectrum is decreased. Since the frequency spectrum is allocated to different users, these users should not interfere much with the neighbouring ones, which is only possible with controlled amount of OOB emissions.

All in all, considering the aforementioned advantages of CR based techniques, whose application may strongly depend on limited values of OOB radiation, and direct advantages of controlled levels of OOB emissions, it is desirable to limit the OOB radiation levels of the transmitter in a single or multi-user communication scenario. In

Table 5.1: Spectrum emission limits specified in the LTE standard [51]

Spectrum emission limit (dBm)/Channel bandwidth							
Δf_{OOB} (MHz)	1.4 MHz	3.0 MHz	5 MHz	10 MHz	15 MHz	20 MHz	Measurement bandwidth
$\pm$0-1	-10	-13	-15	-18	-20	-21	30 KHz
$\pm$1-2.5	-10	-10	-10	-10	-10	-10	1 MHz
$\pm$2.5-2.8	-25	-10	-10	-10	-10	-10	1 MHz
$\pm$2.8-5		-10	-10	-10	-10	-10	1 MHz
$\pm$5-6		-25	-13	-13	-13	-13	1 MHz
$\pm$6-10			-25	-13	-13	-13	1 MHz
$\pm$10-15				-25	-13	-13	1 MHz
$\pm$15-20					-25	-13	1 MHz
$\pm$20-25						-25	1 MHz

order to limit the OOB radiations, there are many standards that draw the boundaries on the maximum allowable OOB radiation levels by defining spectral mask requirements. These are given in detail in Section 5.2.

5.2 Spectral Mask to Limit OOB Emissions

Many standards have defined spectral masks that enforce maximum allowable OOB radiation levels around the transmission bandwidths that can be utilized [50], [51]. For example, the spectral mask requirement in LTE standard is presented in Table 5.1. In Table 5.1, Δf_{OOB} indicates the distance from both ends of the transmission bandwidth. For example, if the baseband equivalent a signal of 10 MHz bandwidth is considered, that is the frequency spectrum of the signal lies between ± 5 MHz, $\Delta f_{OOB} = \pm 0 - 1$ corresponds to the frequency region between -6 and -5 MHz or 5 and 6 MHz. A better illustration to indicate what Δf_{OOB} corresponds to is indicated in Figure 5.1. As shown in Figure 5.1, the channel bandwidth corresponds to the bandwidth that is used for data transmission. Its values range from 1.4 MHz up to 20MHz in LTE. Furthermore, there is also a column entitled "Measurement

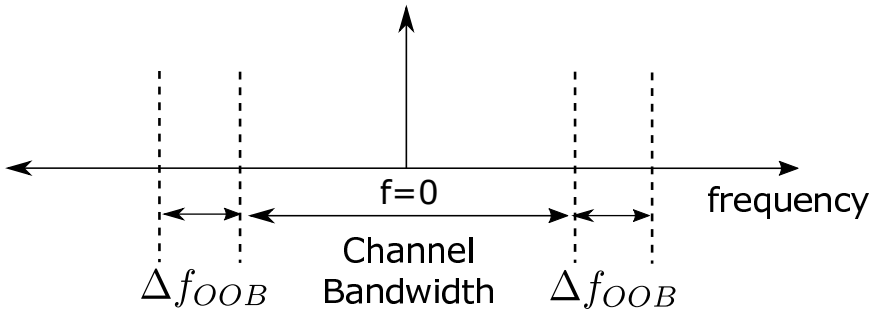

Figure 5.1: Channel bandwidth and Δf_{OOB} parameters in Table 5.1.

Bandwidth" in Table 5.1. This implies that the values given in Table 5.1 in dBm or equivalently in mW, are the average power values that is measured over a bandwidth of 1MHz.

The spectral mask specified in Table 5.1 is important in that, in the simulations that will compare OFDM, GFDM and WCP-COQAM, the transmitted power values will be compared while the transmitted signals satisfy the spectral mask requirements. Through such a comparison, the modulation type that has the highest transmission power while satisfying the spectral mask requirements will be considered to be advantageous over the others, since transmitting higher power, without creating much OOB radiation will result in higher SNR values at the receiver side, which is better in terms of the capacity of the communication system. Moreover, it can also be important to consider the effects that create additional out-of-band radiation and distortion in the transmitted signal of DACs that has sharp transitions at their time-domain output signals or power amplifier (PA) non-linearities. Furthermore, under such non-ideal effects, other than the rise in the OOB radiation levels, there are also other issues created by these non-ideal elements which shows as distortion in the transmitted signals quantified by some parameters such as error-vector magnitude (EVM), signal-to-interference ratio (SIR). Therefore, in order to carry out a thorough comparison between any type of modulation in terms of their OOB radiation, the non-ideal elements that create additional OOB emissions such as DAC or PA should also be considered along with the other effects of these non-ideal items that create distortion in the transmitted signal. These non-ideal elements and the reasons why they increase OOB emissions are detailed in Section 5.3.

5.3 Non-Ideal Effects that Increase OOB Emisssions

5.3.1 Amplifier Nonlinearity

Amplifier non-linearity is one non-ideal factor that the power amplifiers (PAs) have which leads to non-linear amplification of the input signal to the amplifier. The input and output voltage characteristics of a typical PA is presented in Figure 5.2 [1].

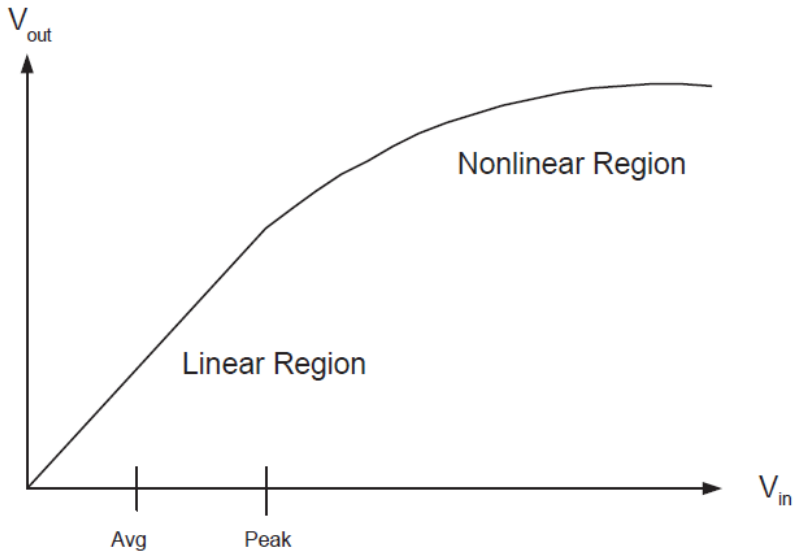

Figure 5.2: PA input-output voltage characteristics.

As can be seen in Figure 5.2, the input voltage is amplified linearly up to some voltage point denoted by "Peak". However, when this peak voltage is surpassed, the linear amplification cannot be maintained.

Ideally, the input signal to the amplifier is expected to be amplified by a constant factor. However, in the non-linear amplification case, harmonics of the frequency components of the input signal appear in the output signal. This results in the leakage of the power in the transmission band to the OOB portions of the frequency spectrum. This is an undesired effect, since the average transmitted power should be reduced in order to satisfy the requirements in a communication standard concerning the maximum OOB radiation levels. Such an action is also referred to as "power back-off".

This will reduce the average transmitted power, which will degrade the SNR levels at the receiver side.

Therefore, simulations comparing any type of modulations with respect to OOB radiations should consider the amplifier non-linearities and its effects. To take the effects of non-linear amplification into account, there are many PA models in the literature. These models are summarized in Section 5.3.2.

5.3.2 Power Amplifier (PA) Models

There are two types of PA models in terms of memory, namely the memoryless PA models and PA models with memory. Memoryless amplifier models assume that the current value of the output signal of the PA depends only on the current value of the input signal to PA, that is, the current value of the output voltage is independent of the past and the future values of the input signal to PA. However, for the PA models with memory, the current value of the output signal of the PA may depend on past or future values of the input signal to PA. Dependence of input and output signals are expressed as Wiener or Volterra series in the PA models with memory, which will not be considered in the scope of this thesis. For the memoryless PA models there are many amplifier models in the literature. The most popular ones are the Saleh model [52] and the Rapp model [53]. A recent modified Saleh model is also reported in [54].

5.3.2.1 Saleh PA Model

Saleh model has AM/AM characteristics, that is, the amplitude of the output signal of PA depends on the the amplitude of the input signal to PA. Furthermore, it has also AM/PM characteristics, that is, there is a phase change in the output signal of PA proportional to the amplitude of the input signal to PA. These characteristics can be given as

$$s_{in}(t) = A_{in}(t)e^{j\phi_{in}(t)}, s_{out}(t) = G(t)e^{j\phi_{in}(t)}e^{j\Phi(t)} \tag{5.2}$$

where

$$G(t) = \frac{g_0 A_{in}(t)}{1 + (A_{in}(t)/A_{sat,in})^2}, \Phi(t) = \frac{\alpha_\phi A_{in}^2(t)}{1 + \beta_\phi A_{in}^2(t)}. \tag{5.3}$$

5.3.2.2 Modified Saleh PA Model

A more recent version of the Saleh model is a model referred to as modified Saleh model [54]. It has both AM/AM and AM/PM characteristics as in Saleh model, which are characterized by

$$s_{in}(t) = A_{in}(t)e^{j\phi_{in}(t)}, s_{out}(t) = G(t)e^{j\phi_{in}(t)}e^{j\Phi(t)} \tag{5.4}$$

where

$$G(t) = \frac{g_0 A_{in}(t)}{\sqrt{1+\beta A_{in}(t)^3}}, \Phi(t) = \frac{\alpha}{\sqrt[3]{1+A_{in}(t)^4}} - \epsilon. \tag{5.5}$$

5.3.2.3 Rapp PA Model

Rapp PA model is another commonly used memoryless PA model. Rather than specifying both AM/AM and AM/PM characteristics as in the Saleh model, the Rapp model has only AM/AM characteristics as in (5.6).

$$s_{out}(t) = \frac{\gamma A_{in}(t)}{(1+(\gamma A_{in}(t)/A_0)^{2p})^{\frac{1}{2p}}} e^{\phi_{in}(t)}. \tag{5.6}$$

5.3.3 Digital to Analog Converter (DAC)

Digital to analog converters (DACs) are used in the modulation types that are examined in this thesis (OFDM, GFDM, WCP-COQAM). Their role in the transmitter is to convert the digital data to be transmitted to an analog signal by sample and hold type interpolation. In Figure 5.3, a typical DAC that works with sample and hold interpolation is presented.

As can be observed in Figure 5.3, the interval between the digital samples in the DAC input is filled with sample and hold type interpolation, that is, the amplitude of the interpolated signal between the two digital samples stays constant at the value of the sample at the beginning of the interval to be interpolated.

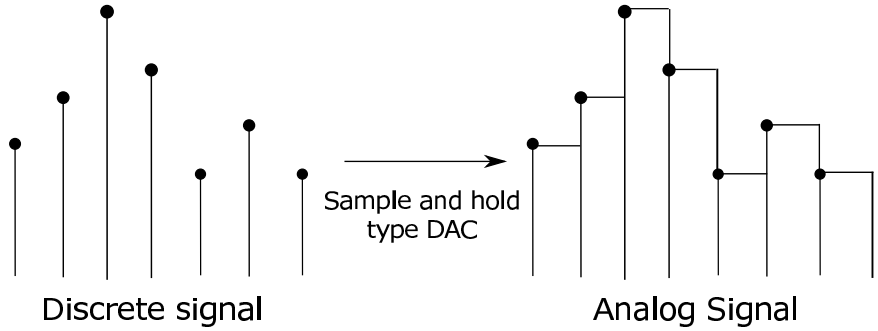

Figure 5.3: Discrete signal input to DAC and the reconstructed analog signal at the output of DAC

To understand the reason why the sample and hold type interpolation increases the OOB radiation, the Fourier transform of the transmitted signal should be considered. Let the discrete signal at the input of the DAC be denoted as $x[n]$. Assume that $x[n]$ represent the samples of a continous time signal g(t), that is $x[n] = g(nT_s)$, where T_s is the sampling rate. In that case, the continous signal at the output of the DAC $y(t)$ can be written as follows.

$$y(t) = g(t) \cdot \sum_{n=-\infty}^{\infty} \delta(t - nT_s) * rect\left(\frac{t - Ts/2}{Ts}\right) \tag{5.7}$$

where $*$ is the convolution operator. Taking the Fourier transform of $y(t)$ to obtain $Y(f)$, one can find

$$Y(f) = \left[G(f) * \frac{1}{T_s} \sum_{n=-\infty}^{\infty} \delta(f - nf_s)\right] P(f) \tag{5.8}$$

where $P(f) = T_s sinc(T_s f) e^{-j\pi f T_s}$ and $f_s = \frac{1}{T_s}$. Therefore,

$$Y(f) = \sum_{n=-\infty}^{\infty} G(f - nf_s) sinc(T_s F) e^{-j\pi f T_s}. \tag{5.9}$$

As can be inferred from (5.9), the frequency spectrum of $y(t)$ is not limited and consists of the replicas of the spectrum of g(t) at the integer multiples of f_s. In fact, multiplication with a sinc term limits the bandwidth of $Y(f)$, but still it has significant components around a few multiples of f_s. Therefore, it can be stated that, while perfect reconstruction of the analog signal to be transmitted from the discrete time samples at the input of the interpolator is possible with a sinc interpolation, which will

suppress the harmonic components at every f_s, due to its low-pass filtering nature, sample and hold type reconstruction results in a signal with significant components falling into OOB. This will result in higher OOB values. Therefore, in the simulations related to OOB comparisons of OFDM, GFDM or WCP-COQAM, the effect of DAC will also be considered.

5.4 OOB Radiation Comparisons between OFDM and FBMC

In literature, there are various studies comparing OFDM and FBMC in cognitive radio applications. For example, in [55], a new resource allocation scheme in a downlink communication scenario has achieved higher bandwidth efficiency when it is used with FBMC in comparison to its application with OFDM. Furthermore, FBMC has shown superior performance in terms of spectral efficiency compared to OFDM in an uplink scenario in [56]. The reason for the performance loss for OFDM is mainly due to its high OOB created owing to the fact that the rectangular pulse has slow decaying property in the frequency domain. However, for FBMC, pulse shaping yields pulses that have lower out-of-band performance. Since lower OOB results in less interference between the adjacent users in frequency domain, higher spectral efficiency values are obtained for FBMC in CR application, either in uplink or downlink, compared to OFDM.

However, although there are many methods that are used to suppress OOB radiation, they are not used in [55] or [56] for OFDM. These methods are summarized in Section 5.5.

5.5 OOB Radiation Suppression Techniques

5.5.1 Windowing

Windowing is a method that is applied to decrease the out-of-band emissions. It works by the way of smoothing the rapid changes that appear in the impulse response of the pulse-shaping filter that is used. Therefore, it can be considered as a low-

pass filtering, which obviously suppresses the high frequency content of the low-pass equivalent of the transmitted signal, which corresponds to the frequency content of the transmitted signal that falls out of the transmission band.

Since OFDM has large side-lobes, windowing is widely applied for OFDM. In that case, it is referred to as filtered OFDM or windowed OFDM (W-OFDM). The pulse shape for an OFDM signal after windowing can be expressed as

$$p_W(t) = \text{rect}(\frac{t - T'/2}{T'}) \cdot g(t) \tag{5.10}$$

where

$$rect(t/T') = \begin{cases} 1, & \text{if } |t| \leqslant T'/2 \\ 0, & \text{otherwise.} \end{cases} \tag{5.11}$$

Here what T' corresponds to will be clear. $g(t)$ in (5.10) can be defined as

$$g(t) = \begin{cases} w(t + T/2 + T_0/2), & \text{if } -T/2 - T_0/2 \leqslant t \leqslant -T/2 + T_0/2 \\ 1, & \text{if } -T/2 + T_0/2 < t < +T/2 - T_0/2 \\ w(t - T/2 + 3T_0/2), & \text{if } +T/2 - T_0/2 \leqslant t \leqslant +T/2 + T_0/2 \\ 0, & \text{otherwise.} \end{cases} \tag{5.12}$$

where $w(t)$ is the windowing function and T is the OFDM symbol duration. T_0 is the half of the duration of the windowing function $w(t)$ and $T' = T + T_0$. All these parameters are presented in Figure 5.4, which shows the construction of g(t) from an arbitrary windowing function $w(t)$ according to the equation given in (5.12).

There are many different types of windowing functions $w(t)$ in the literature. For example, Hamming and Hanning windows are given by a general formula below.

$$w(t) = \begin{cases} K\left(\alpha - \beta cos(\frac{\pi t}{T_0})\right), & \text{if } 0 \leqslant t \leqslant 2T_0 \\ 0, & \text{otherwise.} \end{cases} \tag{5.13}$$

For Hamming and Hanning windows, $\alpha = 0.54, 0.5$ and $\beta = 0.46, 0.5$, respectively. Another widely used window is a Blackman window, which can be expressed as

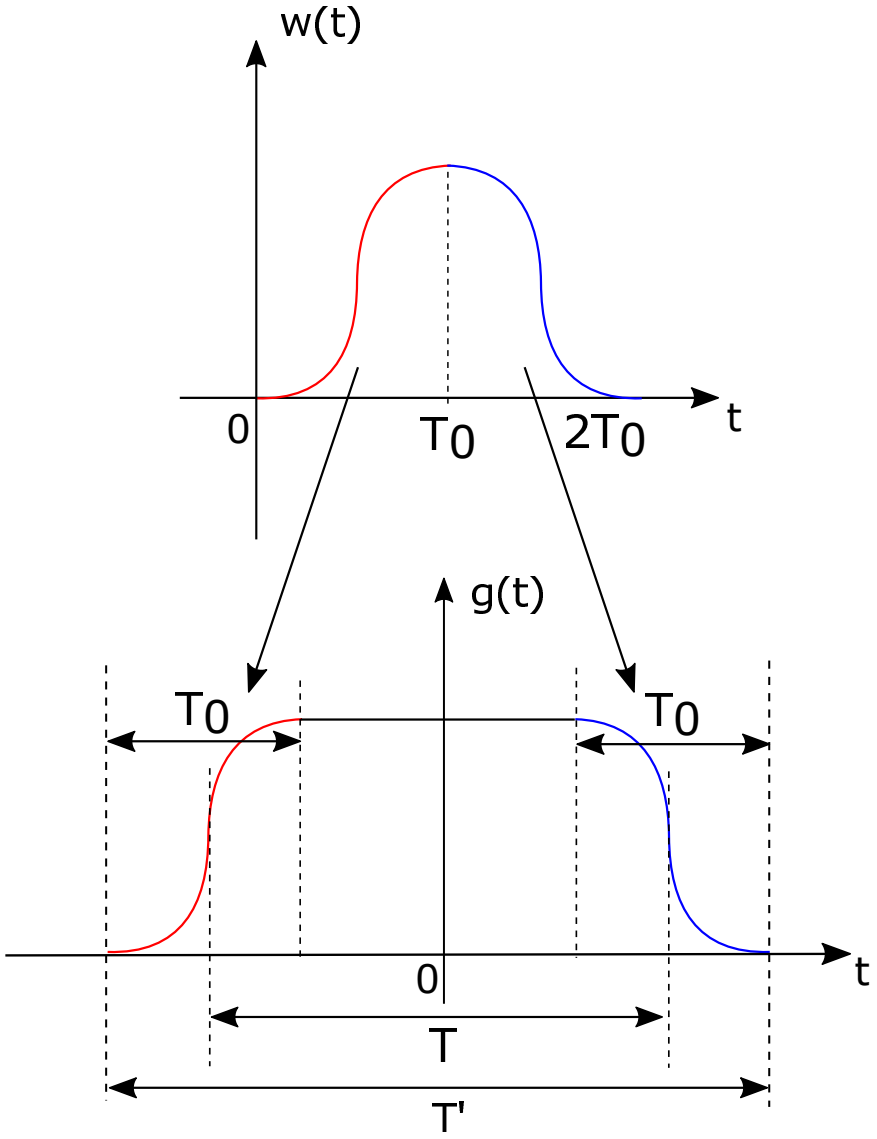

Figure 5.4: Construction of $g(t)$ from the windowing function $w(t)$

$$w(t) = \begin{cases} K\left(0.42 + 0.08cos(\frac{2\pi t}{T_0}) - 0.5cos(\frac{\pi t}{T_0})\right), & \text{if } 0 \leqslant t \leqslant 2T_0 \\ 0, & \text{otherwise.} \end{cases} \tag{5.14}$$

Subsequent OFDM symbols for which windowing is applied is presented as in Figure 5.5. In Figure 5.5 (a), T corresponds to the OFDM symbol duration for the case

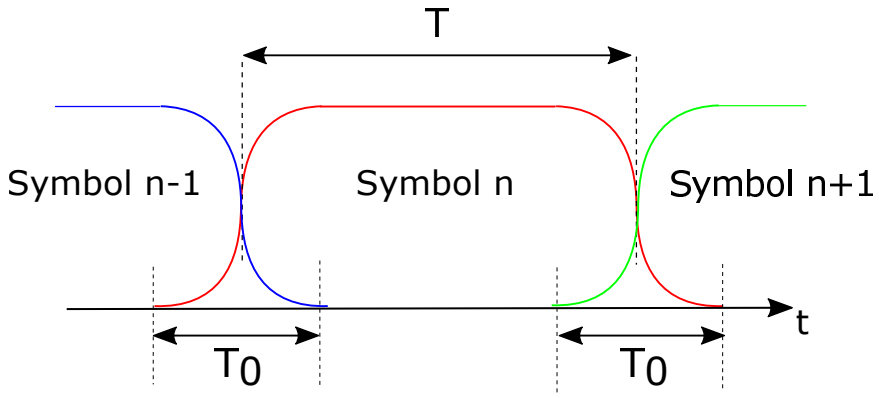

Figure 5.5: Transmitted pulse shape along with the neighbouring OFDM symbols when windowing is applied.

when no windowing is applied, and T_0 is the transition duration between the transmitted subsequent symbols created due to the windowing function. Total OFDM symbol duration is $T' = T + T_0$. Therefore, there is a loss of transmission efficiency owing to non-zero T_0. The spectral efficiency loss owing to windowing, η_{W-OFDM} is

$$\eta_{W-OFDM} = \frac{T_0}{T}. \tag{5.15}$$

In order for the spectral efficiency loss to be small, T_0 should be selected as small as possible. However, since windowing operation is effectively a low-pass filtering, small T_0 will result in a higher cut-off frequency for the equivalent low-pass filtering effect, this will increase the OOB emissions. Therefore, in the design of the windowing function and T_0, the trade-off between the OOB radiation suppression and spectral efficiency loss should be considered.

5.5.2 Guard Subcarriers

Guard subcarriers are the subcarriers that are placed at both sides of the transmission bandwidth, which contains the subcarriers that carry the information symbols and possible pilot symbols. The aim of the insertion of guard subcarriers is to establish a guard region between the active subcarriers and the users that may be at the neighbouring bands. Via such a guard band, the interference created between the adjacent users in the subsequent bands are reduced. In Figure 5.6, the insertion of guard subcarriers around the data and pilot subcarriers are illustrated.

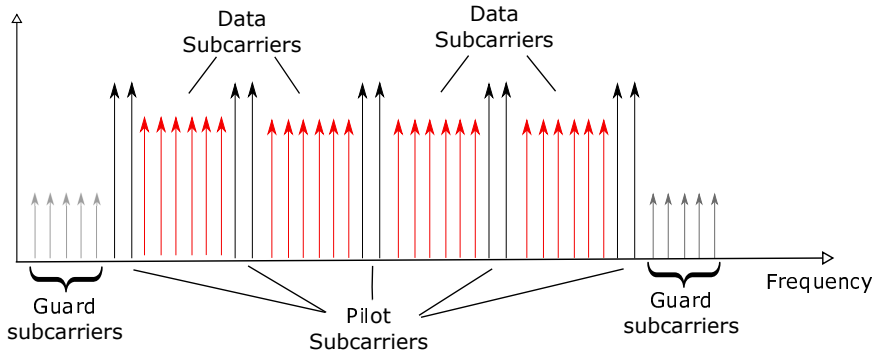

Figure 5.6: Insertion of guard subcarriers to reduce OOB emissions

In Figure 5.6, the subcarriers that carry the information symbols are referred to as data sub-carriers, whereas the sub-carriers that are allocated to be used for timing or frequency synchronization or channel estimation tasks are represented as pilot subcarriers. As can be seen, guard subcarriers are placed at both ends of the transmission bandwidth.

Forming a guard region composed of guard subcarriers is simple. The only thing to do is to use the subcarriers in the transmission band to carry the data and pilot symbols and do not utilize some of the subcarriers at both ends of the spectrum as illustrated in Figure 5.6. This means that zeros will be transmitted by the guard subcarriers, that is, no transmission is carried out over some of the subcarriers that are at both ends of the transmission bandwidth, which makes these subcarriers be called "guard subcarriers".

5.5.3 Other Techniques

There are also some techniques other than windowing or insertion of guard subcarriers in the literature. The first possible technique is using cancellation carriers (CC) to suppress OOB emissions [57], [58]. In this method, in addition to the data subcarriers, which carry the information to be transmitted, a number of subcarriers are placed at both sides of the transmission bandwidth with appropriate weighting in order to minimize the interference caused in a specific portion of the frequency spectrum. On the other hand, employing CCs to minimize the out-of-band radiation in a specific portion of the spectrum has the disadvantage of having larger peak-to-average-power-ratio (PAPR) [59]. Therefore, in [59], another method is proposed which is referred to as adaptive symbol transition (AST) to limit OOB radiation in OFDM. It is similar to the windowing technique in that OFDM symbols are extended in time in order to have a smoother transition. However, rather than using a static windowing filter, the signal during the transition is adapted according to the transmitted data. In this way, PAPR is not increased much while OOB emissions are suppressed.

Now that the disadvantages of high OOB radiation are examined and the techniques to reduce OOB radiation are discused, the next section will compare OFDM, GFDM and WCP-COQAM in terms of OOB radiation levels in presence of OOB radiation reduction techniques.

5.6 Comparison of OFDM, GFDM and WCP-COQAM in terms of OOB radiation

In this section, OOB radiation of OFDM, GFDM and WCP-COQAM will be compared. In fact, there are already such comparisons in the literature. For example, GFDM is shown to create lower OOB radiation compared to OFDM in [7]. However, the OOB comparisons are not made at equal spectral efficiency conditions, that is, the number of subcarriers in OFDM, is not equal to the product of the number of subcarriers in GFDM and the number of GFDM symbols in a GFDM frame. In other words, the number of subcarriers in an OFDM symbol is not equal to $T \cdot K$. Furthermore, GFDM is also shown to have even better OOB radiation performance,

when windowing and insertion of guard subcarrier techniques are applied as detailed in [7]. However, while giving such comparisons, these techniques are not applied to OFDM, which deems the OOB radiation comparison unfair in [7].

Similarly, in [17], WCP-COQAM is compared with OFDM, which revealed the superiority of WCP-COQAM over OFDM in terms of OOB radiations. However, the OOB radiation comparisons in [17] are considered to convey trivial results since WCP-COQAM has windowing but OFDM does not have. For a fair comparison, windowed OFDM (W-OFDM) should be compared with WCP-COQAM with respect to the OOB emissions. Furthermore, as in [7], the OOB comparisons in [17] are not made under equal spectral efficiency conditions.

Therefore, the simulations that will be performed to compare the OOB radiations of OFDM, GFDM and WCP-COQAM in this thesis will also be performed under fair conditions, that is, the comparisons will also be carried out under equal spectral efficiency conditions and OOB radiation reduction techniques such as windowing or insertion of guard subcarriers will also be applied for OFDM.

The simulations related to the comparison of OFDM, GFDM and WCP-COQAM in terms of OOB radiation that is presented in the subsequent sections mainly consist of two parts. In the first part, the non-ideal effects of PA and DAC is not considered, whereas in the second part they are included, in addition to other distortions created by PA and DAC.

5.6.1 Simulation Results with no PA or DAC

In this section, simulations concerning OOB radiations will be carried out without considering PA and DAC effects. For the OOB radiation comparisons of OFDM, GFDM and WCP-COQAM, simulation parameters are selected as in Table 5.2.

Simulations will be performed when OFDM, GFDM and WCP-COQAM have equal or unequal spectral efficiency. For the simulations carried out under unequal spectral efficiency conditions, the number of subcarriers, namely K, is taken to be 128 for the three different modulation types. When guard symbol insertion technique is used, out of 128 subcarriers, the number of guard subcarriers is taken to be 52. The number of

Table 5.2: Simulation Parameters

Total number of subcarriers (K)	128 or 1152
No. of guard subcarriers	52 or 468
No. of symbols in GFDM frame	9
Pulse shape	RC (with roll-off=0.1)
Constellation order	16-QAM
CP length	32 samples
Interpolation filter type	RC pulse with roll-off=0.1
Upsampling Rate	6
Interpolation filter duration	81 samples
No. of Monte-Carlo simulations	40
Spectral estimation method	Periodogram
Windowing function	Hanning, 18 samples from both sides

subcarriers being 128, out of which 52 are guard subcarriers, are taken from the possible choices that are specified in LTE standard [13]. In addition, cyclic prefix length is selected to be 32, which is the long CP selection when the number of subcarriers is 128 in [13]. When the guard symbol insertion technique is utilized, OFDM, GFDM and WCP-COQAM modulation types will be referred to as G-OFDM, G-GFDM, GWCP-COQAM, respectively. Similarly, if windowing technique is applied, OFDM and GFDM will be called as W-OFDM and W-GFDM. There is no change for the name of WCP-COQAM since it has windowing by default in its name. Furthermore, if both windowing and guard symbol insertion techniques are used in OFDM, GFDM and WCP-COQAM, they will be named as GW-OFDM, GW-GFDM and GWCP-COQAM.

Note that the number of subcarriers is 1152 for OFDM for the simulations that are made under equal spectral efficiency conditions. This results from the fact that the number of subcarriers of OFDM should be equal to the multiplication of the number

of subcarriers in GFDM or WCP-COQAM, which is 128, with the number of GFDM symbols in a GFDM frame, which is 9, in order for equal spectral efficiency conditions to apply. The multiplication yields 1152, which is the number of subcarriers for OFDM under equal spectral efficiency conditions.

One may wonder the reason why the length of the windowing function is taken to be 18 samples. In fact, since the length of the windowing function is not specified in LTE standard [13], it is taken to be 18 samples. The windowing function is selected to be Hanning, which is amongst the possible windowing functions discussed in Section 5.5.

Another important point may be about the selected constellation order. It is selected to be 16-QAM. This originates from the fact that in [7], for the OOB comparisons between GFDM and OFDM, the constellation order selection is 16-QAM. In order to see that our results are in agreement with the results in [7], the constellation orders are selected to be the same. Moreover, the number of GFDM symbols in a GFDM frame is also selected to be 9. Note that, it is an odd number since the number of GFDM symbols in a GFDM frame must be an odd number, in order that a ZF receiver can be used [30] in GFDM.

The power spectral densities (PSDs) of the signals are found by using the periodogram method. Although there exists better spectral estimation methods such as Welch or Bartlett methods [60], periodogram is an asymptotically unbiased estimator. In our simulations, it has been observed that 40 Monte-Carlo simulations are enough to attain stable OOB emissions curves, thus it makes sense to conclude that periodogram provides the unbiased estimates with the specified number of Monte-Carlo simulations.

Another point that may be significant is how oversampling is made to be able to observe the frequency range larger than the transmission bandwidth. In the simulations, the time-domain signals are sixfold oversampled with an RC filter that has a length of 81 samples. However, after filtering, the samples are truncated from both sides such that total number of samples of the upsampled signal is 6 times that of the original signal. In fact, such a truncation could also not be made, but it will come with a loss of spectral efficiency, owing to the delay caused by the interpolation filter, which will

increase the required CP length between the OFDM symbols. Furthermore, if a truncation is not made, the interpolation filter itself creates the effect of windowing, which results in observations in which windowing has no or little effect in suppressing the OOB radiation, since interpolation filter itself shows the effect of windowing.

5.6.1.1 Unequal Spectral Efficiency Conditions

With the specified simulation parameters in Table 5.2, the out-of-band radiations of OFDM, GFDM and WCP-COQAM under unequal spectral efficiency conditions, with or without windowing are presented in Figure 5.7.

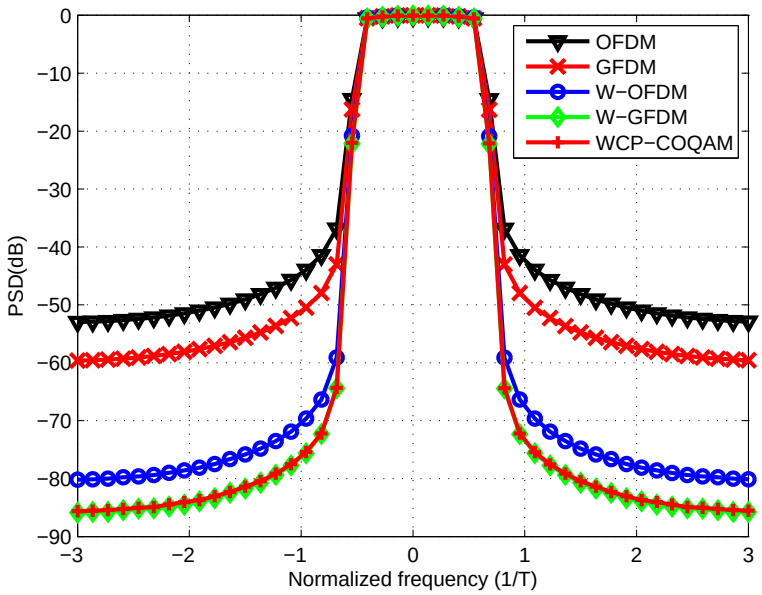

Figure 5.7: PSD of OFDM, GFDM and WCP-COQAM under unequal spectral efficiency conditions with or without windowing

As can be observed in Figure 5.7, there is a significant difference between the out-of-band radiations of OFDM and GFDM. The PSD values at 3 times the normalized frequency (3/T) are about -53dB and -60dB, for OFDM and GFDM, respectively. Application of windowing decreases the OOB radiations dramatically. It is able to result in about 30dB less PSD values at 3/T either for OFDM or GFDM. An interesting observation may be that the difference between the OOB radiations of OFDM

and GFDM decreases with the application of Hanning window. However, there is still a significant performance difference between W-GFDM, WCP-COQAM and W-OFDM. It should also be noted that W-GFDM and WCP-COQAM shows similar OOB emissions, which indicates that using OQAM instead of QAM does not change anything with respect to OOB radiations. These results are in agreement with some of the results in [7], which states that GFDM has lower OOB radiation compared to OFDM. However, as also discussed before, these comparisons should be made under equal spectral efficiency conditions in order to be more fair. Before giving the results for the equal spectral efficiency case, OOB radiation results will be presented when guard symbol insertion is also applied as an OOB radiation suppression method. These results are depicted in Figure 5.8.

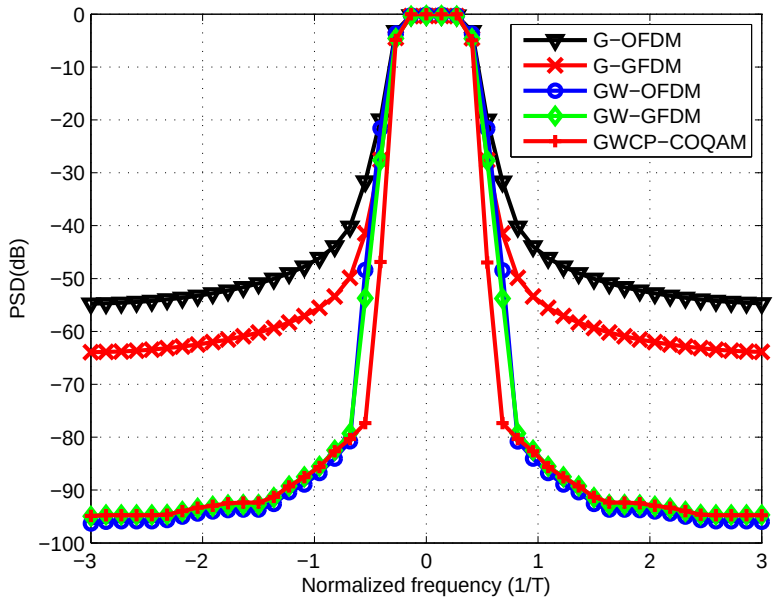

Figure 5.8: PSD of OFDM, GFDM and WCP-COQAM under unequal spectral efficiency conditions with guard symbol insertion and windowing

Note that the transmission bandwidth portion seems to be shortened in Figure 5.8 compared to that observed in Figure 5.7. This is owing to the fact that some of the subcarrriers are "turned off", that is, no symbol is transmitted over them, which makes these subcarriers called as guard subcarriers. Moreover, when G-OFDM and G-GFDM in Figure 5.7 is compared to OFDM and GFDM in Figure 5.7, there is ap-

proximately 2-3 dB change in the PSD values at 3/T. This corresponds to the OOB suppression effect of the guard symbol insertion. Moreover, as can also be seen from Figure 5.8 although G-GFDM has about 10dB less OOB radiation compared to G-OFDM, when both windowing and guard symbol insertion is applied to all of the three modulations, there is no significant difference between their OOB radiations. Therefore, it can be stated that if windowing and guard symbol insertion techniques, which are commonly used to reduce OOB radiation levels, are utilized, there is no significant difference between the OOB radiations of OFDM, GFDM and WCP-COQAM, even under unequal spectral efficiency conditions.

Now that, many of the OOB reduction techniques, which are windowing and guard symbol insertion, are used to see the OOB radiation of OFDM, GFDM and WCP-COQAM under unequal spectral efficiency conditions, the simulations continue with the case when OFDM has the same spectral efficiency as GFDM or WCP-COQAM.

5.6.1.2 Equal Spectral Efficiency Conditions

As mentioned before, a fair comparison of the OOB radiations of OFDM, GFDM and WCP-COQAM should be made under equal spectral efficiency conditions. Such conditions can be met when the number of subcarriers that is used in OFDM equals to the product of the number of subcarriers in GFDM or WCP-COQAM, which is denoted by K, by the number of GFDM symbols in a GFDM frame, which can also be denoted as T. This means that the number of subcarriers used in OFDM is T times larger than that used in GFDM or WCP-COQAM. This, in fact, causes an increased CFO vulnerability for OFDM, due to having more subcarriers in the same bandwidth. Hence, OFDM may suffer more form CFO compared to GFDM. However, such simulations, which revealed no higher CFO vulnerability for OFDM compared to GFDM, are also done in Chapter 3. This further validates the fairness of the comparison of the OOB radiations of OFDM, GFDM and WCP-COQAM under equal spectral efficiency conditions. Using the simulation parameters in Table 5.2, the PSDs of the three modulation types, for some of which windowing is applied as an OOB reduction technique, are presented in Figure 5.9.

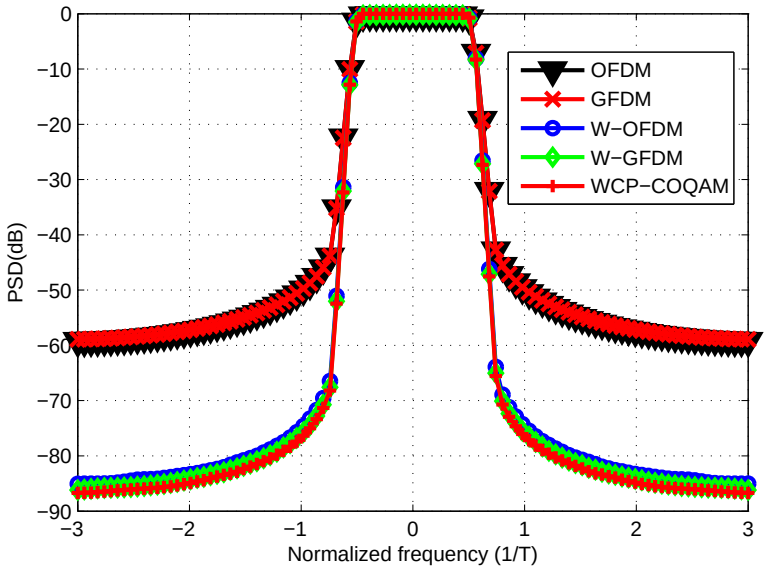

Figure 5.9: PSD of OFDM, GFDM and WCP-COQAM under equal spectral efficiency conditions with or without windowing

As can be seen in Figure 5.9, when the spectral efficiencies of OFDM and GFDM are the same, they show the same performance in terms of the OOB radiation. For unequal spectral efficiency case, GFDM has a 7-8 dB advantage over OFDM, whereas they are the same for the equal spectral efficiency case. Moreover, if windowing is applied, all of the modulation types produce the same performance with respect to OOB radiation. Note that, there was a 4-5 dB difference in the PSD values at 3 times the normalized frequency between W-OFDM and W-GFDM for the unequal spectral efficiency case. In short, equating the spectral efficiencies, the OOB performances of OFDM, GFDM and WCP-COQAM are made the same, either with or without windowing.

The last part of the simulations includes the application of guard symbol insertion for the three modulation types under equal spectral efficiency conditions. Corresponding results are presented in Figure 5.10.

As can be observed from Figure 5.10, in all possible configurations, OFDM, GFDM and WCP-COQAM gives the same OOB radiation values. For example, if only guard symbol insertion is applied, OFDM and GFDM perform the same. In comparison to the PSD values of OFDM and GFDM, for which no windowing or guard sym-

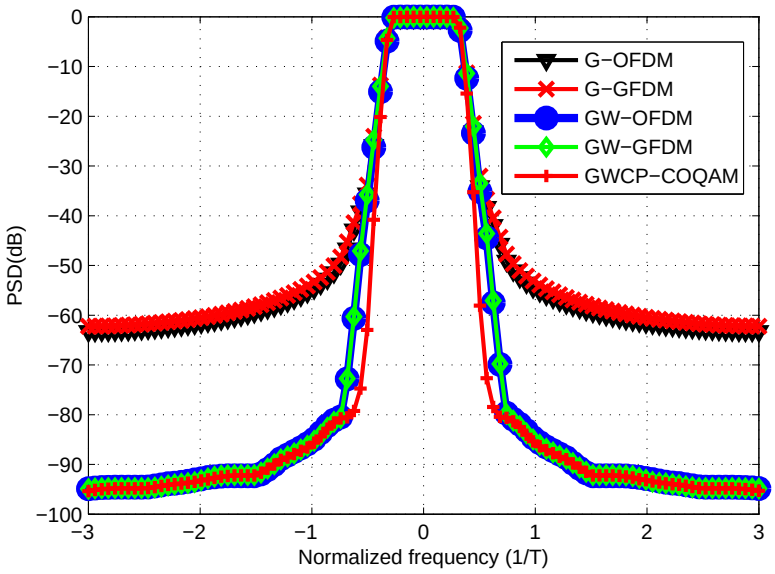

Figure 5.10: PSD of OFDM, GFDM and WCP-COQAM under equal spectral efficiency conditions with guard symbol insertion and windowing

bol insertion is used, which can be observed in Figure 5.9, guard symbol insertion is responsible for about 5dB reduction in the PSD values according to Figure 5.10. Moreover, if both windowing and guard symbol insertion is applied, OFDM, GFDM and WCP-COQAM again gives the same OOB emission values. If the PSD values of W-OFDM, W-GFDM and WCP-COQAM at 3 times the normalized frequency, which can be observed in Figure 5.9, are compared to that of GW-OFDM, GW-GFDM and GWCP-COQAM in Figure 5.10, it can be stated that guard interval insertion gives about 10dB fall in the PSD values. Note that, this reduction was about 5dB when there was no windowing. Therefore, these results convey that guard symbol insertion does not affect the PSD values linearly. Its effect is enhanced when it is used along with windowing, which is in fact the common practice.

All in all, when the spectral efficiencies of OFDM, GFDM and WCP-COQAM are equated, there is no OOB radiation performance difference between any two of the three modulations types, with or without any of the OOB reduction techniques that are used in the simulations, which are windowing or guard symbol insertion.

5.6.2 Simulation Results with PA and DAC

In this section, the effect of PA and DAC at the transmitters of OFDM, GFDM and WCP-COQAM are considered. The block diagram that shows the elements in the transmitter for the three modulation types is presented in Figure 5.11.

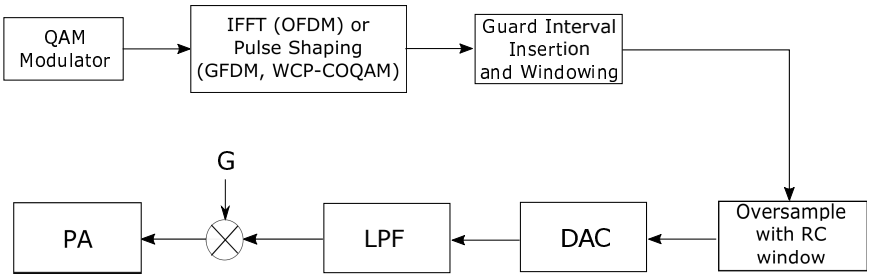

Figure 5.11: The transmitter block diagram with DAC and PA

As can be observed in Figure 5.11, the IFFT of the modulated symbols at the output of the modulator is taken for OFDM. For GFDM or WCP-COQAM, this IFFT block is replaced by the pulse shaping block. Then the OOB reduction methods, guard interval insertion and windowing are applied. After that, to see a frequency range larger than the transmission bandwidth, the signal is sixfold oversampled with an RC pulse of roll-off 0.1. This signal at the output of the oversampling with RC pulse block can be considered to be the signal whose PSD is found in the first part of the simulations. To observe the effect of the sample-and-hold behavior of DAC in the simulations, the samples at the input of DAC are repeated 11 times. Then, an additional low-pass filtering is carried out with a 5^{th} degree Butterworth filter of 4.9MHz cut-off frequency to suppress the replicas created in the frequency spectrum of the output signal of DAC due to the sample and hold behavior of DAC, which are discussed in Section 5.3.3. Note also that the transmission bandwidth is selected to be 10 MHz in the simulations. This choice is made since the closest number of subcarrier selection to our choice, which is 1152, was 1024 in LTE standard, for which the transmission bandwidth is specified to be 10MHz. Following the DAC block, the input to the PA block is multiplied by a gain factor of g. The importance of this gain factor will be discussed shortly. After such a multiplication, the signal is fed to the PA block, which is the last element in the transmitter.

The simulation procedure in this section can be expressed as follows. First, the simulations are done with an initial value of the gain factor k. Then, the PSD of the output signal is plotted. If it surpasses the limits specified in the spectral emission mask in the LTE standard, the details of which are given in Table 5.1, the value of the gain factor, g, is decreased. If the observed PSD is well below the emission mask, the gain factor is increased. This procedure continues until the signal barely complies with the spectral mask requirements. In fact, the specified procedure is the same as that in [61] that compares OFDM and single-carrier transmission with frequency domain equalization considering spectral mask requirements in WiMAX.

At the value of the gain factor g value, for which the spectral mask is barely satisfied, three different parameters of the PA output signal is found. These parameters are the transmitted power, error-vector magnitude (EVM), and signal to interference ratio (SIR). EVM and SIR are defined as

$$EVM = \frac{\sigma_I}{A_{max}}, SIR = \frac{\sigma_s^2}{\sigma_I^2} \tag{5.16}$$

where σ_I^2, σ_s^2 and A_{max} are the interference power, signal power and maximum signal amplitude, respectively, as defined in [62].

In the simulations, the modulation type amongst OFDM, FBMC and WCP-COQAM, that has the highest transmitted power satisfying the defined spectral mask, with acceptable distortion values observed from the EVM or SIR of the transmitted signal, will be considered to be advantageous over the others.

For the simulation parameters, the ones in Table 5.2, which are used for equal spectral efficiency conditions case in the first part of the simulations are selected except that Gaussian pulse is used for WCP-COQAM rather than RC pulse. For example, the number of subcarriers in OFDM is selected to be 1152, rather than 128. Furthermore, in this section, windowing and guard symbol insertion will be applied for all cases in the simulations. However, the modulations will be referred to as OFDM, GFDM, WCP-COQAM, rather than GW-OFDM, GW-GFDM and WCP-COQAM.

The PA models that are presented in Section 5.3.2 are all included in the simulations. For the Saleh model, the constants are selected as $(g_o, \alpha_\phi, \beta_\phi, A_{sat,in}) = (1, \pi/4, 0.25, 2V)$ as in [63]. For the modified Saleh model, the parameters are se-

lected as $(\alpha, \epsilon, g_0, \beta) = (0.161, 0.124, 1.0536, 0.086)$ which are the selections in [54]. The Rapp model parameters are also chosen as $(\gamma, A_0, p) = (1, 1V, 2)$ as in [61].

An illustration of the condition for which the transmitted signal in OFDM barely satisfies the LTE spectral mask is presented in Figure 5.12.

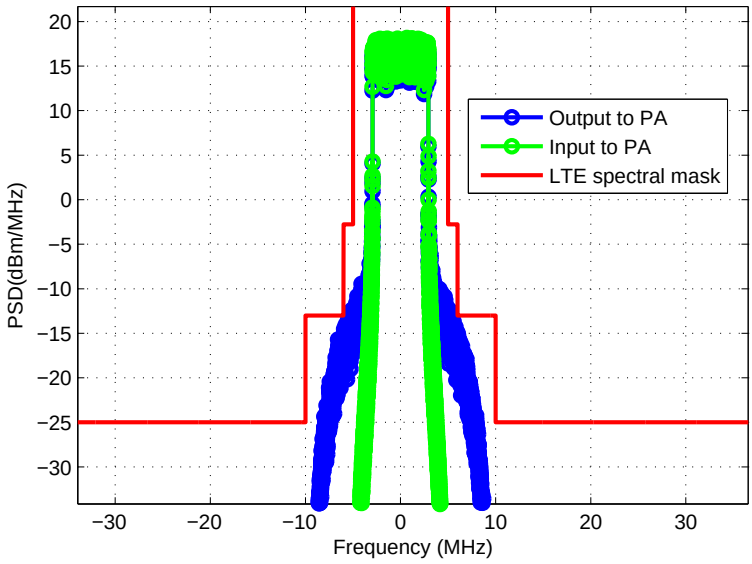

Figure 5.12: PSDs of the low-pass equivalent OFDM signals, before and after PA (Rapp PA model)

In Figure 5.12, the PSDs of the signals modulated with OFDM at the input and output of the PA are plotted. The PA model in Figure 5.12 is the Rapp PA model. Moreover, the spectral mask specified in Table 5.1 can also be observed in Figure 5.12. Note that, there is no spectral mask requirement for the frequency range defined in the transmission bandwidth, which lies in the frequencies between -5MHz and 5MHz, since no such limitation is specified in the LTE spectral mask requirements.

The effect of PA, which increases the OOB radiation can also be observed in Figure 5.12. The PSD of the signal at the input of the PA has lower PSD values for the frequencies that fall out of the transmission bandwidth, which is between -5 MHz and 5 MHz. As can also be observed, the signal at the output of PA barely complies with the spectral mask, as the PSD values touches the spectral mask limits at about ± 6 MHz. At that point, the EVM, SIR and the average transmitted power is found. Similar procedure is also applied for the other PA models and the other modulation types, which are GFDM and WCP-COQAM.

Such a procedure yields the transmitted power, EVM and SIR values, which are presented for Saleh, Modified Saleh, and Rapp model PAs in Table 5.3, Table 5.4 and Table 5.5, respectively.

Table 5.3: EVM, SIR and the transmitted power values for OFDM, GFDM and WCP-COQAM when Saleh model PA is used

Modulation Type	EVM (%)	SIR(dB)	Transmitted Power (mW)
OFDM	2.17	30.74	181
GFDM	2.16	30.78	183
WCP-COQAM	2.16	30.76	174

Table 5.4: EVM, SIR and transmitted power values for OFDM, GFDM and WCP-COQAM when Modified Saleh model PA is used

Modulation Type	EVM (%)	SIR(dB)	Transmitted Power (mW)
OFDM	2.17	30.74	483
GFDM	2.16	30.75	490
WCP-COQAM	2.17	30.74	491

Table 5.5: EVM, SIR and transmitted power values for OFDM, GFDM and WCP-COQAM when Rapp model PA is used

Modulation Type	EVM (%)	SIR(dB)	Transmitted Power (mW)
OFDM	2.16	30.76	217
GFDM	2.17	30.77	211
WCP-COQAM	2.15	30.75	210

As can be observed from Table 5.3-5.5, the highest transmission power is observed for the Modified Saleh PA model. However, there is no significant difference between the transmitted powers of OFDM, GFDM and WCP-COQAM for any of the models. Moreover, the EVM and SIR values are extremely close to each other. From these results, it can be stated that there is no significant difference between OFDM, GFDM and WCP-COQAM in terms of the transmitted power values which are observed with similar distortion levels in the simulations carried out. These simulations are performed under a practical scenario considering the spectral mask requirements in a communication standard, which is selected to be LTE, with the inclusion of the effects of DAC and PA, which are fundamental elements in a transmitter. The results also mean that the three modulation types suffer similarly from the PA non-linearity, with close values of average transmitted powers, which leads to the conclusion that their peak-to-average power ratio (PAPR) values are also similar.

In summary, although GFDM or WCP-COQAM is shown to have better performance compared to OFDM in terms of OOB emissions in [7], [17], this result does not hold when the three modulation types are compared under fair conditions, that is, when their spectral efficiencies are the same and OOB emission reduction techniques are applied also to OFDM. In fact, even under unequal spectral efficiency conditions, if both windowing and guard symbol insertion is applied, their OOB emissions are similar. Furthermore, in a more practical scenario, taking into account the spectral mask requirements and the effects of DAC and PA, their transmitted power performance turned out to be very close to each other with similar levels of distortion in the transmitted signals, which are observed with SIR and EVM parameters. These results imply that there is no significant advantage of GFDM or WCP-COQAM over OFDM, with respect to OOB emission levels for the cases that are included in the simulations.

CHAPTER 6

CONCLUSION AND FUTURE WORK

In this thesis, the claimed advantages of GFDM, which is one of the most popular candidate physical layer modulation scheme to be used in 5G communication systems, and its variant WCP-COQAM compared to OFDM are investigated in terms of different performance metrics. The first claimed advantage is about the OOB emissions. In [7] and [17], GFDM and WCP-COQAM are shown to yield better performance in terms of OOB radiations. However, these comparisons are not carried out under fair conditions. The unfairness results from the fact that the OOB emission reduction techniques such as windowing or guard symbol insertion was only applied for GFDM or WCP-COQAM. In the OOB emission simulations included in this thesis, these techniques are also applied for OFDM. In that case, it was observed that when both guard symbol insertion and windowing is applied, there is no difference between the OOB emissions between the three inspected modulation schemes.

Another unfairness in the OOB emission comparisons in the literature is the fact that these comparisons are not made under equal spectral efficiency conditions. In OOB simulations in this thesis, OOB emissions are also compared when the three modulation schemes are at equal spectral efficiency. Under such conditions, it has been shown that OOB emissions are the same for OFDM, GFDM and WCP-COQAM regardless of whether windowing or guard symbol insertion techniques are used or not. In addition to the observations of OOB emissions over the PSD estimates, the OOB emission performance of the three modulations are compared in a much more practical scenario in which the effects of amplifier nonlinearity and digital to analog converter is also included. Under such effects, parameters related to the transmitted

signals such as the average transmitted power, error vector magnitude and signal to interference ratio are found for the three modulation types under spectral mask requirements defined in the LTE standard. However, no important difference between OFDM, GFDM and WCP-COQAM is observed in terms of these parameters.

Other than the comparisons related to OOB emissions, the three modulation types are also compared with respect to their CFO immunities. Such simulations are made since FBMC techniques, of which GFDM or WCP-COQAM are special cases, are reported to be more robust to CFO compared to OFDM. Their CFO immunity performances are evaluated in terms of their error rate performances under CFO in various channel types. Furthermore, these simulations are also carried out under unequal or equal spectral efficiency conditions. For the channel types and pulse shapes that are included in simulations, neither GFDM nor WCP-COQAM yielded better CFO immunity compared to OFDM.

In order to explore whether the CFO immunity of WCP-COQAM can be made better than OFDM via pulse-shaping, discrete Zak transform based pulse shaping methods are considered for WCP-COQAM. Since a pulse that satisfies the orthogonality conditions defined for OQAM-OFDM are mathematically proved to imply orthogonality when it is used for WCP-COQAM, which constitutes the main analytical contribution of this thesis, the advanced pulse shaping methods defined for OQAM-OFDM, which yield minimum time frequency localization pulses, are also applied to WCP-COQAM. With such pulses, the error rate performances of WCP-COQAM and OFDM are again compared under CFO, which has not yielded any better CFO immunity for WCP-COQAM.

All in all, the results in this thesis point out that WCP-COQAM or GFDM does not perform better in terms of the inspected performance metrics compared to OFDM. Since the implementation of OFDM, which is composed of simple IFFT and FFT blocks at the transmitter and the receiver, is simpler than GFDM or WCP-COQAM, which requires matrix multiplications at the transmitter or receiver side to implement the pulse shaping filters. Future work may concentrate on the pulse-shaping, since the flexibility of GFDM or WCP-COQAM is mainly at that stage. The reason for the fact that no better CFO immunity is obtained for WCP-COQAM although optimal time

frequency localized pulses are used can be inspected through an even more analytical perspective. If the reasons are understood better, new pulse designs can be made accordingly for WCP-COQAM or GFDM to have better CFO immunity or OOB emission performance compared to OFDM.

REFERENCES

[1] A. Goldsmith, *Wireless Communications*. New York, NY, USA: Cambridge University Press, 2005.

[2] R. V. Nee and R. Prasad, *OFDM for Wireless Multimedia Communications*. Norwood, MA, USA: Artech House, Inc., 2004.

[3] H. Bölcskei, P. Duhamel, and R. Hleiss, "Orthogonalization of OFDM/OQAM pulse shaping filters using the discrete Zak transform," *Signal Process.*, vol. 83, no. 7, pp. 1379 – 1391, Jul. 2003.

[4] P. Siohan, C. Siclet, and N. Lacaille, "Analysis and design of OFDM/OQAM systems based on filterbank theory," *IEEE Trans. Signal Process.*, vol. 50, no. 5, pp. 1170–1183, May. 2002.

[5] B. Farhang-Boroujeny, "OFDM versus filter bank multicarrier," *IEEE Signal Process. Mag.*, vol. 28, no. 3, pp. 92–112, May. 2011.

[6] H. Ochiai and H. Imai, "On the distribution of the peak-to-average power ratio in OFDM signals," *IEEE Trans. Commun.*, vol. 49, no. 2, pp. 282–289, Feb. 2001.

[7] N. Michailow, M. Matthe, I. Gaspar, A. Caldevilla, L. Mendes, A. Festag, and G. Fettweis, "Generalized frequency division multiplexing for 5th generation cellular networks," *IEEE Trans. Commun.*, vol. 62, no. 9, pp. 3045–3061, Sept. 2014.

[8] R. R. Mosier and R. G. Clabaugh, "Kineplex, a bandwidth-efficient binary transmission system," *AIEE Trans.*, vol. 76, no. 6, pp. 723–728, Jan. 1958.

[9] G. Porter, "Error distribution and diversity performance of a frequency-differential PSK HF modem," *IEEE Trans. Commun. Technol.*, vol. 16, no. 4, pp. 567–575, Aug. 1968.

[10] M. Zimmerman and A. L. Kirsch, "The AN/GSC-10 (KATHRYN) variable rate data modem for HF radio," *IEEE Trans. Commun. Technol.*, vol. 15, no. 2, pp. 197–204, Apr. 1967.

[11] P. Roshan and J. Leary, *802.11 Wireless LAN Fundamentals*. Indiana, IN, USA: Cisco Press, 2004.

[12] *IEEE Standard for Local and Metropolitan Area Networks- Part16: Air Interface for Fixed Broadband Wireless Access Systems*, IEEE 802.16e, 2005.

[13] *Evolved Universal Terrestrial Radio Access (E-UTRA): Physical Channels and Modulation*, 3GPP TS 36.211 v. 8.8.0, 2009.

[14] G. Fettweis and S. Alamouti, "5G: Personal mobile internet beyond what cellular did to telephony," *IEEE Commun. Mag.*, vol. 52, no. 2, pp. 140–145, Feb. 2014.

[15] G. Fettweis, "The tactile internet: Applications and challenges," *IEEE Veh. Technol. Mag.*, vol. 9, no. 1, pp. 64–70, Mar. 2014.

[16] Y. Ding, Y. Jin, L. Ren, and K. Hao, "An intelligent self-organization scheme for the internet of things," *IEEE Comput. Intell. Mag.*, vol. 8, no. 3, pp. 41–53, Aug. 2013.

[17] H. Lin and P. Siohan, "Multi-carrier modulation analysis and WCP-COQAM proposal," *EURASIP J. Appl. Signal Process.*, vol. 2014, no. 1, pp. 1–19, May. 2014.

[18] B. Saltzberg, "Performance of an efficient parallel data transmission system," *IEEE Trans. Commun. Technol.*, vol. 15, no. 6, pp. 805–811, Dec. 1967.

[19] R. Chang, "High-speed multichannel data transmission with bandlimited orthogonal signals," *Bell Syst. Tech. J*, vol. 45, no. 6, pp. 1775–1796, Dec. 1966.

[20] L. Lin and B. Farhang-Boroujeny, "Cosine-modulated multitone for very-high-speed digital subscriber lines," *EURASIP J. Adv. Signal Process.*, vol. 2006, pp. 79–79, Jan. 2006.

[21] W. G. Jeon, K. H. Chang, and Y. S. Cho, "An equalization technique for orthogonal frequency-division multiplexing systems in time-variant multipath channels," *IEEE Trans. Commun.*, vol. 47, no. 1, pp. 27–32, Jan. 1999.

[22] R. Datta, N. Michailow, M. Lentmaier, and G. Fettweis, "GFDM interference cancellation for flexible cognitive radio phy design," in *Proc. IEEE Veh. Technol. Conf. (VTC)*, Sept. 2012, pp. 1–5.

[23] B. M. Alves, L. L. Mendes, D. A. Guimarães, and I. S. Gaspar, "Performance of GFDM over frequency selective channels," vol. 15, no. 2, Oct. 2013.

[24] G. Fettweis, M. Krondorf, and S. Bittner, "GFDM - Generalized frequency division multiplexing," in *Proc. IEEE Veh. Technol. Conf. (VTC)*, Apr. 2009, pp. 1–4.

[25] N. Michailow, M. Lentmaier, P. Rost, and G. Fettweis, "Integration of a GFDM secondary system in an OFDM primary system," in *Future Network Mobile Summit (FutureNetw), 2011*, Jun. 2011, pp. 1–8.

[26] I. Gaspar, N. Michailow, A. Navarro, E. Ohlmer, S. Krone, and G. Fettweis, "Low complexity GFDM receiver based on sparse frequency domain processing," in *Proc. IEEE Veh. Technol. Conf. (VTC)*, Jun. 2013, pp. 1–6.

[27] J. Proakis, *Digital Communications*, 5th ed. New York, NY, USA: McGraw-Hill, 2007.

[28] R. W. Chang, "Synthesis of band-limited orthogonal signals for multichannel data transmission," *Bell Syst. Tech. J.*, vol. 45, no. 10, pp. 1775–1796, Dec. 1966.

[29] A. Sahin, I. Guvenc, and H. Arslan, "A survey on multicarrier communications: Prototype filters, lattice structures, and implementation aspects," *IEEE Commun. Surveys Tuts.*, vol. 16, no. 3, pp. 1312–1338, Mar. 2014.

[30] M. Matthe, L. Mendes, and G. Fettweis, "Generalized frequency division multiplexing in a gabor transform setting," *IEEE Commun. Lett.*, vol. 18, no. 8, pp. 1379–1382, Aug. 2014.

[31] A. R. Bahai and B. R. Saltzberg, *Multi-Carrier Digital Communications: Theory and Applications of OFDM*. Norwell, MA: Kluwer, 1999.

[32] C. Cook and M. Bernfeld, *Radar signals: an introduction to theory and application*, ser. Electrical science series. New York: Academic Press, 1967.

[33] W. Y. Chen, *DSL: Simulation Techniques and Standards Development for Digital Subscriber Lines*. Indianapolis, IN: Macmillian, 1998.

[34] T. Rappaport, *Wireless Communications: Principles and Practice*, 2nd ed. Upper Saddle River, NJ, USA: Prentice Hall PTR, 2001.

[35] T. Strohmer and S. Beaver, "Optimal OFDM design for time-frequency dispersive channels," *IEEE Trans. Commun.*, vol. 51, no. 7, pp. 1111–1122, Jul. 2003.

[36] B. Boashas, *Time Frequency Signal Analysis and Processing : A Comprehensive Reference*. Oxford, UK: Elsevier, 2003.

[37] P. Siohan and C. Roche, "Cosine-modulated filterbanks based on extended gaussian functions," *IEEE Trans. Signal Process.*, vol. 48, no. 11, pp. 3052–3061, Nov. 2000.

[38] R. Haas and J.-C. Belfiore, "A time-frequency well-localized pulse for multiple carrier transmission," *Wireless Pers. Commun.*, vol. 5, no. 1, pp. 1–18, Jul. 1997.

[39] M. Alard, "Construction of a multicarrier signal," 1996, Patent WO 96/35278.

[40] B. Le Floch, M. Alard, and C. Berrou, "Coded orthogonal frequency division multiplex," *Proc. IEEE*, vol. 83, no. 6, pp. 982–996, Jun. 1995.

[41] H. Bolcskei and F. Hlawatsch, "Discrete Zak transforms, polyphase transforms, and applications," *IEEE Trans. Signal Process.*, vol. 45, no. 4, pp. 851–866, Apr. 1997.

[42] C. Heil, "A discrete Zak transform," MITRE Corp., Danvers, MA, Tech. Rep. MTR-89W000128, 1989.

[43] A. Janssen and H. Boleskei, "Equivalence of two methods for constructing tight gabor frames," *IEEE Signal Process. Lett.*, vol. 7, no. 4, pp. 79–82, Apr. 2000.

[44] T. Weiss and F. Jondral, "Spectrum pooling: an innovative strategy for the enhancement of spectrum efficiency," *IEEE Commun. Mag.*, vol. 42, no. 3, pp. S8–14, Mar. 2004.

[45] S. Haykin, "Cognitive radio: Brain-empowered wireless communications," *IEEE J. Sel. Areas Commun.*, vol. 23, no. 2, pp. 201–220, Feb. 2005.

[46] Federal Communications Commission, "Spectrum policy task force report, FCC 02-155," Nov. 2002.

[47] J. Andrews, S. Buzzi, W. Choi, S. Hanly, A. Lozano, A. Soong, and J. Zhang, "What will 5G be?" *IEEE J. Sel. Areas Commun.*, vol. 32, no. 6, pp. 1065–1082, Jun. 2014.

[48] C. Stevenson, G. Chouinard, Z. Lei, W. Hu, S. Shellhammer, and W. Caldwell, "IEEE 802.22: The first cognitive radio wireless regional area network standard," *IEEE Commun. Mag.*, vol. 47, no. 1, pp. 130–138, Jan. 2009.

[49] M. Kaur, M. Uddin, H. Verma, and B. Ambedkar, "Role of cognitive radio on 4g communications a review," *J. Emerg. Trends Comput. Inf. Sci.*, vol. 3, no. 2, 2012.

[50] *Air interface for fixed broadband wireless access systems*, IEEE 802.16-revd/d5-2004.

[51] *LTE; Evolved Universal Terrestrial Radio Access (E-UTRA): User Equipment (UE) radio transmission and reception*, ETSI, 3GPP TS 36.101, version 8.10.0, Release 8, 2010.

[52] A. Saleh, "Frequency-independent and frequency-dependent nonlinear models of TWT amplifiers," *IEEE Trans. Commun.*, vol. 29, no. 11, pp. 1715–1720, Nov. 1981.

[53] C. Rapp, "Effects of HPA-nonlineariry on 4-DPSK/OFDM-signal for a digital sound broadcasting system," in *Eur. Conf. Satell. Commun.*, Oct. 1991, pp. 179–184.

[54] M. O'Droma, S. Meza, and Y. Lei, "New modified Saleh models for memoryless nonlinear power amplifier behavioural modelling," *IEEE Commun. Lett.*, vol. 13, no. 6, pp. 399–401, Jun. 2009.

[55] M. Shaat and F. Bader, "Computationally efficient power allocation algorithm in multicarrier-based cognitive radio networks: OFDM and FBMC systems," *EURASIP J. Adv. Signal Process.*, vol. 2010, pp. 5:1–5:11, Jan. 2010.

[56] H. Zhang, D. Le Ruyet, D. Roviras, Y. Medjahdi, and H. Sun, "Spectral efficiency comparison of OFDM/FBMC for uplink cognitive radio networks," *EURASIP J. Adv. Signal Process.*, vol. 2010, pp. 4:1–4:11, Jan. 2010.

[57] H. Yamaguchi, "Active interference cancellation technique for MB-OFDM cognitive radio," in *Proc. Microw. Conf.*, Oct. 2004, pp. 1105–1108.

[58] S. Brandes, I. Cosovic, and M. Schnell, "Reduction of out-of-band radiation in OFDM systems by insertion of cancellation carriers," *IEEE Commun. Lett.*, vol. 10, no. 6, pp. 420–422, Jun. 2006.

[59] H. Mahmoud and H. Arslan, "Sidelobe suppression in OFDM-based spectrum sharing systems using adaptive symbol transition," *IEEE Commun. Lett.*, vol. 12, no. 2, pp. 133–135, Feb. 2008.

[60] P. Stoica and R. Moses, *Introduction to Spectral Analysis*. New Jersey, NJ, USA: Prentice Hall, 1997.

[61] E. Köken and A. Ö. Yılmaz, "Spectral mask compliance and amplifier nonlinearity in single carrier and OFDM systems," *Wireless Pers. Commun.*, vol. 63, no. 3, pp. 579–586, 2012.

[62] J. G. Andrews, A. Ghosh, and R. Muhamed, *Fundamentals of WiMAX: understanding broadband wireless networking*. New Jersey, NJ, USA: Pearson Education, 2007.

[63] E. Costa, M. Midrio, and S. Pupolin, "Impact of amplifier nonlinearities on OFDM transmission system performance," *IEEE Commun. Lett.*, vol. 3, no. 2, pp. 37–39, Feb. 1999.